March 2017

Particles Confined by Fluid Interfaces: Imaging Particle Motion, Interface Deformation and Capillary Forces

Paul Y. Kim
University of Massachusetts - Amherst

PARTICLES CONFINED BY FLUID INTERFACES: IMAGING PARTICLE MOTION, INTERFACE DEFORMATION AND CAPILLARY FORCES

A Dissertation Presented

by

PAUL Y. KIM

Submitted to the Graduate School of the
University of Massachusetts Amherst in partial fulfillment
of the requirements for the degree of

DOCTOR OF PHILOSOPHY

February 2017

Polymer Science and Engineering

PARTICLES CONFINED BY FLUID INTERFACES: IMAGING PARTICLE MOTION, INTERFACE DEFORMATION AND CAPILLARY FORCES

A Dissertation Presented

By

PAUL Y. KIM

Approved as to style and content by:

_____
David A. Hoagland, Co-Chair

_____
Thomas P. Russell, Co-Chair

_____
Anthony D. Dinsmore, Member

_____
David A. Hoagland, Department Head
Polymer Science and Engineering

This dissertation is dedicated to my parents.

You've been with me every step of the way.

ACKNOWLEDGMENT

This dissertation would not exist without the consistent support of colleagues, friends, and family members. Although it is impossible to adequately express my gratitude and acknowledge everyone who played a role, I will do my best to be concise while hoping the rough image I sketch gives some shape to my feelings.

I would first like to express my sincere appreciation to Professor David Hoagland. I was fortunate enough to learn from a brilliant scientist who has profound knowledge and powerful insight. His keen criticisms of my idea helped me to consider problems from different angles. I could develop my knowledge and my skills beyond my expectations thanks to his methodical approach toward science.

No less appreciation goes to Professor Thomas Russell. One of the main reasons I came to this department was my strong impression of his pioneering works. I was happy to be counted among his many students and to have had a chance to experience the way to success. I must thank him for the support he bestowed upon me. No matter how busy he was, he made time to discuss with me or listen to my problems. His broad perspective helped me to find out the important points in my experiments. He gave me the opportunity to work with other research groups and to use resources at national laboratories.

I deeply appreciate both of my advisors for always trusting me and having such great patience with me. They provided me with freedom to explore many different areas of research and helped strengthen my ability to solve problems for myself. It is easy to look back and see how much I have grown and learned over the past few years, and for this I

am truly grateful. I will remember their hearty encouragement, affection, and kindness. I would also like to thank Professor Anthony Dinsmore for sharing with me his vast experience and knowledge on complex fluids as my committee member. His input and advice were something I truly needed.

Dr. Alexander Ribbe, another one of my mentors, trained me to become an effective electron microscopist. His support was critical to my work as several core results have been available by his contribution. He has been a reliable person during my PhD life, and I am genuinely lucky to know him.

I would like to thank all the members of both the Hoagland and Russell research groups. I received positive feedback from Mengmeng, Tao, Hsinwei, Kyle, Yige, Stephen, Xiaobo, Packy, Sunzida, Kathleen, Jaewon, Jooyoung, Yao, Takeko, Sungwoo, and Joungkeun. They helped me run experiments and deeply enriched my knowledge. I am also grateful that they provided a friendly working environment for me. I would like to thank Mengmeng and Tao in particular for being such good office mates with me for more than five years. My friendship with them made my life more colorful and memorable.

Many department staff members assisted me in conducting my research and deserve my appreciation. Lou Raboin was very helpful whenever I needed to use electron microscopy and microtoming. Jacob Hirsch performed X-ray photoelectron spectroscopy and refilled a liquid nitrogen dewar. Laurie Banas helped me purchase lab supplies and chemicals as well as get travel imbursements. Lisa Groth shared with me important information for graduate students. John Nicholson assisted with the microfabrication in the cleanroom lab.

I must also thank my family who mean the most to me. Without their love and unconditional support, I couldn't be who I am today. My mother and father's encouragement and caring have been a continuing source of guidance. Thanks also to my brother, Michael, for reassuring me and for being a good travel mate while he was studying at CMU. In addition, I thank my lovely dogs, Jullie and Gommy, for giving me happiness and joy. I am grateful to my grandmother for her constant encouragement.

Finally, I thank the Heavenly Father for allowing all of the invaluable experiences I have had at Amherst. Thank you for sending me to the best place to study and for leading me to successfully complete my PhD life. Thank you with all my heart for always being with me.

ABSTRACT

PARTICLES CONFINED BY FLUID INTERFACES: IMAGING PARTICLE MOTION, INTERFACE DEFORMATION AND CAPILLARY FORCES
FEBRUARY 2017

PAUL Y. KIM

B.S., POHANG UNIVERISY OF SCIENCE AND TECHNOLOGY

M.S., UNIVERSITY OF MASSACHUSETTS AMHERST

Ph.D., UNIVERSITY OF MASSACHUSETTS AMHERST

Directed by: Professor David A. Hoagland and Professor Thomas P. Russell

Small solid particles, confined in two-dimensions by fluid interfaces, were studied by a variety of experimental methods to understand particle motion, menisci shapes near interface-supported particles, and capillary interactions among such particles. Unwanted evaporation was circumvented by adopting non-volatile ionic liquids to create the fluid interfaces. A related application, employment of ionic liquids to float cryo-microtomed polymer sections, was also developed.

The Brownian motions of nanospheres and nanorods in free-standing ionic liquid films were visualized *in situ* by high resolution scanning electron microscopy, which images features almost 100× smaller than possible in an optical microscope. For suspensions that are dilute and films that are thick compared to the particle diameter, the translational and rotational diffusion coefficients determined by single-particle tracking agreed with existing theoretical predictions. In thinner films, a striking and unexpected dynamical pairing of nanospheres was observed, suggesting a balance of capillary and hydrodynamic interactions. Nanospheres at high concentration displayed subdiffusive

caged motion and hexagonal-lattice crystallization. Concentrated nanorods in the thinner films transiently assembled into finite stacks but did not achieve high tetratic liquid crystalline order, perhaps because of spherical impurities.

A small spherical microparticles on a cylindrically curved liquid interface, to maintain constant contact angle about its wetted periphery, locally induces a quadrupolar interface deformation. Measured by optical profilometry, this deformation was compared to a recent theoretical expression, and good agreement was noted. The interface quadrupoles lead to particle capillary interactions in analogy to a 2d electrostatic quadrupoles, and as one consequence, spheres on a cylindrical interface assemble tetragonally. The assembly was monitored in the optical microscope, with particles driven to assembly as predicted, into a tetragonal lattice aligned with the underlying cylindrical axis.

Lastly, ionic liquids and their mixtures with low molecular weight solvents were applied as flotation liquids for cryo-ultramicrotomy. With control of glass transition temperature and liquid viscosity, flat and ultra-thin sections were reliably floated onto transmission electron microscopy grids at cryogenic temperature. Compared to established flotation media for soft polymer systems, the required time and skill are significantly reduced, and the operator was not exposed to noxious fumes.

TABLE OF CONTENTS

Page

LIST OF TABLES

Table Page

LIST OF FIGURES

Figure Page

CHAPTER 1

MOTIVATION AND BACKGROUND

1.1 Introduction to Particles Confined by Fluid Interfaces

Small solid particles confined by fluid interfaces are discovered in our daily life, emerging in various forms such as gels, suspensions, pastes, emulsions, and membranes. Supporting directed migration and assembly of particles, fluid interfaces create unique types of materials (i.e. bi-gels, colloidosomes, films, and Pickering emulsions) and have potential applications in magnetic data storage, oil recovery, coating, detergents, pharmaceuticals, polymer composites, metamaterials, and photovoltaic devices. As an important subject of colloid and interface sciences, particle suspensions have raised a number of questions that are new and fundamentally interesting. Preceding works on these materials discovered that internal forces in conjunction with Brownian motion determine the stability and phase behaviors. In addition to these effects, external forces such as gravity, electromagnetic field, and interfacial curvature produce complex phenomena, each of which is important in technological applications. Over the past few decades, many theoretical and experimental studies have examined the influence of these forces on particle behaviors. However, a depth of understanding is still lacking for a number of systems and requires experimental works; such systems examined in this dissertation are (i) nanoparticles suspended in an ultra-thin liquid film and (ii) spherical particles adsorbed at an anisotropically curved fluid-liquid interface.

The broad goal of this research is to provide insight into the behaviors of individual particles confined by fluid-liquid interfaces. Particles trapped in liquid film or adsorbed at

fluid-liquid interfaces were imaged directly using time-lapse electron microscopy and scanning optical profilometer to understand how particles diffuse and behave under interparticle forces, such as those from hydrodynamic and capillary interactions and steric repulsion.

1.2 Imaging Particle Motions in Liquids

Single-particle tracking is a powerful method to study dynamics in particulate systems with spatial or temporal inhomogeneity. In comparison with ensemble-averaged measurements, the approach provides much more detailed information, ranging from individual particle behaviors to their averages and distributions. A number of mathematical tools have been applied to tracking results (i.e. particle trajectories) to analyze dynamics and structural arrangements quantitatively; commonly used equations are for the mean-square displacement, pair-correlation function, orientation parameter, and inverted Boltzmann equation. The mean-square displacement $\langle r^2 \rangle$ vs. time lag t characterizes interwoven dynamical and rheological properties, allowing categorization of microscale dynamics into normal diffusion, anomalous diffusion, directed motion and confined diffusion, as summarized in Figure 1.1. The pair-correlation function $g(r)$ offers the probability of finding a particle at a certain distance from another particle, and is used for analyzing microscale structure and structural arrangements. The orientation parameter determines the local ordering in concentrated colloids, e.g. hexagonal close packing of spherical particles and alignment of rod-like particles in the nematic phase.[1, 2] The inverted Boltzmann distribution function calculates equilibrium interaction forces between particles[3, 4] or between a particle and a wall[5] from particle trajectories at a short time interval; $U(r) = -kT\ln P(r)$, where $P(r)$ is the distribution of separations

between two objects, and $U(r)$ is interaction potential.

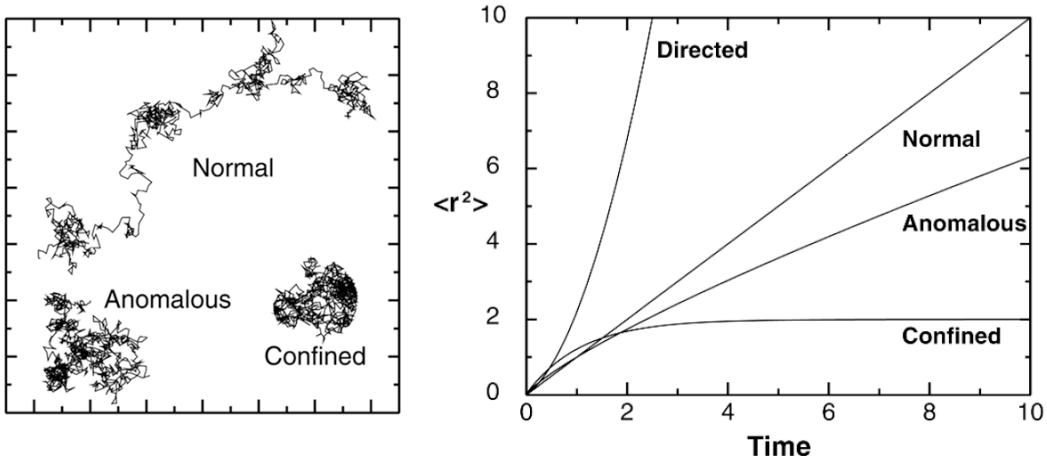

Normal	$\langle r^2 \rangle \sim t$
Anomalous	$\langle r^2 \rangle \sim t^{\gamma}$, where $\gamma < 1$
Directed	$\langle r^2 \rangle \sim 2dDt + (vt)^2$ (d is dimensionality)
Confined	$\langle r^2 \rangle \sim \langle r^2 \rangle_0 [1 - \exp(-t/\tau)]$

Figure 1.1 Trajectories, equations and the curves of mean-square displacement versus time for different types of particle motion. The figure is adapted from Saxton, *Fundamental concepts in biophysics*. New York:: Humana, 2009.[6]

Through particle tracking experiments, several groups have studied various physical phenomena in colloidal materials. Structural relaxation near the colloidal glass transition were directly imaged in three dimensions,[7] and caged diffusion,[8-11] cooperative motions,[12, 13] and ageing[7] of colloidal glasses were studied by tracking particles with confocal microscopy. Hydrodynamic and capillary interactions of colloidal particles in a soap film were characterized by manipulating the particles with optical tweezers.[14, 15] The Brownian motions of ellipsoidal particles confined to two dimensions were tracked to quantify the crossover from short-time anisotropic to longtime isotropic diffusion.[16] The micromechanics of gels was measured by imaging time-dependent particle motions in the gels.[17-19]

Particle tracking experiments often exploit tracers that exhibit fluorescence or refractive index contrast with the solvent, a practice analogous to the use of small-sized dye molecules and fluorescent proteins in biophysical single molecule tracking experiments. Because of their narrow emission spectra yet broad absorption spectra, quantum dots (i.e., semiconductor nanocrystals) enable particle experiments that require multiple labeling with a single light source. Fluorescent latex beads underlie many single-particle tracking experiments in physics and colloid science. The beads are stabilized against aggregation by introducing surface charges or by coating them with a surfactant or polymer to achieve steric stabilization.[13] Gold nanoparticles of radius ~20 nm have been employed as tracers in bright-field microscopy, where the particles appear darker due to the strong scattering of light.[20]

The spatial resolution of a microscope is described by the Rayleigh limit. The point source of light in the object plane, broadened by diffraction in the image plane, is specified by the point spread function. For bright-field microscopy, the resolution (the smallest resolvable distance between two objects) is given by

$$d = \frac{0.61\lambda}{NA},$$

where λ is a wavelength of light, NA is numerical aperture (the size of the light cone that an objective can collect). The equation reveals that the resolution of imaging can be improved by reducing λ and enhancing NA. According to the equation, the maximum resolution of optical microscope is about 200 nm (d=240 nm for λ=550 nm and NA=1.4). For isolated smaller particles, particle location can be detected beyond the resolution limit by fitting the intensities with the point spread function. However, the

particles are unresolved if they are separated by less than the Rayleigh limit. To clearly detect individual particles, the particle concentration must be kept low ensure interparticle separations are large.

Electron microscopy provides a unique window into structures and processes in solid and liquid phases, achieving a spatial resolution at the nanometer scale. Since the wavelength of electrons is less than 1 nm (λ=0.0037 nm for 100-keV electrons), the resolution is potentially much higher than that of an optical microscope. The three common types of electron microscopes capitalize on different contrast mechanisms.[21-23] Transmission electron microscope (TEM) irradiates thin samples (similar to or less than 200 nm) with a stationary, spread electron beam of 80-300 keV and forms an image by detecting transmitted electrons. In scanning TEM (STEM), a focused beam is scanned over the sample, constructing the image pixel by pixel from gathered transmitted electrons. Scanning electron microscope (SEM) scans samples with a focused beam (typical energy between 500 V and 30 keV), collecting secondary or backscattered electrons pixel by pixel. All electron microscope types require ultra-high vacuum to minimize scattering from media other than the sample. For stable imaging without evaporation, solvated or dispersed specimens can be encapsulated in vacuum-sealed cells. (Environmental scanning electron microscopy (ESEM), which achieves visualization of hydrated specimens under relaxed vacuum conditions, is limited in resolution and time due to water evaporation.[24, 25]) These cells have electron-transparent windows variously made from thin carbon foils,[26, 27] graphene sheets, [28, 29] or silicon nitride films,[30] as shown in Figure 1.2. However, cell handling is cumbersome, samples are imperfectly sealed, beam damage for organic materials is inevitable, electron scattering from cell windows

reduces image resolution and contrast, and interactions of the specimen with the cell walls can bias the visualized dynamics. Vaporization of the liquid by electron beam exposure limits the time of continuous imaging.

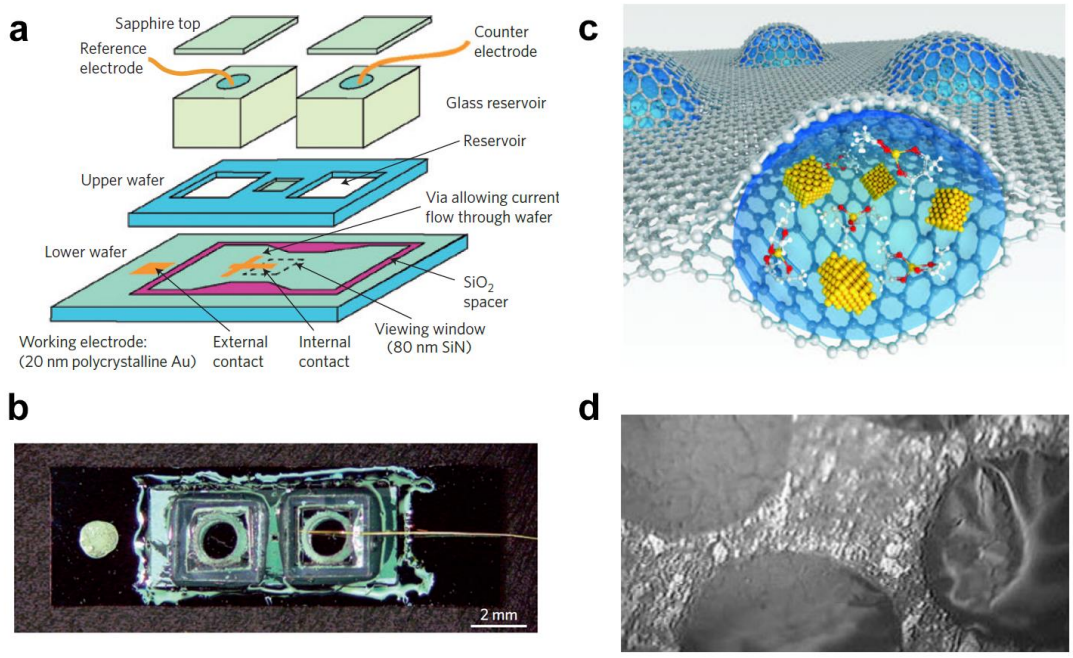

Figure 1.2 Vacuum sealing devices: liquid cells. (a) Fabrication of a liquid cell from silicon wafer with silicon nitride windows for electrochemical TEM experiment N3, (b) an assembled liquid cell N3, (c) liquid cell sealed by graphene sheets, and (d) carbon film microcapsules containing the liquid crystals. The figures are adapted from Williamson et al. *Nature Materials* **2**, 532-536 (2003),[30] Yuk et al. *Science* 2012, **336** (6077) 61-64,[29] and Daulton et al. *Microscopy and Microanalysis* **7**, 470-485 (2001).[26]

Ionic liquids (ILs) provide the basis of a new electron microscopy approach for solvated soft materials, one that obviates the need of a liquid cell. Owing to negligible volatility at room temperature, ILs are stable under high vacuum (10^{-5} to 10^{-7} Pa).[31] In addition, their characteristic properties, such as intermediate polarity, moderate viscosity, high ionic conductivity, large liquidus range, and wide electrochemical window,[32] are appropriate for electron microscopy. Using ILs as a platform for electron microscopy, the

motions of diblock copolymer assemblies in an IL thin film were imaged by TEM,[33] and the growth of gold nanoparticles from an IL solution was observed.[34] These studies demonstrated difficulties from electron beam interactions with IL, and, in particular, that at the electron doses needed for suitable TEM contrast, stable dynamics persisted for only seconds.

We demonstrate *in-situ* SEM visualizations of dynamics for spherical nanoparticles and nanorods dispersed in ultra-thin free-standing IL films at room temperature (Chapter 3). The Brownian motions of nanoparticles (NPs) are recorded in image sequences at nanoscale resolution. Through particle tracking and comparison to theoretical predictions, the applicability of the technique is verified. The SEM imaging of NPs floated on the IL surface is also presented as a relevant work.

1.3 Capillary Interaction between Adsorbed Particles at Fluid Interfaces

When a particle is adsorbed on a boundary between two immiscible fluids, the liquid interface can be deformed near the particle. Such deformations, which give rise to additional interfacial energy, generate lateral capillary forces on the particle in a way that reduces the potential energy of the system. Particle can be attracted to (or repelled from) adjacent particles over long-range distances due to overlapping of their interface deformations. The particle also can sense a gradient in interfacial curvatures and migrate toward specific locations. The phenomenon of capillary-induced migration, the so-called Cheerios effect,[35] has been an appealing approach for the manipulation of microscopic objects to fabricate materials with hierarchical structures *via* an inexpensive bottom-up process.[36-45] The precise designs of the platform provide access to directionality of migration as well as self-assembly into complex patterns.

A liquid interface is locally deformed when vertical forces are applied through an adsorbed particle on either the liquid or the interface. Mismatched density, for example, will exert a buoyancy force,[46, 47] and particles with surface charges can exert electrostatic force;[48, 49] these particular forces, respectively, can be neglected for particles that are sufficiently small or charged. Beyond such direct forces, vertical capillary forces can arise from particle wetting. For smooth particles, the equilibrium contact angle between particle and liquid interface is predicted by Young's equation to remain constant around a particle's periphery. To satisfy the constant-contact-angle condition with minimal interface deformation, a smooth spherical particle on a planar interface can simply adjust its height relative to that of the interface. For less symmetric particles, maintaining equilibrium contact angle may entail distortion of the contact line as well as deformation of the nearby interface.

The influence of particle shape on particle wetting has been demonstrated both theoretically and experimentally. An ellipsoidal (or rod-like) particles on an initially planar interface creates an interfacial curvature field (e.g., "meniscus") with an elongated quadrupolar structure, as simulated and measured by Lewandowski[50] and Botto[51]. Loudet, et al. observed assembly of polystyrene ellipsoids tip-to-tip or side-to-side at relatively small surface coverage.[52] Madivala, et al. demonstrated relatively compact percolating networks of charged polystyrene ellipsoids at fluid interfaces with local formation of triangular or flower-like structures.[53] Lewandowski et al. showed capillary interaction between SU-8 cylinders of moderate aspect ratio, with particles assembled end-to-end on a planar interface to create straight and rigid multi-particle chains.[50] These chains, when slowly compressed at an air-water interface, transformed into bamboo-like structures,[51]

and without compression, they tend to form irregular polygonal networks. Control over assembly along a preferred particle face has been also demonstrated by Lewandowski, et al. using biscotti-shaped particles with planar sides and curved ends.[54] Diblock rods that has strips of different chemical functionalization were assembled side-to-side to create two dimensional bilayers.[55] Loudet and Poulingny showed that pairs of ellipsoids with different length can assemble into arrow-shapes (i.e., with the particle axes at an angle).[56] Interaction with an initially curved interface allowed these particles to be oriented and steered along predicted trajectories, as demonstrated by Cavallaro, et al. and Lewandowski, et al.[57, 58] Even slightly non-spherical (1% deformation) particles were predicted to undulate contact line, resulting in dendritic aggregates.[59]

Similar phenomena occur when spherical particles are adsorbed at interfaces that display anisotropic curvature. In contrast to adsorption at a planar interface, spherical particles are exposed to non-uniform wetting geometry and so, to satisfy the constant-contact-angle condition, the surrounding interface must deform. In an early contribution, Wüger predicted quadrupolar deformation of catenoid surface by an adsorbed sphere.[60, 61] The spheres were expected to migrate toward the waist of the catenoid by a vertical capillary force, and there, they should order in square lattice. Russell and co-workers observed adsorbed spheres on a capillary bridge.[62] The spheres were segregated near the bridge edge by a strong driving force originating at the bridge-substrate contact line. Nobili and co-workers predicted and measured capillary forces acting on a spherical particle on an arbitrary-shaped interface.[63] The particle was subject to a capillary force when an interfaces had a gradient in Gaussian curvatures. van der Gucht and co-workers observed organization of spherical colloids into a square lattice at curved interfaces, and

they measured the capillary energy among particles (Figure 1.3).[64] The spheres ordered more strongly at higher deviatoric curvature $D=1/2|\kappa_1 - \kappa_2|$, where κ_1 and κ_2 are the principal curvatures. Zeng at el. Modeled the adsorption of spheres on cylindrical interfaces (*i.e.,* interfaces with a uniformly anisotropic curvature) by numerical calculations.[65] Because of the zero Gaussian curvature gradient, thee spheres did not experience lateral capillary forces unless the local deformations from neighboring spheres overlapped. The local deformation of cylindrical interface near an adsorbed sphere was predicted to have a quadrupolar structure. The lateral capillary force between two identical spheres has an analytical form that is analogous to the two-dimensional electrostatic interaction of quadrupole charges.

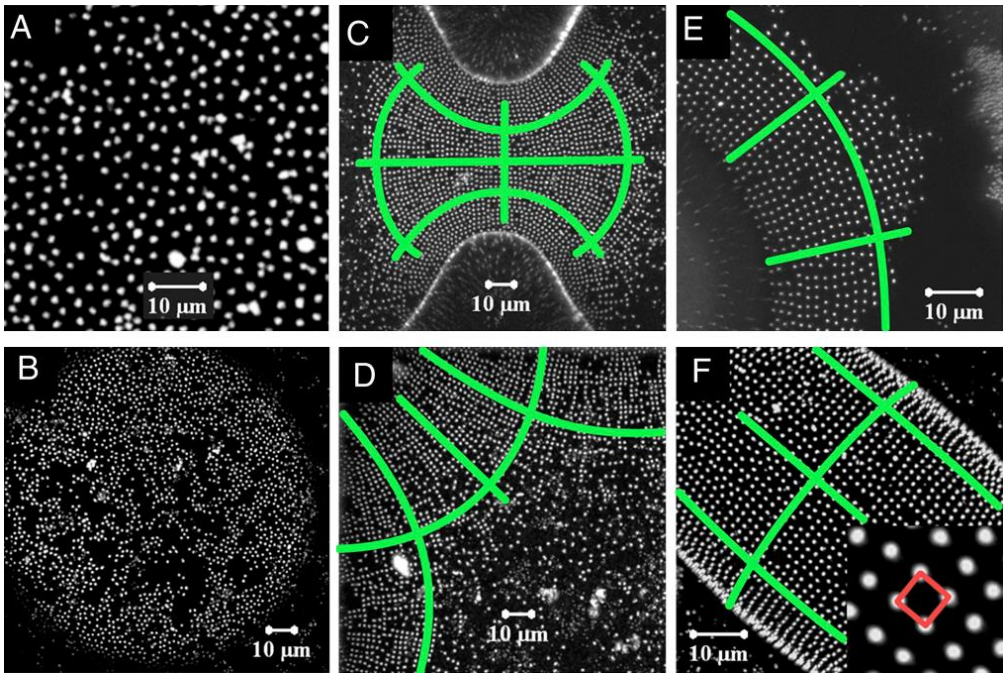

Figure 1.3 Particle organizations on oil/water interfaces of different shape. Fluorescently labeled 1.2-µm particles on (A) a flat interface, (B) a spherical interface, (C) a dumbbell-shaped interface, (D) a droplet pinned to a square patch (only one corner is shown), (E) a toroid shape interface, and (F) a prolate ellipsoid. The figure is adapted from Ershov et al. *PNAS* 2013, **110**(23)**:** 9220-9224

1.4 Structure of the thesis

Particles confined by fluid interfaces are introduced in Chapter 1 in an overview of previous theoretical and experimental studies on this topic. Chapter 2 presents the fundamentals governing the diffusion and capillary interaction of particles near (or at) fluid interfaces, and describes the derivation of the basic equations. Chapter 3 explores the dynamics of spherical nanoparticles and nanorods dispersed in ultrathin free-standing ionic liquid films (and floated on ionic liquid surface) at room temperature revealed using a new *in-situ* scanning electron microscopy visualization technique. As extended image sequences, or movies, NP and NR Brownian motions were recorded at nanoscale resolution across large film areas. Films thicknesses both smaller and larger than the particle diameters were prepared, and dispersed particle dynamics for the two differ significantly and sometimes unexpectedly. Chapter 4 describes wetting behaviors and associated capillary interactions of spherical microparticles bound to liquid interfaces, initially curved in a cylindrical shape. The meniscus structure near an isolated particle was measured using three-dimensional optical profilometer. The capillary interactions between two particles on the interface were estimated by tracking the particle motions using an optical microscope. The results from both experiments are compared to the theoretical predictions. Chapter 5 demonstrates ionic liquids as a new type of cryo-ultramicrotomy flotation media. After cryo-microtomy, polymers with low glass transition temperatures were floated on to ILs or their mixture with low molecular weight alcohols in making specimens for TEM characterization.

CHAPTER 2

THEORETICAL FUNDAMENTALS OF PARTICLE DIFFUSION AND CAPILLARY INTERACIONS

2.1 Introduction

We present a number of analytical expressions for particle diffusion and capillary interactions, supporting experimental observations in the subsequent chapters. Brownian motion and hydrodynamics of spherical or rod-like particles in fluids, i.e. bulk and thin film, are described in section 2.2. The shape of a fluid-liquid interface and the capillary interaction between adsorbed particles are explained in terms of surface tension, interfacial curvature, wetting condition, and space scaling (section 2.3).

2.2 Diffusion of Particles in Liquids

2.2.1 Brownian Motion of Particles

Small particles dispersed in a fluid undergo constant random motion due to their collisions with the molecules of surrounding fluid. The discovery of this phenomenon is attributed to the Scottish botanist Robert Brown, who observed the continuous erratic motion of pollen grains suspended in water. Extending from the early descriptions of microscopic observations, Brownian motion was described with phenomenological equations based on macroscopic laws.[66] This approach originated by Einstein is effective under several conditions, including much longer length- and time-scale of consideration compared to the surrounding molecule's characteristics, and the linear relation between flux and forces. The description of Brownian motion has two seemingly different but essentially identical expressions: Smoluchowski equation and Lanvegin equation. The

former describes the diffusion equation governing the probability of finding the particles in a particular configuration. The latter shows the mean square displacements of the individual particles as functions of time by balancing the random Brownian forces against the viscous drag. In this section, we reproduce the derivation of these equations described by Doi M. and Edwards SF.[67]

2.2.1.1 Smoluchowski Equation

Diffusion is one of the clear phenomena which appears by Brownian motion. For one-dimensional diffusion, the concentration of particle c at position x and time t can be described by the Fick's law, where the flux $J(\mathrm{x},\mathrm{t})$ is proportional to the spatial gradient of the concentration:

$$J(\mathrm{x},\mathrm{t}) = -D\frac{\partial c}{\partial \mathrm{x}},$$

where the constant D is named the diffusion coefficient. If there is external potential $U(x)$, its gradient creates force F, resulting in non-vanishing velocity v:

$$\mathrm{v} = \frac{F}{\zeta} = -\frac{1}{\zeta}\frac{\partial U}{\partial x}.$$

The constant ζ is called the friction coefficient and its inverse $1/\zeta$ is called the mobility. ζ can be obtained from hydrodynamic if the particle is sufficiently large, as described in the following sections. The total flux is increased by flux cv due to the potential gradient:

$$J = -D\frac{\partial c}{\partial \mathrm{x}} - \frac{c}{\zeta}\frac{\partial U}{\partial x}.$$

In equilibrium state, the flux disappears and the concentration obeys the Boltzmann

distribution $c_{eq} \propto \exp(-U(x)/k_B T)$:

$$-D\frac{\partial c_{eq}}{\partial \mathrm{x}} - \frac{c_{eq}}{\zeta}\frac{\partial U}{\partial x} = 0.$$

Solving this equation leads to the Einstein relation:

$$D = \frac{k_B T}{\zeta}.$$

Einstein relation states that the diffusion of an object is related to the response to the thermal fluctuations. Substituting D in Fick's second law gives a diffusion equation named Smoluchowski equation:

$$\frac{\partial c}{\partial \mathrm{t}} = \frac{\partial}{\partial \mathrm{x}}\frac{1}{\zeta}\left(k_B T\frac{\partial c}{\partial x} + c\frac{\partial U}{\partial x}\right) = 0.$$

2.2.1.2 Langevin Equation

The sum of incessant collisions of the fluid molecules provides the random force $f(t)$ on the Brownian particle. The Langevin equation describes the balance between the random force, the viscous drag, and the particle inertia:

$$\zeta\frac{\mathrm{dx}}{\mathrm{dt}} = -\frac{\partial U}{\partial x} + f(\mathrm{t}).$$

For the Brownian motion of a free particle (U=0), the equation is reduced to

$$\zeta\frac{\mathrm{dx}}{\mathrm{dt}} = f(\mathrm{t}).$$

If the initial particle location is $\mathrm{x_o}$ at $\mathrm{t} = 0$, the displacement of the particle at $\mathrm{t} = \tau$ is

$$\mathrm{x}(\tau) - \mathrm{x_o} = \frac{1}{\zeta}\int_0^{\tau} f(\mathrm{t})\,\mathrm{dt}.$$

As $f(\mathrm{t})$ is considered as a Gaussian random variable, the probability distribution of

$\mathrm{x(t)}$ reveals the Gaussian distribution:

$$\Psi(\mathrm{x},\tau) = \frac{1}{\sqrt{2\pi \mathrm{B}}} \exp\left(-\frac{(\mathrm{x}-\mathrm{A})^2}{2\mathrm{B}}\right),$$

where

$$\mathrm{A} = \langle \mathrm{x}(\tau) \rangle = \mathrm{x_o},$$

$$\mathrm{B} = \langle (\mathrm{x}(\tau) - \mathrm{A})^2 \rangle = \frac{2k_B T}{\zeta}\tau = 2D\tau,$$

where calculations of A and B are based on the characteristics of $f(\mathrm{t})$ moment:

$$\langle f(\mathrm{t}) \rangle = 0;\ \langle f(\mathrm{t}) \rangle \langle f(\mathrm{t}') \rangle = 2\zeta k_B T \delta(\mathrm{t}-\mathrm{t}').$$

Therefore, the distribution of Brownian particles at an equilibrium state is written as

$$\Psi(\mathrm{x},\tau) = \frac{1}{\sqrt{4\pi D\tau}} \exp\left(-\frac{(\mathrm{x}-\mathrm{x}')^2}{4D\tau}\right).$$

2.2.2 Hydrodynamics of Particles in Bulk Liquids

2.2.2.1 Hard Spheres

We consider the uniform motion of a rigid sphere in an infinite expanse of fluid, following the derivation described by Kleinstreuer C.[68] If the inertial force on the sphere is negligible in comparison with the viscous force, the Navier-Stokes equations are reduced into the Stokes equations: $\nabla p = \eta \nabla^2 \vec{v}$ and $\nabla \cdot \vec{v} = 0$, where p is pressure, η is viscosity, and $\vec{v}$ is flow velocity. Such situation occurs with slow flow around a submerged body, highly viscous lubrication, small length-scale flow, or very low density flow. The flow field ψ past a sphere can be expressed in the spherical coordinates using the Stokes equations:

$$\left[\frac{\partial^2}{\partial r^2}+\frac{\sin\theta}{r^2}\frac{\partial}{\partial\theta}\left(\frac{1}{\sin\theta}\frac{\partial}{\partial\theta}\right)\right]^2\psi=0$$

with the boundary conditions of

$$v_r=\frac{1}{r^2\sin\theta}\frac{\partial\psi}{\partial\theta}=0\text{ at }r=a$$

$$v_\theta=-\frac{1}{r\sin\theta}\frac{\partial\psi}{\partial r}=0\text{ at }r=a$$

$$\psi=\frac{1}{2}Ur^2\sin^2\theta\text{ at }r\to\infty,$$

where r is a radial distance from the sphere center, a is the sphere radius, U is the flow speed of the sphere relative to the fluid at an infinite distance. Applying the boundary conditions to the equation yields

$$\psi=\frac{r^2}{2}\left(1-\frac{3a}{2r}+\frac{a^3}{2r^3}\right)\sin^2\theta$$

with the velocity components

$$v_r=U\left[1-\frac{3a}{2r}+\frac{a^3}{2r^3}\right]\cos\theta,$$

$$v_\theta=-U\left[1-\frac{3a}{4r}-\frac{a^3}{4r^3}\right]\sin\theta.$$

The pressure field P and shear stress $\tau_{r\theta}$ around the sphere can be calculated from the velocity components.

$$P=P_\infty-\frac{3\eta aU}{2r^2}\cos\theta,$$

$$\tau_{r\theta}=\eta\left(\frac{1}{r}\frac{\partial v_r}{\partial\theta}+\frac{\partial v_\theta}{\partial r}\right)=-\frac{\eta U}{r}\left(1-\frac{3a}{4r}+\frac{5a^3}{4r^3}\right)\sin\theta.$$

The distribution of P and $\tau_{r\theta}$ on the sphere surface ($r = a$) is visualized in Figure 2.1.

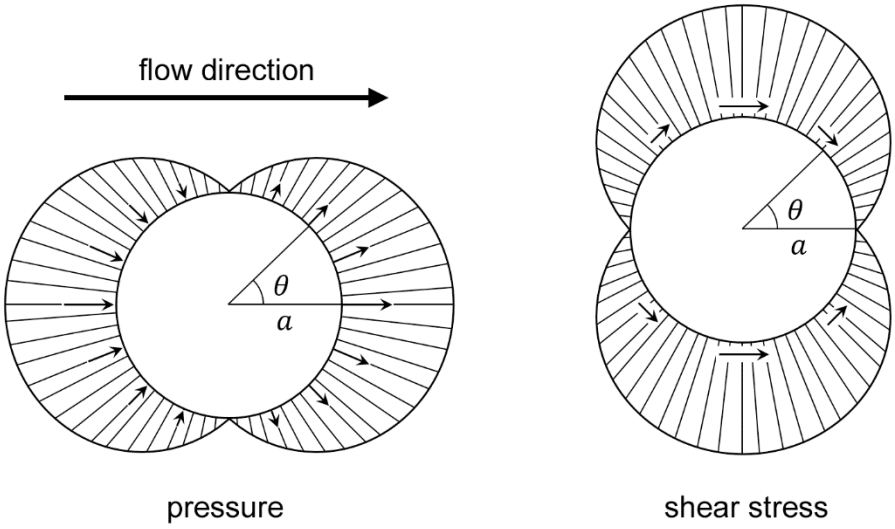

$$P = -\frac{3\eta U}{2a}\cos\theta \qquad \tau_{r\theta} = \frac{3\eta U}{2a}\sin\theta$$

Figure 2.1 Pressure and shear stress field on the surface of sphere in a flow of viscous fluid. The distribution is shown in a planar section parallel to the flow direction.

The drag force acting on the sphere is obtained by the integration of P and $\tau_{r\theta}$

$$F_d = \int_0^{\pi} (P|_{r=a}\sin\theta + \tau_{r\theta}|_{r=a}\cos\theta) 2\pi a^2 \sin\theta \, d\theta$$

$$= 2\pi\eta U a + 4\pi\eta U a = 6\pi\eta U a,$$

which is the Stokes law. The corresponding friction coefficient shows up to be

$$\zeta_{sphere} = \frac{F_d}{U} = 6\pi\eta a.$$

Combining the Stokes law with the Einstein equation gives the Stokes-Einstein equation:

$$D = \frac{k_B T}{6\pi\eta a}.$$

Rigid Rods:

Rod-like particles in fluids display translational and rotational Brownian motions. The friction coefficients of both motions can be estimated by 'shish-kebab' model as illustrated in Figure 2.2 (derivation were taken from Doi M., Edwards SF[67]); a rigid rod is regarded as a straight string of beads numbered from $-N/2$ to $N/2$ in the total length of $L = Nb$.[67] If the particle rotates in an angular velocity $\boldsymbol{\omega}$, the bead *n* separated from the center by a nb distance will move at $\boldsymbol{v}_n = \boldsymbol{\omega} \times nb\boldsymbol{u}$ velocity, where $\boldsymbol{u}$ is the unit vector parallel to the particle axis. The friction force on the bead *n* is $-\zeta_b \boldsymbol{v}_n$ (or $-3\pi\eta b\boldsymbol{v}_n$) if the hydrodynamic interaction is ignored. Then, the total torque on the particle due to the hydrodynamic friction is given by

$$\boldsymbol{\tau}_{friction} = \sum_{n=-N/2}^{N/2} nb\boldsymbol{u} \times -\zeta_b \boldsymbol{v}_n = -\zeta_b \frac{(Nb)^3}{4} \boldsymbol{\omega}.$$

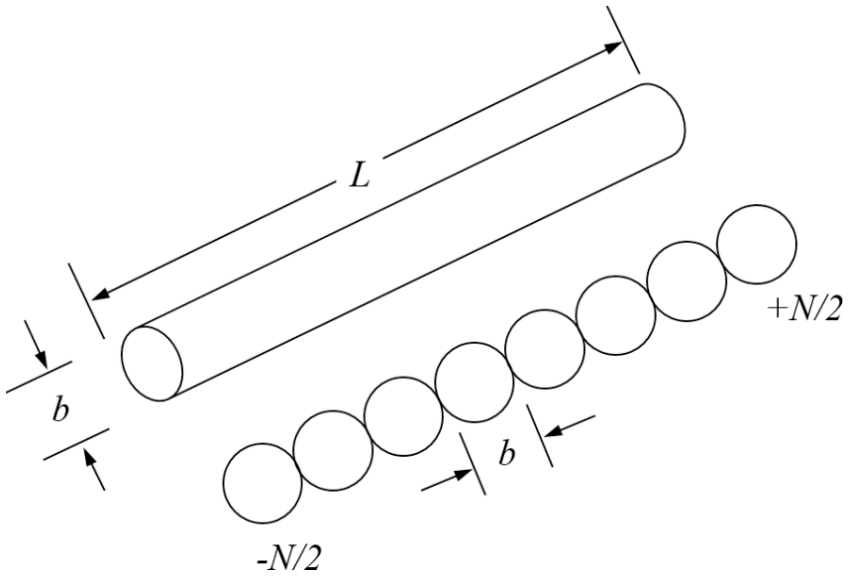

Figure 2.2 Rigid rod-like particle and shish-kebab model, which consists of N beads of diameter b placed along a straight line of length L.

The external torque $\boldsymbol{\tau}$ balances the hydrodynamic friction, therefore the rotational diffusion coefficient is calculated as

$$\zeta_{rotation} = \frac{\boldsymbol{\tau}}{\boldsymbol{\omega}} = \zeta_b \frac{(Nb)^3}{4} = \frac{\pi\eta L^3}{4}.$$

If the hydrodynamic interaction between beads is taken in to account, $\zeta_{rotation}$ becomes

$$\zeta_{rotation} = \frac{\pi\eta L^3}{3(\ln(L/b) + \delta)},$$

where δ is the end-effect correction that depends on the rod's aspect ratio, $p = L/b$. The estimation is based on the Kirkwood-Riseman theory, which describes hydrodynamic interaction between beads using Oseen approximation. The theory also predicts the translation friction coefficients parallel ($\zeta_{||}$) and perpendicular ($\zeta_{\perp}$) to the rod axis and the overall friction coefficient ($\zeta_{translation}$).

$$\zeta_{||} = \frac{2\pi\eta L}{\ln(\mathrm{L/b}) + \upsilon_{||}}, \quad \zeta_{\perp} = \frac{4\pi\eta L}{\ln(L/b) + \upsilon_{\perp}},$$

$$\zeta_{translation} = \frac{3}{(2/\zeta_{||}) + (1/\zeta_{\perp})} = \frac{3\pi\eta L}{\ln(L/b) + \upsilon}$$

where $\upsilon_{||}$, $\upsilon_{\perp}$, and υ are the end-effect corrections. Numerical values of δ, $\upsilon_{\perp}$, $\upsilon_{||}$, and υ have been calculated for particles with symmetric ends and fitted to simple quadratic equations for interpolation in the range of $2 < p < 30$:[69-71]

$$\delta_{\perp} = -0.662 + 0.917/p - 0.050/p^2$$

$$\upsilon_{\perp} = 0.839 + 0.185/p + 0.233/p^2$$

$$\upsilon_{||} = -0.207 + 0.980/p - 0.133/p^2$$

$$\upsilon = 0.312 + 0.565/p - 0.100/p^2.$$

Since $\zeta_{||} < \zeta_{\perp}$, the rod moves more easily in the direction parallel to the rod axis than that perpendicular. If rotation is prohibited, the rod will diffuse independently in two directions with diffusion coefficients $D_i = k_B T/\zeta_i$, where i is $||$ or $\perp$. However, if rotation is allowed, the rotational diffusion (with $D_r = k_B T/\zeta_{rotation}$) washes out directional memory and leads to a crossover from anisotropic to isotropic diffusion at time longer than the diffusion time $\tau_r = 1/2D_r$.[16]

The thermal kicks on the rod are random, therefore the probability distribution function (PDF) of the body-frame displacement (Figure 2.3) is Gaussian at all times:

$$\Psi(\tilde{x}_i, \tau) = \frac{1}{\sqrt{4\pi D_i \tau}} \exp\left(-\frac{\tilde{x}_i^2}{4D_i\tau}\right).$$

Meanwhile, the displacement statistics in the lab frame are non-Gaussian due to the dissipative coupling of translational motion to rotational motion. At short time, the body- and lab-frame displacements are equal, therefore the PDFs of both displacements are Gaussian. The central limit theorem implies that the PDF of the lab-frame displacement also becomes Gaussian at time longer than τ_r; the theorem is applicable because the lab-frame displacement is a sum of displacements for ~τ/τ_r statistically independent steps. Thus at fixed initial particle orientations, non-Gaussian behavior is expected to vanish at $\tau = 0$ and $\tau = \infty$ and to maximize near the order of τ_r. If the PDF is averaged for all particle orientations, the distribution becomes non-Gaussian particularly as $\tau \to 0$ (no rotational displacement).

$$\Psi(\mathrm{x}_j, \tau) = \lim_{\tau \to 0} \int_0^{2\pi} \frac{1}{\sqrt{2\pi}\sigma} \exp\left(-\frac{{\mathrm{x}_j}^2}{2\sigma^2}\right) \frac{d\theta}{2\pi},$$

where $\sigma^2 = {\sigma_{||}}^2 \cos^2\theta + {\sigma_{\perp}}^2 \sin^2\theta$ with $\sigma_{||} = 2D_{||}\tau$ and $\sigma_{\perp} = 2D_{\perp}\tau$.

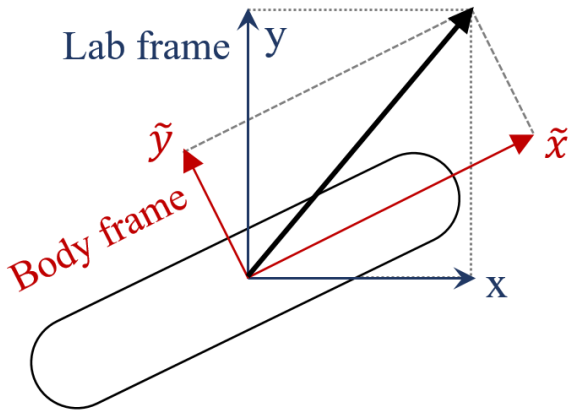

Figure 2.3 Representation of a rod in the $\tilde{x}$-$\tilde{y}$ body frame and the x-y lab frame.

2.2.3 Hydrodynamics of Particles in Liquid Films

The particle motions in a liquid film are more complex than that in a bulk fluid. If the film thickness is comparable to the particle diameter, particles are confined in two-dimensions (2D), and their motions are controlled by an effective 2D film viscosity estimated from the contributions of the bulk fluid and fluid-fluid interfaces as shown in Figure 2.4:[72]

$$\eta_{\text{film}} = \eta_{\text{bulk}} h + 2\eta_{\text{int}},$$

where η_{bulk} is the viscosity of the bulk fluid, η_{int} is the interface viscosity, and h is the film thickness. The units of η_{film} is Pa·s·m in contrast with that of bulk viscosity Pa·s. In addition to the film viscosity, surrounding fluids influences the flow in the liquid film. The diffusion coefficient of a disk of diameter d and height h in the liquid film can be approximated by considering a 2D membrane with both sides surrounded by the 3D fluid, as described by Saffman PG., Delbrück M. [73]:

$$D = \frac{k_B T}{4\pi\eta_{\text{film}}}\left[\ln\left(\frac{2}{\eta_{\text{surrounding}}/\eta_{\text{film}}}\right) - \gamma_E\right],$$

where γ_E is Euler's constant (=0.577). The equation is effective for small ε.

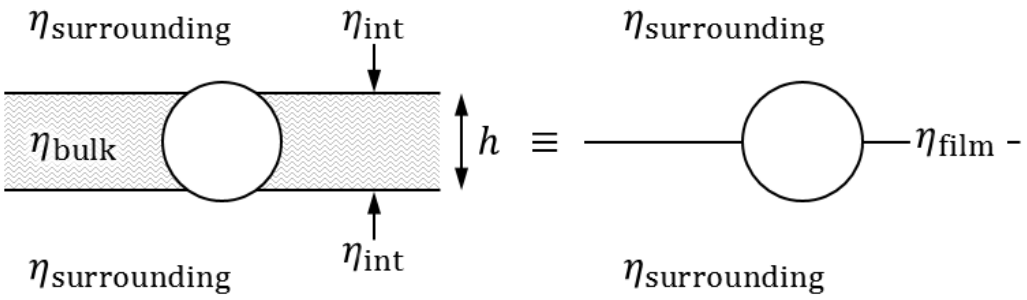

Figure 2.4 Approximation of the liquid film into a single interface.

2.3 Capillary Interaction between Particles at a Liquid-Fluid Interface

2.3.1 Definition of Surface Tension

We consider a system of two homogeneous bulk phases (α and β) divided by an infinitely thin interface.[74] If temperature and volume of each phase keep constant, the work done by the interface dW is proportional to the change in interfacial area dA:

$$dW = \gamma dA.$$

The positive coefficient γ is called surface tension. Including the work done by the interface, the variation of the Gibbs energy G of the system is given by

$$dG = -SdT + V_\alpha dP_\alpha + V_\beta dP_\beta + \sum \mu_i \, dN_i + \gamma dA,$$

where S is the entropy, T is the temperature, V is the volume, P is the pressure, μ_i is the chemical potential of element i, and N is the number of element i. Both bulk

phases have the same pressure P_α=P_β=P when the interface has a planar geometry:

$$dG = -SdT + VdP + \sum \mu_i \, dN_i + \gamma dA.$$

From the equation, the surface tension can be defined as a derivative of the Gibbs energy:

$$\left.\frac{\partial G}{\partial A}\right|_{T,P,N_i} \equiv \gamma.$$

The physical origin of the surface tension is related to molecular interactions; for immiscible fluids, molecules are more stable in the bulk phase than at the interface. The net potential energy of the system increases as the number of molecules from the bulk phases to the interface increases linearly with an expanding interfacial area.

2.3.2 Shape of Fluid-Liquid Interfaces

For smooth surfaces, the geometry at any point can be defined by two principal curvatures along the sections normal to the surface. According Euler's theorem, the sections of two principal curvatures are orthogonal to each other, and the sum of the curvatures is equal to that of curvatures along two arbitrary normal sections:

$$\kappa = \kappa_1 \cos^2\theta + \kappa_2 \sin^2\theta$$

$$\kappa_\perp = \kappa_1 \cos^2(\theta + \pi/2) + \kappa_2 \sin^2(\theta + \pi/2) = \kappa_1 \sin^2\theta + \kappa_2 \cos^2\theta$$

$$\kappa + \kappa_\perp = (\kappa_1 + \kappa_2)(\cos^2\theta + \sin^2\theta) = \kappa_1 + \kappa_2,$$

where κ_1 and κ_2 are principal curvatures, κ and $\kappa_\perp$ are curvatures in any normal sections, and θ is an angle between principal curvature direction and arbitrary curvature direction. The local surface curvature can be described effectively by Gaussian curvature $K = \kappa_1\kappa_2$ and mean curvature $H = 1/2(\kappa_1 + \kappa_2)$.

The shape of fluid-liquid interfaces is governed by the Young-Laplace equation, which relates the pressure difference across the interface to the geometry and the surface tension:

$$\Delta p = 2\gamma H = \gamma\left(\frac{1}{R_1} + \frac{1}{R_2}\right),$$

where Δp is the pressure difference, γ is interfacial tension, R_1 and R_2 are the principal radii of the curvature. The equation can be derived either by force balance or by energy minimization. Both cases assume an ideal interface (*i.e.* zero thickness) for constant surface tension. In equilibrium and in the absence of gravity or other external fields, the pressure across the interface should be uniform, and therefore the interface displays the shape of a constant mean curvature.

2.3.2.1 Derivation of Young-Laplace Equation

We follow the derivation of Young-Laplace equation using force balance described by Defay, R and Prigogine, I.[75] Figure 2.5 shows a small patch of a fluid interface, of which boundary is at a constant distance ρ from the center point *P*. The curves *AB* and *CD* (through *P*) are sections along the principal curvatures with radii of curvatures R_1 and R_2, respectively. At point A, the segment δl is subjected to a surface tension $\gamma \times \delta l$. The projection of the surface tension onto the normal vector *PN* is

$$F_A = (\gamma \times \delta l)\sin\phi \simeq \gamma\phi \times \delta l = \gamma\frac{\rho}{R_2} \times \delta l.$$

The sum of projected forces applied on *A*, *B*, *C*, and *D* is calculated as

$$F_A + F_B + F_C + F_D = 2\gamma\rho\left(\frac{1}{R_1} + \frac{1}{R_2}\right) \times \delta l$$

As mentioned above, the value in the parenthesis is independent of the choice of *AB* and *CD* if two are orthogonal to each other. Therefore, the total projected force around the periphery can be obtained by integration over one quarter of a revolution:

$$2\gamma\rho\left(\frac{1}{R_1}+\frac{1}{R_2}\right)\times\int_0^{\frac{\pi\rho}{2}}\delta l=\pi\rho^2\gamma\left(\frac{1}{R_1}+\frac{1}{R_2}\right).$$

The force in normal direction (*PN*) is originated by the pressure difference across the interface, $\Delta p\times\pi\rho^2$. The Young-Laplace equation can be derived by equating the surface tension along the periphery and the pressure on the surface.

$$\Delta p\times\pi\rho^2=\pi\rho^2\gamma\left(\frac{1}{R_1}+\frac{1}{R_2}\right)$$

$$\Delta p=\gamma\left(\frac{1}{R_1}+\frac{1}{R_2}\right)$$

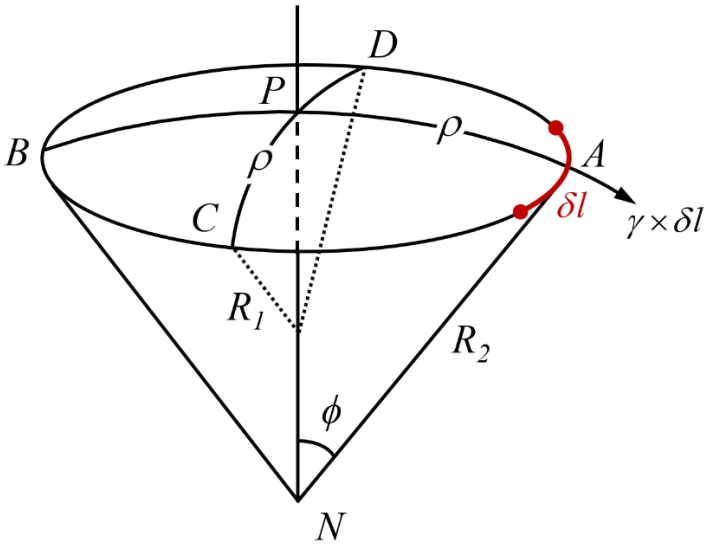

Figure 2.5 Local non-spherical surface at an equilibrium state

2.3.3 Wetting of Particles at Fluid Interfaces

Particles adsorb on an interface between immiscible fluids when the total interfacial energy is lowered by the contact between particles and fluid phases. If the particles have smooth surface (*i.e.* no pinning of the line of contact), the angle of contact between particles and the fluid interface satisfies an equilibrium constant, as predicted by Young-Dupré equation. Here, we consider wetting of a spherical particle at a planar fluid interface and derive the equation based on an argument by Pieranski P.[76]

Contact angle of a spherical bead at a planar fluid interface:

When a spherical solid particle is bound to a planar gas-liquid interface (Figure 2.6), the total surface energy is determined by the contributions from liquid-solid (LS), solid-vapor (SV), and liquid-vapor (LV) interfaces. The energies of each interface can be calculated from simple geometric arguments:

$$E_{LS} = 2\pi a^2(1 - z/a)\gamma_{LS}$$

$$E_{SV} = 2\pi a^2(1 + z/a)\gamma_{SV}$$

$$E_{LV} = \pi R^2(1 - z^2/a^2)\gamma_{LV},$$

where z is the vertical position of the particle center with respect to the level of the vapor-liquid interface, and a is the radius of the particle. The particle adjusts its vertical position to minimize the total surface energy:

$$\frac{\partial E}{\partial z} = \frac{\partial}{\partial z}(E_{LS} + E_{SV} - E_{LV}) = 0$$

$$\frac{\bar{z}}{a} = \frac{\gamma_{LS} - \gamma_{SV}}{\gamma_{LV}}$$

where $\bar{z}$ is z at equilibrium. Since $\bar{z}/a = -\cos\theta$ by trigonometry, the above equation

can be re-written in Young-Dupré equation.

$$\gamma_{LS} + \gamma_{LV} \cos\theta = \gamma_{SV}$$

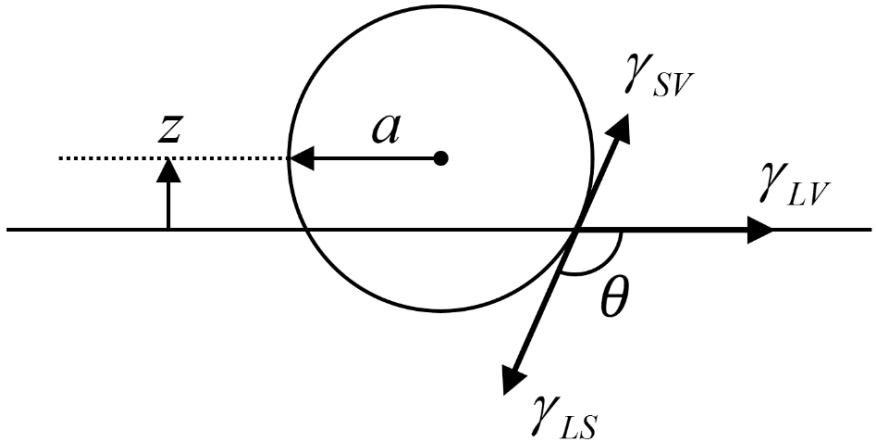

Figure 2.6 Spherical solid particle adsorbed at a planar vapor-liquid interface. The particle has radius a and positioned at z from the interface.

2.3.4 Perturbation of Fluid Interfaces by Particle Adsorption

Owing to Laplace's law, an interface with an adsorbed particle satisfies constant mean curvature at an equilibrium state. The interface x characterized by a mean curvature H_0 is perturbed into a shape with a mean curvature H_1 by normal deflection $\zeta(x)$. The variation of the mean curvature $\delta H \equiv (H_1 - H_0)/H_0$ is given to first order in $\zeta(x)$ by

$$\delta H(x) = -\left[\left((2H_0)^2 - G_0(x)\right) + \nabla_s B(x) \cdot \nabla_s + \frac{1}{2}\nabla_s^2\right]\zeta(x),$$

$$B(x) \equiv -\frac{1}{8}\ln[(H_0)^2 - G_0(x)],$$

where ∇_s and ∇_s^2 are the surface gradient and Laplacian, respectively, and $G_0(x)$ is the Gaussian curvature at x.[77] The equation implies that the deflection is uniform if the axial

symmetry of the interface is preserved by the adsorbed particle. Two examples of such case are (i) spherical particle adsorbed on a planar interface and (ii) spherical particle adsorbed on a spherical drop.

The deformation of a generic interface by an adsorbed particle has an expression

$$\zeta(x) = a^2 H_o f(xH_0; aH_0),$$

where a is a particle radius, f is a dimensionless function of $\tilde{x} = xH_o$, of which functional form shows a strong dependence on aH_o (*i.e.* multiplication of a local scale a and a global scale H_o). The amplitude of deformation $\sim a^2 H_o$ can be proved by considering two distinct scale transformations: (i) rescaling particle and interface together and (ii) rescaling particle or interface selectively. If the particle and the interface are rescaled together *via* affine transformation (*i.e.* $a'/a = H_o/H_o'$), the amplitude of deformation is proportional to the particle radius: $\zeta(x) = a\tilde{\zeta}(xH_0; aH_0)$, where $\tilde{\zeta}$ is a dimensionless function that describes the shape of the deformation. If the interface or the particle is selectively rescaled *via* non-affine transformation (*i.e.* $a'/a \neq H_o/H_o'$), the deformation disappears as the particle become vanishingly small or the interface approaches a planar shape (*i.e.* if $a' \to 0$ or $H_o' \to 0$, then $\tilde{\zeta} \to 0$). This suggest $\tilde{\zeta} \sim aH_0$, and accordingly the amplitude of ζ is proportional to $a^2 H_o$.

2.3.4.1 Spherical Particle Adsorbed on an Infinite Planar Fluid Interface

The planar shape of the interface is preserved by the adsorbed particle, therefore $H_0 = H_1 = \delta H = 0$, $G_0 = 0$, and $\nabla_s B(x) = 0$. The deformation vanishes ($\zeta = 0$) at $H_0 = 0$, since the particle can attain equilibrium contact angle by adjusting its height relative to the interface.

2.3.4.2 Spherical Particle Adsorbed on a Spherical Fluid Interface

If a spherical interface has a radius of curvature $R \gg a$, $H_0 = 1/R$ and $G_0 = 1/R^2$. For incompressible fluids, the adsorption of the particle will cause uniform interface deformation; the interface will have a radius of curvature $R[1 + O(a^3/R^3)]$, hence $\delta H \sim -O(a^3/R^4)$ and $\zeta(x) \sim O(a^3/R^2)$. Due to the co-axial symmetry of the interface and the particle, the particle doesn't undulate the interface.

2.3.4.3 Spherical Particle Adsorbed on a Cylindrical Fluid Interface

The wetting geometry along particle's periphery is azimuthally asymmetric for a particle adsorbed at a cylindrically curved interface. To satisfy constant contact angle condition, the line of contact should be undulated. Here we derive the undulation of interface by reproducing the work done by Zeng C., et al.[65] The deformed surface at equilibrium can be written in cylindrical coordinates (Figure 2.7):

$$\Phi(r, \theta, z) = r - R - a^2 H_o f(\theta, z),$$

where r is a radial distance from cylindrical axis, θ is angular distance, z is a distance along the axial direction, $R = 1/2H_o$ is a radius of initial cylindrical interface. A unit vector $\hat{n}$ normal to the interface is calculated from the surface gradient using dimension parameters $= a/R$ $\tilde{z} = z/R$, and $\tilde{r} = r/R$:

$$\hat{n} = \frac{\nabla\Phi}{|\nabla\Phi|} = (1, -\delta^2 \partial_\theta f, -\delta^2 \partial_{\tilde{z}} f).$$

Using the relation between $\hat{n}$ and the mean curvature H_1,

$$2H_1 = \nabla\hat{n} = \frac{1}{R}\left[1 - \delta^2\left(1 + \partial_\theta^2 + \partial_{\tilde{z}}^2\right) f\right],$$

$$2\delta H = \frac{H_1 - H_0}{H_0} = -\delta^2\left(1 + \partial_\theta^2 + \partial_{\tilde{z}}^2\right)f.$$

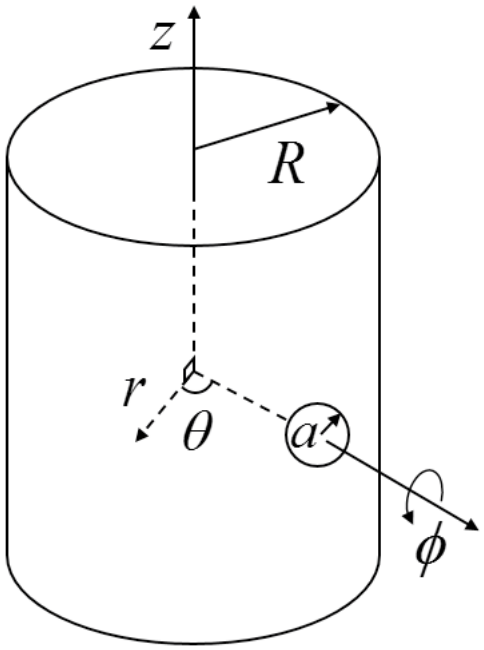

Figure 2.7 Sphere adsorbed at a section of infinitely long cylindrical fluid interface.

For an infinitely long interface, the mean curvature is unaffected by the particle adsorption (*i.e.* $\delta H = 0$), therefore the expression for f reduces to the Helmholtz equation:

$$\left(1 + \partial_\theta^2 + \partial_{\tilde{z}}^2\right)f = 0,$$

The boundary conditions for this equation are provided by the constant contact angle condition (*i.e.* $\hat{n}_i \cdot \hat{n}_p = \cos\theta$, where $\hat{n}_i$ and $\hat{n}_p$ are units normal to the particle and the interface respectively) and interface mirror symmetries:

$$f - \theta\partial_\theta f - \tilde{z}\partial_{\tilde{z}} f = -\frac{\theta^2}{2\delta^2} \text{ on } \tilde{z}^2 + \theta^2 = \delta^2 \sin^2\theta_c\,,$$

$$\partial_\theta f = 0 \text{ on } \theta = 0, \qquad \partial_\theta f = 0 \text{ on } \theta = \pi, \qquad \partial_{\tilde{z}} f = 0 \text{ on } \tilde{z} = 0$$

The Helmholtz equation and the boundary conditions are similar to electrostatic quadrupolar potential in two-dimensions. Therefore, the image method for solving Laplace equation (often used in electrostatics) can be applied to get the solution to the Helmholtz equation; a series of quadrupoles are overlaid along θ to satisfy the boundary conditions simultaneously. The solution to the interface deformation using the method is

$$f = -\frac{\pi}{48}\delta^2 \sin^4\theta_c \sum_{n=-\infty}^{\infty} [J_2(\tilde{\rho}_n) + Y_2(\tilde{\rho}_n)] \cos 2\phi_n,$$

where $\tilde{\rho}_n = \sqrt{\tilde{z}^2 + (\theta + 2n\pi)^2}$, $\phi_n = \arctan[(\theta + 2n\pi)/\tilde{z}]$, and J_2, Y_2 are the Bessel functions (of order 2) of the first and second kind, respectively. At the vicinity of the particle, the deformation has essentially identical expression to a quadrupolar electrostatic potential, as extracted from a Taylor expansion of the leading contribution, J_2:

$$f_{near} = \frac{\delta^2 \sin^4\theta_c}{12} \frac{\cos 2\phi}{\tilde{\rho}^2} + O(\delta^2).$$

2.3.5 Lateral Capillary Forces between Adsorbed Particles

The overlap of interfacial deformations by adsorbed particles can cause lateral capillary forces in directions that reduce the potential energy of the system. Particles can be attracted to or repelled from each other, depending on the signs of meniscus slopes ψ_1 and ψ_2 at the contact lines of each particle as shown in Figure 2.8. The force is attractive when $\psi_1\psi_2 > 0$ and repulsive when $\psi_1\psi_2 < 0$.[78]

If the meniscus slope varies along the particle periphery (*i.e.* capillary multipoles), the directions of capillary forces are determined by the mutual orientations. Through preferred attraction along specific orientations, particle are self-assembled in complex

aggregations, such as hexagonal lattices, square lattices, strings, and structures with voids as shown in Figure 2.8.[79]

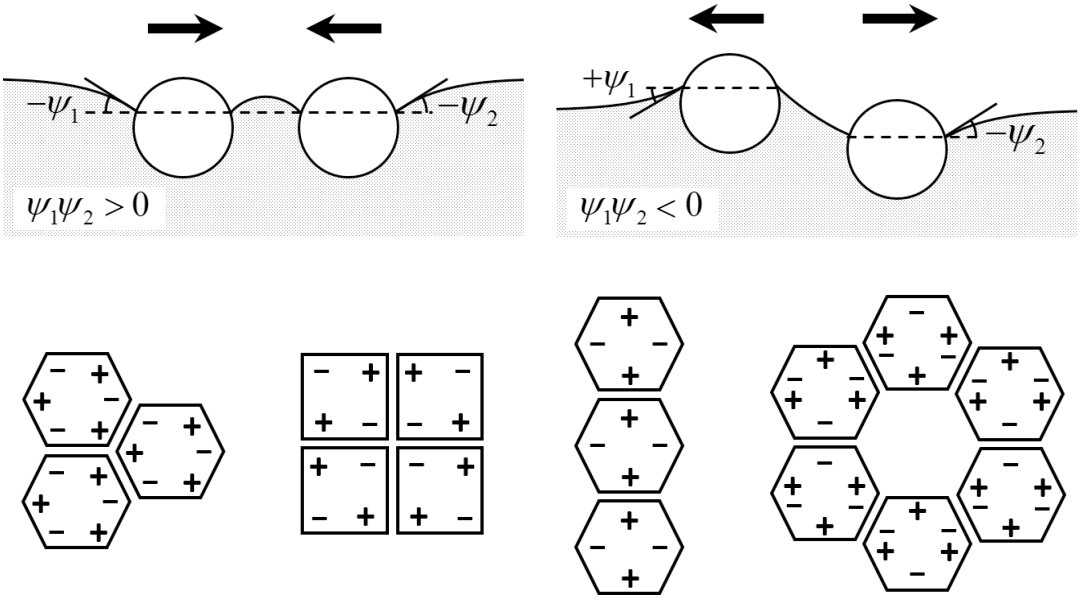

Figure 2.8 Lateral capillary interaction and self-assembly of particles at fluid interface. (Top) Capillary forces between particles. The sign of meniscus slope ψ_1 and ψ_2 at each particle determines the force direction (attraction or repulsion). (Bottom) Self-assembly of particles in two-dimensional arrays by capillary multipoles. + and – denote the signs of meniscus slope.

2.3.5.1 Lateral Capillary Force between Two Spherical Particles at a Cylindrical Fluid Interface

Following the derivation carried out by Zeng C., et al.,[65] we consider lateral capillary forces between two particles at a cylindrically curved interface. Particle 1 with radius a and particle 2 with radius b are placed at $(0,0)$ and $\mathrm{d}(\cos\omega, \sin\omega)$ respectively, where d is the separation distance and ω is the angle between two particles. At any point on the contact line, the capillary force is along the direction of a unit vector $\hat{\gamma}$ perpendicular to both the normal to the interface $\hat{n}_i$ and the tangent of the contact line

$\hat{\tau}_c$ (Figure 2.9). By integrating the forces around the contact line, the total capillary force on particle 1 is obtained as

$$F_c = \gamma \oint dl\, \hat{\gamma} = \gamma \int_0^{2\pi} d\phi \sqrt{a^2 \sin^2\theta_c + \left(\partial_\phi x\right)^2}\, \hat{\gamma}(\phi),$$

where γ is the interfacial tension, l is the length of the contact line, ϕ is the angular location with respect to the particle axis, θ_c is the contact angle, x is the height of the interface at the contact line.[65]

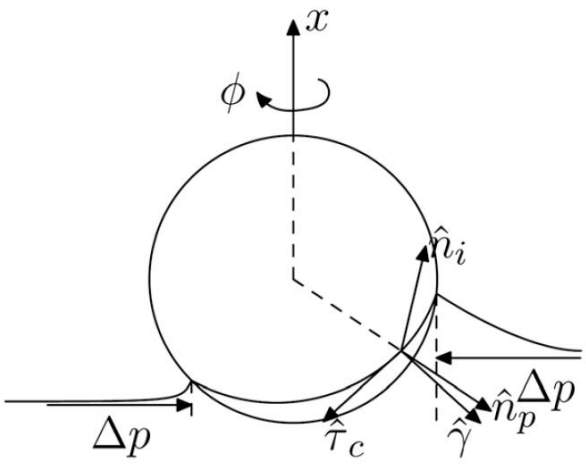

Figure 2.9 The forces on a spherical particle at a cylindrically curved fluid interface. $\hat{\gamma}$ is the capillary force direction, $\hat{n}_i$ is the normal to the interface, $\hat{n}_p$ is the normal to the particle surface, $\hat{\tau}_c$ is the tangent of the contact line, and Δp is the pressure difference across the interface. The figure is adapted from Zeng C et al., *Soft Matter*, 2012, **8**, 8582.[65]

The Laplace pressure $\Delta p = \gamma/\mathrm{R}$ across the interface (R is the cylinder's radius) also creates forces on the particle. The lateral component of this force in ρ, ϕ plane (ρ is distance from the particle axis on the interface) is given by

$$F_P = -\frac{\gamma}{R} \int_0^{2\pi} d\phi x(a \sin\theta_c, \phi)\, a \sin\theta_c\, \hat{\gamma},$$

where $x(a\sin\theta_c, \phi)$ is the height of the contact line. The forces normal to the interface is balanced by the capillary force. Finally, the total lateral force on particle 1 can be calculated by adding two contributions:

$$F(d,\omega) = F_c + F_p = -\frac{\pi\gamma a^4 b^4 \sin^8\theta_c}{3R^2 d^5}(\hat{z}\cos 5\omega + \hat{y}\sin 5\omega) + O\left(\frac{\gamma a^{10}}{R^4 d^5}\right).$$

CHAPTER 3

VISUALIZING THE DYNAMICS OF NANOPARTICLES IN LIQUIDS BY SCANNING ELECTRON MICROSCOPY

3.1 Introduction

Solvated soft materials, as exemplified by solutions, dispersions, and gels, play an important role in life and physical sciences, supporting dynamic processes such as flow, crystallization, self-assembly, and swelling. Key structural aspects of these processes are best understood when visualized on the nanometer scale using electron microscopy, a technique requiring high vacuum to achieve high resolution. As a consequence, liquid specimens are typically frozen before examination, eliminating their dynamics.[80] Even environmental scanning electron microscopy (ESEM), which achieves visualization of hydrated specimens under relaxed vacuum conditions, is limited in resolution and time due to water evaporation.[81] To monitor dynamics in solvated or dispersed specimens *via* transmission electron microscopy (TEM), specimens can be encapsulated in vacuum-sealed devices, *i.e.* liquid cells with silicon nitride windows, to prevent evaporation.[82-84] Cell handling can be challenging, beam damage for organic materials is inevitable, electron scattering from cell windows reduces image resolution and contrast, and interactions of the specimen with the cell walls can bias the dynamics. Some cell limitations are overcome by using graphene windows,[29, 85, 86] as shown by Zettl, Alivisatos and co-workers in imaging the diffusive motion of nanoparticles in an aqueous phase.[86] The atomically thick graphene layers reduced unwanted loss of incident electrons and significantly enhanced the contrast and resolution of imaging. For perfect sealing, however, flawless, large area sheets are needed, and the graphene windows

themselves can exhibit motion caused by electron beam exposure and fluid motion. The interactions of the nanoparticles with the windows, *i.e.* graphene, remains a concern. The vaporization of the liquid by electron beam exposure limits the time for continuous imaging of the dynamics.

Ionic liquids (ILs) offer an alternate approach for high resolution imaging of dynamics for solvated soft materials, one that circumvents the need for a liquid cell. Classified as salts that melt near or below room temperature, ILs possess vanishingly low volatility at ambient temperature and, therefore, are stable under high vacuum (10^{-5} to 10^{-7} Pa).[31] All types of soft matter states seen with traditional aqueous and organic solvents (gels, pastes, solutions, dispersion, *etc*.) are also found with ILs.[87-92] The motions of nanoparticles and polymers in ILs are the same as those in conventional organic and aqueous solvents.[93] Among the characteristic properties of ILs are intermediate polarity, moderate viscosity, high ionic conductivity, large liquidus range, and wide electrochemical window.[32] None of these properties hinder electron microscopy, and indeed, many would seem beneficial. High vacuum spectroscopy methods such as x-ray photoelectron spectroscopy (XPS)[94] have been applied to ILs on occasion, as have static TEM[95, 96] and scanning electron microscopy (SEM).[97] In an early contribution on nanodynamics, Ju and co-workers used an IL electrolyte to observe an electrochemically induced structural change in nanowires by TEM.[98] Likewise, Schubert and co-workers imaged the motions of diblock copolymer assemblies in an IL thin film by TEM,[33] and Uematsu and co-workers observed the growth of gold nanoparticles from an IL solution.[34] Many of these studies demonstrated difficulties from electron beam interactions with IL, and, in particular, that at the electron doses needed for suitable contrast, stable dynamics persisted for only seconds.

Nanomaterials did not necessarily diffuse by thermal fluctuations but also in response to the crosslinking or rupture of the IL film.

This chapter describes *in situ* SEM visualizations of dynamics for spherical nanoparticles, NPs, and nanorods, NRs, dispersed in ultra-thin free-standing IL films at room temperature (Figure 3.1). As extended image sequences (*i.e.*, movies), NP and NR Brownian motion were recorded at nanoscale resolution across large film areas (> 50 μm^2). Films thicknesses both smaller and larger than the particle diameters were prepared, and dispersed particle dynamics for the two differ significantly and sometimes unexpectedly. The imaging of NPs floated on the IL surface is also presented as a relevant work.

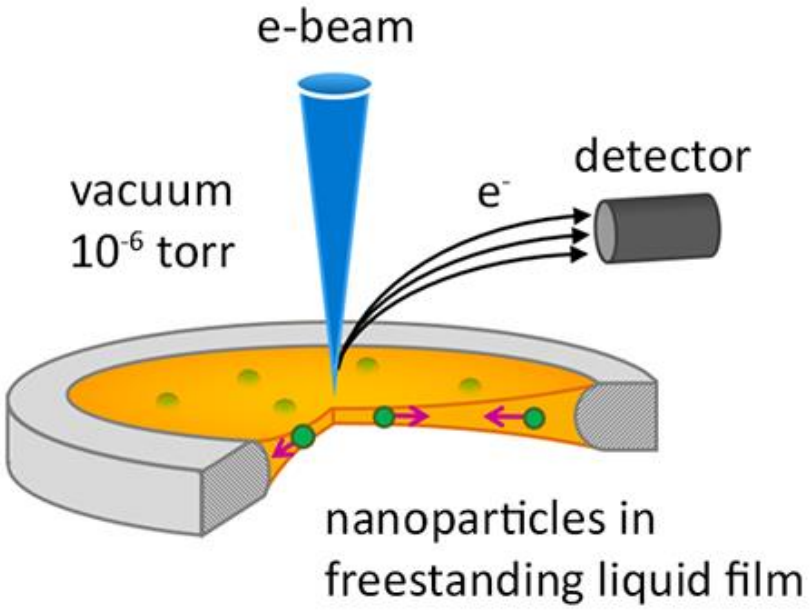

Figure 3.1 Observation of nanoparticle motions in freestanding ionic liquid films with scanning electron microscopy, which requires ultra-high vacuum

3.2 Experimental

3.2.1 Materials and Sample Preparation

Silica NPs and NRs were made by established sol-gel processes. By SEM, NPs had a 175 nm ± 10 nm diameter and NRs had a 103 ± 36 nm diameter and 393 ± 6 nm length. Gold-coated silica NPs (GSNPs) were purchased from Nanocomposix. Their core silica diameter was 120 nm and gold coat thickness was 20 ± 7 nm. To promote IL dispersibility, both NP and NR were surface-decorated with polyethylene glycol (PEG, 5000 g/mol), anchored by the condensation reaction between a succinimidyl ester endgroup of the PEG and the surface amine groups of the nanoparticle.[99] GSNPs were likewise decorated by PEG-thiol. Such steric stabilization was necessary, since ILs screen stabilizing electrostatic repulsions.[100] Dispersions in the hydrophilic IL, 1-ethyl-3-methylimidazolium ethyl sulfate ([emim][$EtSO_4$]), was accomplished by adding a small amount of nanoparticle-containing methanol to the IL, then removing the methanol and any volatile IL contaminants by passing dry nitrogen over the dispersion for 12 h.[101] Nanoparticles were stable against obvious aggregation for several months. A free-standing film was created by placing a drop of nanoparticle-IL dispersion on a lacey carbon-coated TEM grid and removing excess liquid by blotting with filter paper. The fibrous grids, ~30-nm thick, were chosen for their large mesh openings (1 to 150 μm in characteristic largest dimension). Electron micrographs of particles, lacey carbon, and free-standing liquid films are shown in Figure 3.2.

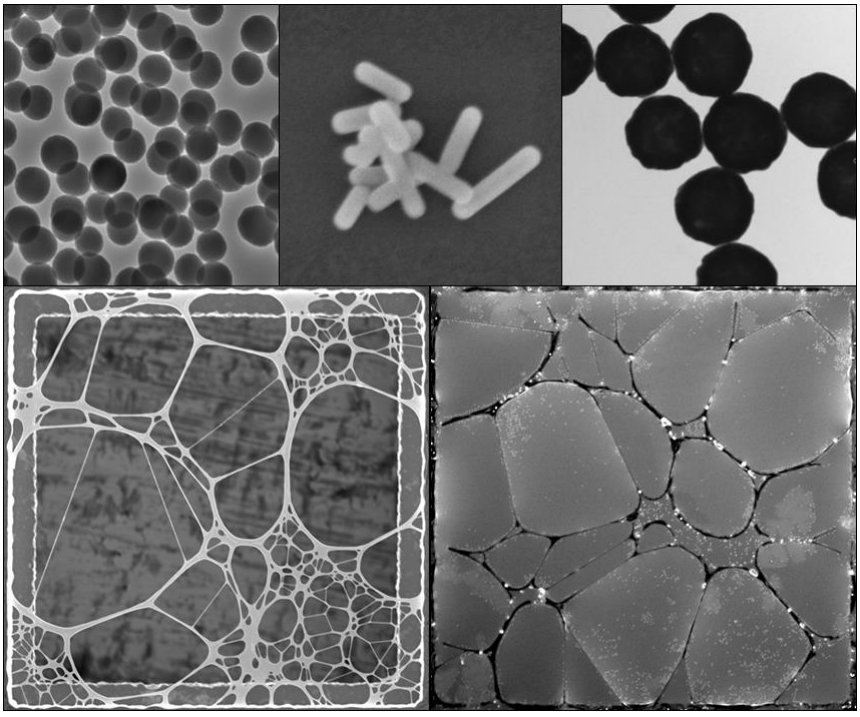

Figure 3.2 Electron micrographs of particles and substrate. (top left) silica nanospheres, (top middle) silica nanorods, (top right) gold-coated silica nanospheres, (bottom left) neat lacey carbon, (bottom right) freestanding liquid film of nanoparticle dispersion bridged on a lacey carbon.

3.2.1.1 IL Purification and Storage

1-ethyl-3-methylimidazolium ethyl sulfate ([emim][EtSO4]) was received as a gift (TEGO IL IMES; Evonik Goldschmidt GmbH, Essen, Germany), and the clear but amber-tinted liquid was subjected to 48 h stirring with activated charcoal and dichloromethane before sequential filtration through a column packed with diatomaceous earth (Celite545, Sigma-Alrich) and a PTFE 0.2-μm membrane (Whatman). After removing dichloromethane at reduced pressure, the hygroscopic IL was dried overnight in a vacuum oven at 60 °C before storage in a nitrogen glove bag.

3.2.1.2 Silica Nanosphere (NP) Synthesis

Tetraethyl orthosilicate (TEOS), 3-aminopropyl-trimethoxysilane (APS), ammonium

hydroxide, methoxypolyethylene glycol 5,000 acetic acid N-succinimidyl ester (PEG-SE), rhodamine B isothiocyanate (RITC), nickel (II) chloride hexahydrate ($NiCl_2$), diethylamine, and cyclohexane were purchased from Sigma-Aldrich; polyoxyethylene (20) cetyl ether (Brij 58) and hydrazine hydrate (100%, hydrazine 64%) were purchased from Acros; and sodium hydroxide (NaOH), hydrochloric acid (HCl, 37.5%), ethanol, methanol, and isopropanol were purchased from Fisher Scientific. To facilitate their characterization, NPs were doped during synthesis with fluorescent rhodamine B using a sol-gel process adapted from Zukoski *et al.*,[102] in which RITC and the silane-coupling agent APS were introduced during an initial phase of NP growth. In a 10 mL vial, 28 mg of RITC and 44 mg of APS were dissolved in 5 mL of ethanol with overnight stirring, and this solution was then poured into a 500 mL flask containing 176 mL of ethanol, 7.7 mL of ammonium hydroxide (29%), 4.6 mL of water, and 7.7 mL of TEOS. Adding 1.65 mL water and 10.18 mL TEOS every 2 h, NP diameter reached 170 nm after 6 h. Next, in a modification of the original recipe, the NPs were surface-functionalized with amine groups by adding 1.65 mL of water and 10.18 mL of 2:1 v/v TEOS and APS mixture during a final phase of NP growth. In a last step, these amine groups were reacted with PEG-SE end groups to form stabilized, PEG-grafted NPs.[99] In a 4 mL vial, 10 mg of PEG-SE and 100 mg of NPs in 1 mL of methanol were mixed under sonication for 3 h. The product was centrifuged, washed, and stored in methanol.

3.2.1.3 Silica Nanorod (NR) Synthesis

Silica NRs were templated, as described by Gao *et al.*,[103] from rod-like nanocrystals prepared by the hydrazine hydrate-induced precipitation of $NiCl_2$ dissolved in reverse micelles. To prepare these micelles, 8.5 g of Brij 58 and 15 mL of cyclohexane were

mixed in a 50 mL round bottom flask kept at 57 °C. After the mixture clarified, 1.9 mL of 0.8 M $NiCl_2$ aqueous solution was added with 1 h stirring to re-clarify the mixture. Drop-wise addition of 0.45 mL of hydrazine hydrate precipitated the $NiCl_2$. After 3 h of crystal growth, the templated deposition of silica was initiated by sequential addition of 1 mL of diethylamine and 1 mL of TEOS. Deposition continued for 2 h before the NR product was collected by centrifugation and washed with copious isopropanol. These precursor NRs were then refluxed in 100 mL of 10 v/v % HCl in ethanol to remove both nickel-hydrazine complex and Brij 58; the solid NR cores were etched away during the reflux. The now hollow NRs were isolated by centrifugation and washed with ethanol repeatedly before re-dispersal in 100 ml of ethanol. Silica growth was re-initiated by adding a further 4 ml of ammonium hydroxide (29%), 3 ml of water, and 1.5 ml of TEOS. As the NRs reached their target size, *i.e.*, 100-nm diameter, a final deposition was made by adding 0.3 ml of a 2:1 v/v mixture of TEOS and APS. The latter facilitated the surface grafting of PE-SE as described already for NPs.

3.2.1.4 SEM Specimen Preparation

Silica nanoparticles (either NPs or NRs) as well as GSNPs were dispersed in IL by mixing 100 μL of a 1~10 mg/ml dispersion in methanol with a solution combining 200 μL of IL and 300 μL of methanol. The methanol was removed by blowing dry nitrogen over the dispersion for 12 h. Just prior to microscopy, the IL dispersion was spread on a lacey carbon TEM grid *via* a glass capillary tube and any excess liquid was removed by blotting with filter paper. For mixtures, the two separate particle dispersions were combined and vortexed just before microscopy.

3.2.2 Characterization of Particle Diffusions in Bulk Liquids

The diffusion coefficient of silica NPs in IL was measured by dynamic light scattering. 1ml of NP dispersion in IL (0.1 % w/v) was filled in a quartz cuvette and then placed in Malvern Zetasizer Nano ZS. After stabilization for 15 min at 20˚C, the sample was incident to He-Ne laser 633 nm. The measurement was continued for 60 s at a scattering angle of 173˚. Silica NRs were not measured because of the spherical impurity.

3.2.3 Thickness Measurement of Free-Standing Liquid Films

Free-standing IL film thicknesses were evaluated at various sample locations using a JEOL JEM-2200FS Energy Filtered TEM in Electron Energy Loss Spectroscopy mode with the filter entrance aperture diameter set to 500 nm. Thickness was calculated by the log-ratio method: $\mathrm{t}/\lambda = \ln(I_t/I_0)$ where I_t and I_0 are total spectrum and zero-loss intensities, respectively; t is film thickness; and λ is the mean free path of electrons in the IL. The inelastic mean free path for IL film was calculated using an experimentally determined formula that has a smooth dependence on atomic number Z:

$$\lambda = \frac{106FE_0}{E_m \ln(2\beta E_0/E_m)},$$

where F is a relativistic factor, E_0 is the electron energy, $E_m \approx 7.6\mathrm{Z}_{\mathrm{eff}}^{0.36}$ is the average energy loss in eV), and $\mathrm{Z}_{\mathrm{eff}} = \sum_i f_i \mathrm{Z}_{\mathrm{eff}}^{1.3} / \sum_i f_i \mathrm{Z}_{\mathrm{eff}}^{0.3}$ is the effective atomic number of the components *i* in a specimen. The parameter estimated *via* a literature method[104] to be 302 nm for 5.3 mrad collection angle.

3.2.4 Simulation of Incident Electron Trajectories in Liquids Films

Incident electron trajectories in the IL for acceleration voltages 500 V, 3 kV, and 5kV were simulated by Monte Carlo methods (CASINO version 2.48). 200-nm thick film of IL ($C_8H_{16}N_2O_4S$, 1.24 g/ml) was assumed for calculation. Several physical models were adapted: cross section (Mott by interpolation)[105], effective section ionization (Casnati 1982)[106], ionization potential (Joy and Luo 1989)[107], random number generator (Pres 1986), directing cosine (Drouin 1997)[108], dE/dS calculation (Joy and Luo 1989)[107].

3.2.5 Imaging Particle Motions by Scanning Electron Microscopy

Movies were collected using a high-resolution SEM equipped with a field emission gun (FEI Magellan™ XHR 400 FE-SEM) and a quick sample load-lock and operated with software (FEI SmartSCAN™) that implements line-integration. SEM experiments were performed at 3-kV acceleration voltage and 100-pA beam current. Operating pressure was in the 3×10^{-6} - 8×10^{-6} torr range. Line-integration significantly reduces charging/heating artifacts. Multiple scans were averaged line-by-line to produce an improved quality, high frame rate (1-2 frame/s) composite image. Scanning was at 50 or 100 ns/pixel, and lines were averaged 20 times in final images (*i.e.*, individual frames). Scans were 512-pixels wide and 442-pixels high. These imaging conditions were found to optimize resolution and acquisition rate while maintaining sufficient contrast to identify individual particles and wide enough field of view to observe film edges or, as needed, to raise the number of particles monitored to improve the statistical analysis of their motions. Features somewhat below 5 nm could be identified at these conditions, a resolution much less than nanoparticle dimensions. While the ultimate resolution of SEM is even higher, the instrument cannot reach its ultimate resolution for visualizing these

systems without noticeable beam damage or significant reduction in the frame number of frames.

3.2.6 Image Processing and Dynamic Analysis

3.2.6.1 Identification of Particle Positions and Orientations

With all steps performed using Matlab, imaging processing began with a step enhancing the contrast between particles and IL by multiplying pixel values with themselves. Each pixel was then averaged with the adjacent eight pixels to reduce noise, and the averaged frame was transformed into a binary image by thresholding; particles became white (1) and background became black (0). White pixels were grouped, and groups with fewer than 5 pixels were discarded as noise. The center of mass of the larger groups (*i.e.*, particles) and the moment of ellipse inertia (orientation) for these groups were computed from pixel locations. The described method was not effective when the nanoparticles are in constant near contact, and particles have distinct contrasts. In this case, the particles were identified by fitting their edges to circles by Hough transform.

3.2.6.2 Connecting Particle Positions into Trajectories

Particle positions in each frame were matched with corresponding positions in later frames. Because particles were indistinguishable, the most probable set of trajectories had to be selected from all possible trajectories. The likelihood of each connection can be estimated by proximity in the different frames. For N non-interacting Brownian particles, the probability P to find particles at distance δ in plane after time τ is

$$P(\{\delta_i|\tau\}) = \left(\frac{1}{4\pi D\tau}\right)^N \exp\left(-\sum_{i=1}^{N}\frac{\delta_i^2}{4D\tau}\right),$$

where D is particle's diffusion coefficient. Therefore, the proper way to link particles in different frames was to select a set of trajectories, which maximizes $P(\{\delta_i|\tau\})$, or equivalently, minimizes the sum of particle displacement $\sum_{i=1}^{N}\delta_i^2$. To reduce the amount of calculation, displacements of particles were assumed to be less than a certain distance. A software developed by John C. Crocker and Eric R. Weeks was adapted for this process.[109]

3.2.6.3 Calculation of Mean Square Displacements

Brownian motions of particles were accessed by mean square displacement as a function of time lag τ. When signal-to-noise is poor, τ is re-defined as the time between any two frames. Rotational displacements between frames were assumed to be less than 90°, because rotations offset by 90° are indistinguishable.

3.2.6.4 Calculation of the Radial Distribution Function g(r)

To evaluate the position correlations among the particles, their radial distribution function was calculated

$$g_{2D}(r) = \frac{dn(r)}{2\pi r dr \cdot \rho},$$

where r is distance from a reference particle, $dn(r)$ is the number of particles at distances between r to $r + dr$, and ρ is the average areal number density of particles (0.105 /μm^2). For reference particles near a frame edge, a circle of radius r can extend beyond the edge. To compensate, the ratio $dn(r)/2\pi r dr$ of the preceding equation was evaluated for just the angular range inside the image.

3.2.6.5 Calculation of Tetratic Order Parameter $G_4(r)$

The degree of four-fold orientational (tetratic) ordering for the NRs was evaluated through the angular correlation function[110]

$$G_4(r_\perp \; or \; r_\parallel) = \langle cos\big[4\big((\theta_i - \theta_j)\big)\big]\rangle \, ,$$

where θ_i is the orientation of a rod with respect to a pre-selected axis, i and j are particle indices, and $r_\perp$ and $r_\parallel$ are respective components of the separation vector between rod centers perpendicular and parallel to the long axis of particle i.

3.2.6.6 Color Coding Grain Morphology of Self-Assembled Hexagonal Lattices

The NP ordering in hexagonal lattices was visualized by color coding the relative angular orientation of hexagons, including a central entity and its six nearest neighbors. The algorism designed by Martin Steinhart and co-worker was adapted for this calculation. Center-to-center distances were calculated for all pairs of NPs. By setting cutoff radius between the first- and second-nearest neighbor peaks, closest six neighbors were extracted for each NP. The orientation was calculated by averaging the angles between the vertical line and the lines connecting the center c and closest neighbors i. The angles were calculated by a trigonometric formula

$$\alpha_i = 180° \, \mathrm{atan}[(y_i - y_c)/(x_i - x_c)\,]/\pi,$$

which was adjusted between -30˚ and 30 ˚. The average angles were coded with colors for each NP. Along with lattice orientations, the average distances between each center and closets neighbors were color coded to visualize the local densities in hexagonal lattices.

3.3 Results and Discussion

3.3.1 General Observations

A free-standing film was created by placing a drop of nanoparticle-IL dispersion on a lacey carbon-coated TEM grid and removing excess liquid by blotting with filter paper. The fibrous grids, ~30-nm thick, were chosen for their large mesh openings (1 to 150 μm in characteristic largest dimension). IL bridges spontaneously formed across the openings at thicknesses of 30 to 90 nm, as measured by energy electron loss spectroscopy (EELS); variations in the size and shape of the lacey carbon grid openings lead to this non-uniformity, as shown in Figure 3.3. Because EELS is performed in a TEM, assigning an EELS thickness to a particular film imaged by a SEM was impossible. Due to the moderate surface tension[111] (49.3 mNm^{-1}) and viscosity (125 mPa·s) of ILs, the bridges were stable for hours, providing sufficient time for the SEM experiments (a few minutes).

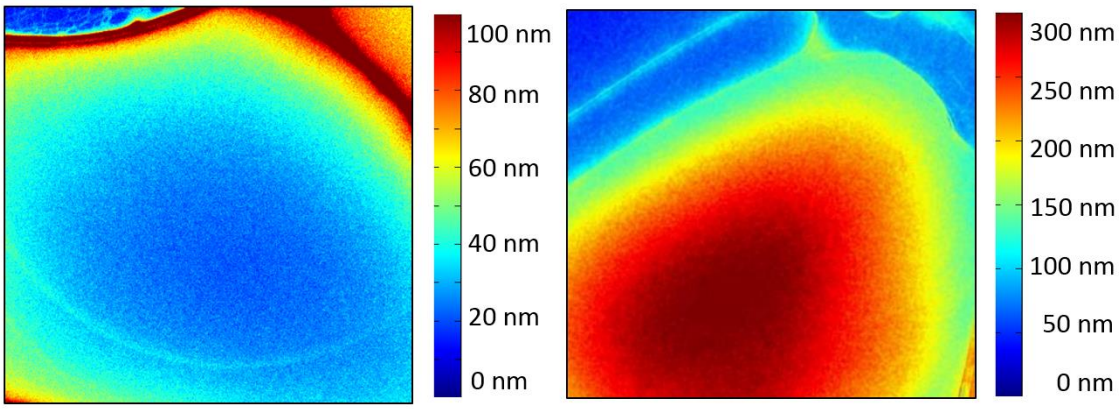

Figure 3.3 Thickness map of freestanding ionic liquid films, measured by electron energy loss spectroscopy. (Left) Film center is thinner than periphery, which happened for most cases (Right) Film center could be as thick as 300 nm.

The excellent wetting characteristics of the IL allowed both the NPs and NRs to be fully confined within the IL films, aligning the NRs in the film plane. SEM images taken

from opposite sides of a film showed identical particle features, verifying internal confinement rather than surface attachment. When the film thickness was less than a NP diameter, the liquid-vacuum interface must deform locally to encompass the wetted particle symmetrically. At such thickness, if two NPs approach each other or the film boundary, overlap of the deformed interfaces induces a capillary interaction. For two particles, the interaction is attractive,[79] and more generally, the interaction drives particles toward regions of greater film thickness.[112] Because the films tended to be thicker at their periphery, dispersed particles slowly concentrated in this region and eventually a crowded, two-dimensional packing developed. To evade this outcome in the study of dilute dispersions, images were taken within 15 min of film preparation, before particle drift was discernable. Individual particles, as well as particle assemblies/aggregates (if any) away from the IL film boundary were *always* mobile.

Incident (primary) electrons can adversely affect a specimen through heating, electrostatic charging, radiolysis, displacement damage, sputtering and hydrocarbon contamination, with their impacts typically proportional to the electron dose.[113] Effects that induce flow are a particular concern for ILs. Because of the high voltage of the electron beam the rapid radiolytic crosslinking of ILs during TEM can be problematic. This crosslinking, which slows and eventually quenches dynamics, is essentially independent of IL chemistry/class and little affected by an added free-radical scavenger. With the beam voltage adjustable, SEM better circumvents deleterious electron beam-IL interactions.

In SEM, the penetration depth or mean free path of primary electrons increases with beam voltage (kinetic energy), revealing features at greater depths from the surface. For

low atomic number (Z) materials such as ILs, secondary electrons, of typical energy between 50 and 500 eV, characteristically escape from depths up to about 10 nm. As shown by the SEM images of Figure 3.4, NPs in ultra-thin IL films are undetected by SEM at 0.5 kV, marginally detected at 1 kV, and readily discerned at 3 kV. To interpret this trend, primary electron trajectories in the IL were simulated by Monte Carlo methods (CASINO version 2.48), as shown in the same figure. At 500 eV, because of shallow penetration, essentially all secondary electrons are created within the top 5 nm, but at 3 kV, with deeper penetration, a small but finite fraction are created beyond 10 nm. The observations establish that an IL layer of intermediate thickness (roughly 5-10 nm) wets and covers the silica nanoparticles. Further, at both 3 and 5 kV, all particle features have nearly the same, uniform apparent sizes and intensities, additional evidence that particles reside at a single depth, *i.e.*, the film mid-plane.

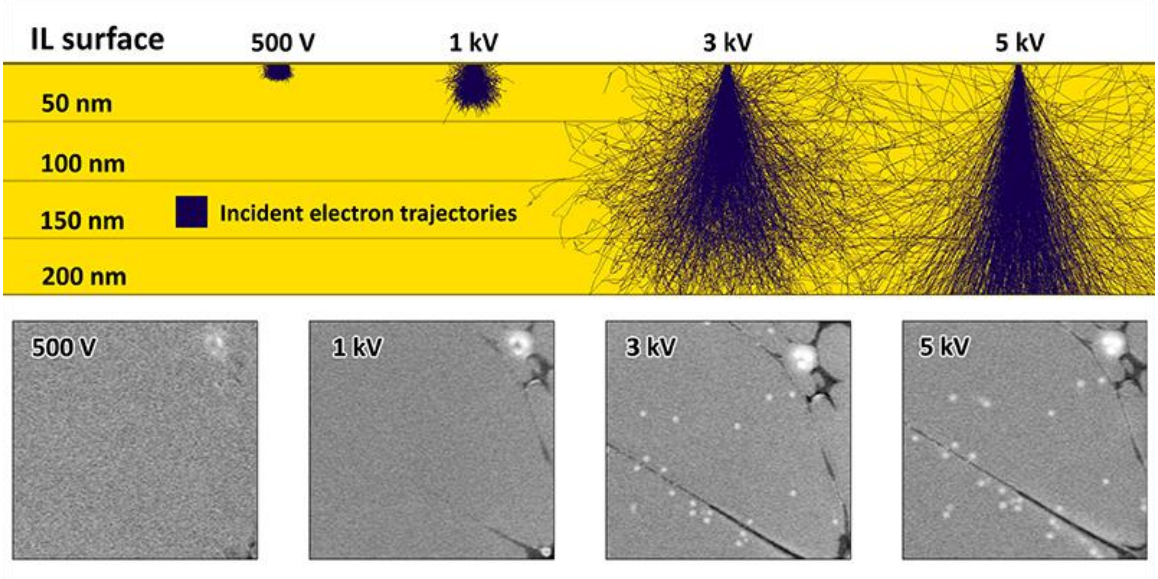

Figure 3.4 Effect of electron acceleration voltage on SEM imaging depth. (Top) Trajectories of incident electrons in IL simulated by Monte Carlo. (Bottom) SEM images taken at different electron acceleration voltages of NPs dispersed in IL films. The width of images is 5.7 μm. Black lines in image are lacey carbon.

Although ion conductivities of ILs are high,[114] their electrical conductivities are low,[115] making charging artifacts a serious concern. However, IL cations efficiently capture energetic electrons[116] with the resultant neutral radicals transported by fast hopping rather than diffusion.[117] ILs thus behave in SEM as electrically conducting,[97] mitigating charging effects. Bulk IL flow, probably from beam heating, is apparent above 5 kV, setting an upper voltage limit. At the lower voltages that offer ample imaging contrast (~1-3 kV), crosslinking is slow but not absent. Collecting 1 frame per 500–1000 ms at 6500x or higher magnification, IL properties, particularly the viscosity, remain constant for ~30 s, as demonstrated in the NP experiments described next.

3.3.2 Diluted Nanosphere

Figure 3.5 shows a single frame 'snapshot' of ~200 NPs uniformly dispersed across a 11.2 x 9.7-μm IL film area. Features of nearly uniform size and intensity are imaged, consistent with NPs at the film mid-plane. As established in the associated full 98 s movie (Movie S1), the individual particles do not change in brightness, do not appear or disappear (except at frame edges), and do not overlap each other as they undergo random thermal displacements with time. They appear bright against the background because silica has a higher electron scattering contrast (greater atomic number) than IL. Over large length scales, correlations in the displacements are not evident, suggesting that bulk flow is inconsequential, and over time, the mean square NP displacement between frames is approximately constant.

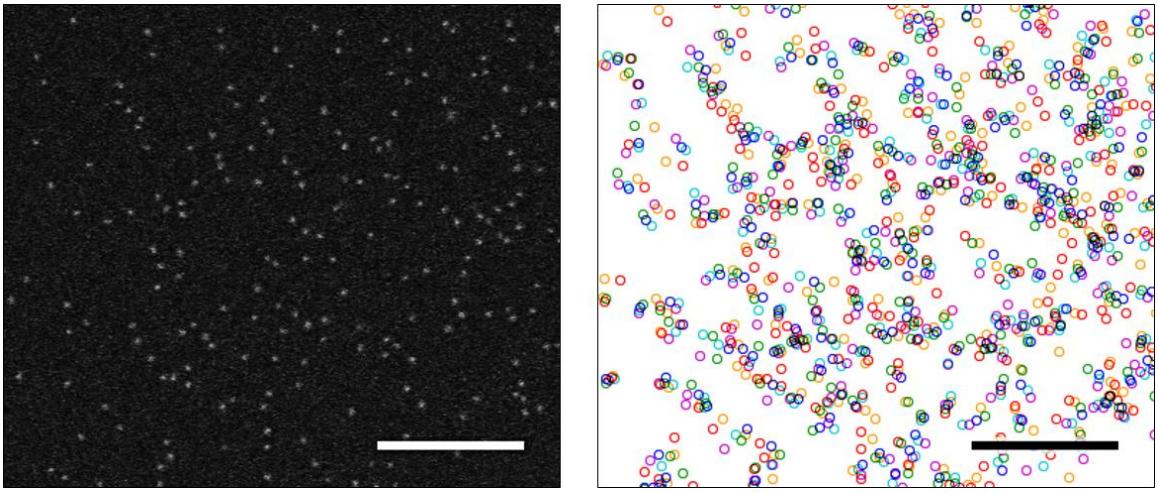

Figure 3.5 NPs imaged in an IL film. (left) Snapshot of ~200 NPs across a 11.2 x 9.7-μm IL film area. (right) Overlaid particle locations from six consecutive frames. The scale bar is 3 μm.

The preceding description is consistent with two-dimensional Brownian motion. To verify this, trajectories at a lower NP areal density (~20 per 11.3 x 9.8 μm) are tracked in Figure 3.6 (data extracted from Movie S2). Figure 3.6 also shows the corresponding mean square displacement $\langle \Delta \vec{r}^2 \rangle$ vs. time τ from the start of the movie. Confirming Brownian motion, $\langle \Delta \vec{r}^2 \rangle$ is nearly linear in τ for τ<30 s. Fitting data over this range with the equation for two-dimensional Brownian motion, $\langle \Delta \vec{r}^2 \rangle = 4D\tau$, uncovers a diffusion coefficient D of 0.0205 μm^2/s. For a dilute NP dispersion in an unbounded fluid, the Stokes-Einstein equation, $D = k_B T/6\pi\eta R$, where η is viscosity and R is radius, provides D = 0.0202 μm^2/s, almost the same as found by dynamic light scattering (D = 0.0186 μm^2/s at 20 °C). Despite the difference in geometry between theory and SEM experiment, *i.e.*, bulk vs. film, the agreement is excellent. For τ>20-30 s, $\langle \Delta \vec{r}^2 \rangle$ vs. τ appears to become sub-diffusive, reflecting the viscosification induced by IL crosslinking, and indeed, at very long times, the NPs become motionless.

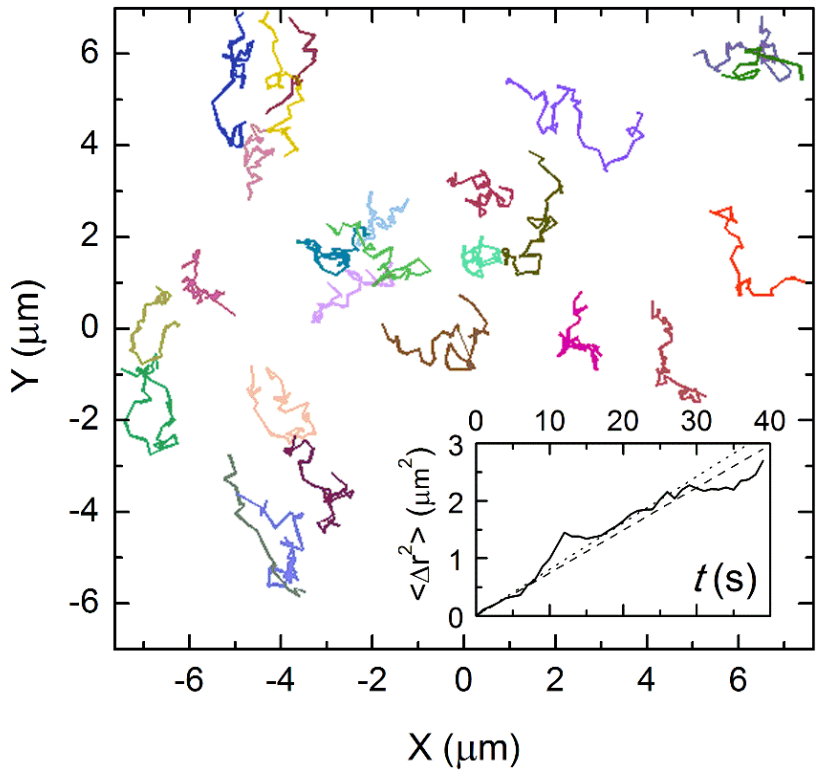

Figure 3.6 Trajectories over 40 s for NPs in an IL film thicker than the NP diameter. Inset: time dependence of mean square displacement as measured by SEM (solid), calculated from Stokes-Einstein equation with input of dry NP diameter (dotted), and derived from separate dynamic light scattering experiment (dashed).

To confirm viscosification induced by IL crosslinking, the distribution of mean-square displacements $\langle \Delta \vec{r}^2 \rangle$ for a single nanoparticle over 1 s was evaluated as a function of the time *t* since the start of imaging for the NPs of Movie S2. The resulting plot, given as Figure 3.7, shows that NP diffusion slows with *t*, a trend attributed to IL viscosification due to beam-induced crosslinking. Supporting this cause, XPS characterization of IL before and after imaging revealed complicated differences. For the imaging conditions chosen, the slowing is not apparent for $t<30$ s, so to be conservative, this period was chosen for the analysis of particle trajectories to determine diffusion coefficients. The same protocol to monitor beam-induced crosslinking was repeated for this, and many

other, imaging conditions, with the trends always similar to the one presented in Figure 3.7, although the length of the period preceding the appearance of viscosification depended on beam voltage and other experimental parameters. As shown in the inset to Figure 3.6, analogous plots of overall $\langle \Delta \vec{r}^2 \rangle$ vs. τ are initially linear, but after approximately the same period, they depart from this dependence, manifesting the slowing of NP motion. By substantially reducing crosslinking, SEM can image soft matter dynamics quantitatively over larger time spans than TEM.

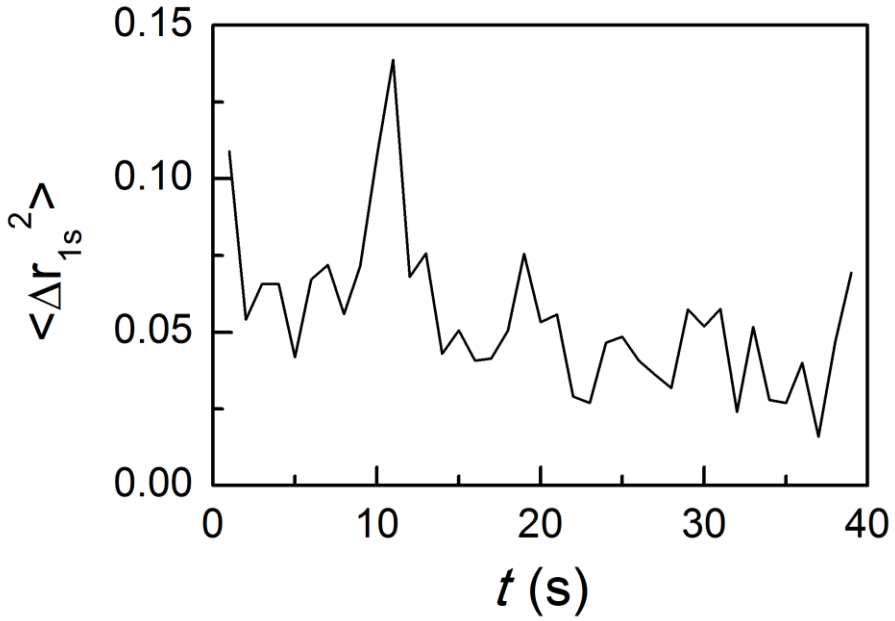

Figure 3.7 $\langle \Delta \vec{r}^2 \rangle$ for a short time lag (τ=1 s) vs. *t* for NPs imaged in Movie S2. The slight downturn at *t*≈ 30 s is a consequence of beam-induced viscosification.

Film thicknesses for the openings across a single grid, assessed at centers, ranged from 20 to 300 nm, with a thickness of 40-50 nm being most common. Literature suggests a close correspondence between bulk and thin film D values only when the film thickness exceeds NP diameter.[112, 118, 119] As indicated by the EELS results, just a fraction of the grid openings support films of such a large thickness, and thus not too surprisingly, the

fraction of openings supporting the motions described in conjunction with Figure 3.6 was similarly small. More frequently, the film thickness was less than the NP diameter, forcing the near planar IL-vacuum interface to deform about each NP, and in this regime, NP motions were more complicated. Naively, random Brownian motion biased by capillary attraction might be expected, with the trade-off between the two effects mediated by the ratio of film thickness to NP diameter. At long times, NPs influenced by capillary attraction would aggregate. Instead, at experimentally accessible τ's and in areas away from the film edges, strong interparticle correlations in position and displacement were found, even for well-separated NPs. Strikingly, as is evident for the dilute particles (~4 per 11.3 x 9.8 μm) tracked in Movie S3, NPs often formed virtual pairs, the partners sluggishly fluctuating in separation as they swirled rapidly about each other. Partners characteristically remained together for several seconds, and occasionally, especially at high sphere concentrations, partners exchanged during close approach. An optical microscopy study reported essentially the same motions for colloidal spheres dispersed in thin soap films.[120]

From the many possible positions and displacement correlations, we address only the radial distribution function $g(r)$, representing the number density of NPs a distance r from an arbitrary reference NP. For r beyond the range of the NP-NP interaction potential, random NP positioning was anticipated, corresponding to $g(r)$ equal to unity. Remarkably, for the NPs tracked in Movie S3, in addition to a peak at ~0.2 μm for particles in contact, $g(r)$ (Figure 3.8) displays a larger peak at ~0.5 μm. NPs in contact remain so permanently, presumably reflecting a large capillary attraction. The peak at larger separation is unambiguously assigned to the aforementioned virtual pairs, a

population more difficult to explain. Inter-particle displacement correlations also manifest the pairing, with this phenomenon most evident at lower NP areal densities, where, unfortunately, imaging-based assessments of $g(r)$ suffer from poor statistics.

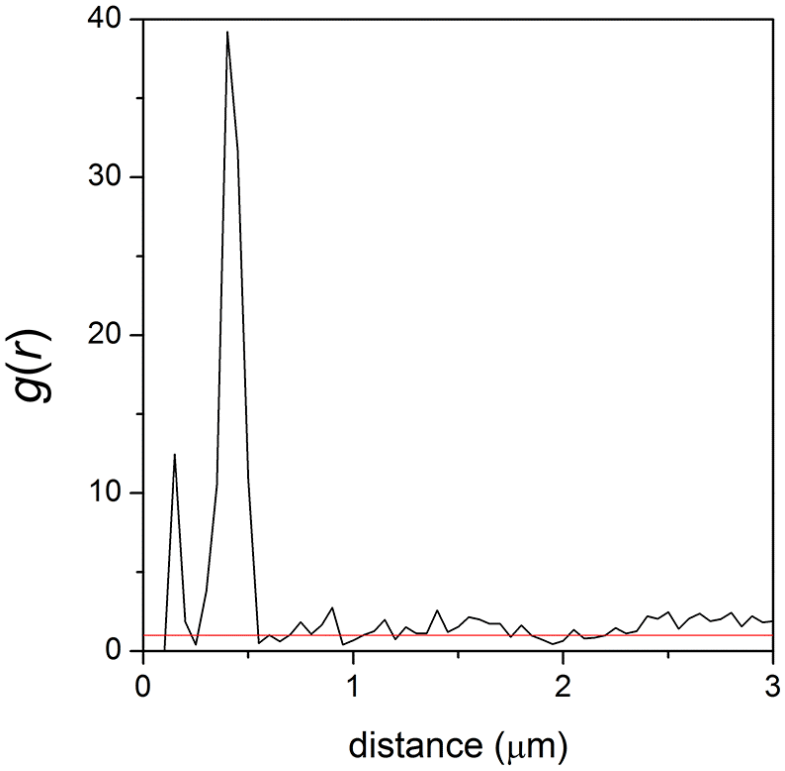

Figure 3.8 Pair distribution function g(r) for NPs of Movie S3. The peaks at ~0.2 and ~0.5 μm correspond to NPs in irreversible contact and in virtual pairs, respectively. The red line plots $g(r) = 1$, as appropriate for random NP positioning.

We argue that the pairing reflects the extraordinary range of hydrodynamic interactions in a thin fluid film bounded on each side by vacuum. Through these interactions, motion of a single particle leads to velocity disturbances that affect motions of distant particles. Hydrodynamic interactions in thin liquid films were analyzed by Saffman and Delbrück, who found that they propagate over a characteristic length $h(\eta/\eta')$, where h and η are the film thickness and viscosity, respectively, and η' is viscosity of the surrounding

medium.[73] For vacuum, η' is zero, and hydrodynamic interactions persist across the entire film, coupling the motions of all particles, and even making film size and shape affect these motions. How hydrodynamic interactions stabilize pairs remains unclear, and capillary attraction is likely important. The timescale of specimen preparation could affect the measured $g(r)$, as the tens-of-minutes experimental timescale might be too short for the equilibration of NP dynamics, and if so, $g(r)$ corresponds to a reproducible but metastable state.

3.3.3 Nanosphere Mixture

The intensity of electron backscattering depends strongly on the atomic number of the probed region, providing a compositional contrast mechanism for SEM imaging.[39, 40] Figure 3.9 compares micrographs of silica NPs and GSNPs on a solid substrate. Although the imaging conditions were identical, gold appeared brighter than silica by additional signals from backscattered electrons. This feature allowed labelling of certain particles by coating with different materials. Figure 3.10 shows silica NPs and GSNPs dispersed together in IL and imaged at 3 kV, the lowest voltage achieving good contrast between NPs and GSNPs. The GSNPs appear brighter, and consequently, slightly larger than the bigger silica NPs. As noted before, capillary interactions concentrate nanoparticles at the film periphery, where they retain high mobility unless in direct contact with the lacey carbon. At the ~57% nanoparticle areal coverage in the peripheral film region of Figure 3.10, single isolated GSNPs underwent caged diffusion among the surrounding NPs, as demonstrated in Movie S4, from which the figure was extracted. Over the experimentally accessible timescale, GSNP diffusion was sub-diffusive, with $\langle \Delta \vec{r}^2 \rangle \sim \Delta t^{\gamma}$, where γ is 0.77 for t = 1-25 s. When the GSNPs occasionally collide, they tend to adhere

irreversibly to each other (Movie S4, ~7 s), forming dimers and higher aggregates that diffuse differently among the NPs than the single GSNPs. Collisions between NPs or between NPs and GSNPs, on the other hand, do not lead to adherence. A GSNP dimer imaged in Figure 3.10 predominately hopped from one NP cage-structure to another by diffusing along the general direction of its axis. Locally, the NPs at this density assumed a noticeable hexatic order characterized by large positional fluctuations, with cages defined by GSNP occupation of a lattice site. Despite the caging, rotational diffusion of the dimer is apparent, and as with translational diffusion, predominately accomplished by hopping.

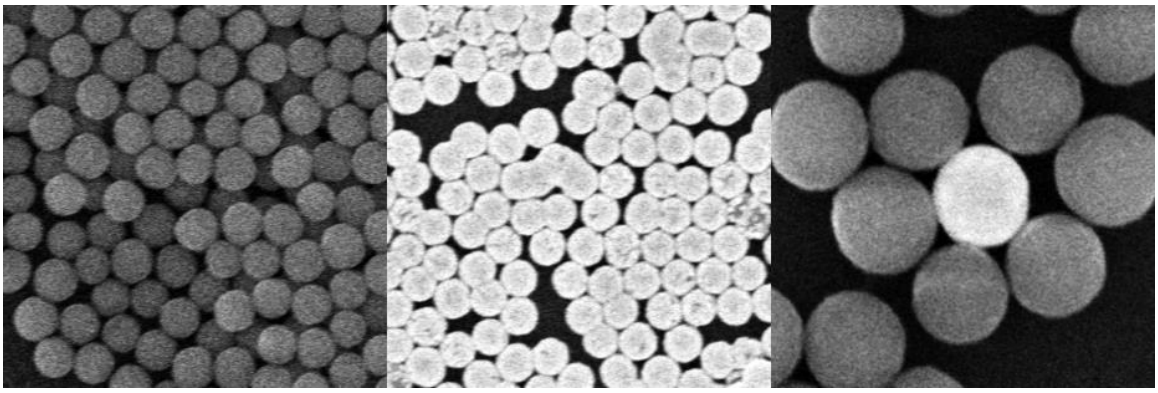

Figure 3.9 NPs, GSNPs, and their mixture on carbon films from left to right. All micrographs were taken at the same imaging conditions (acceleration voltage 5 kV beam current 25 pA)

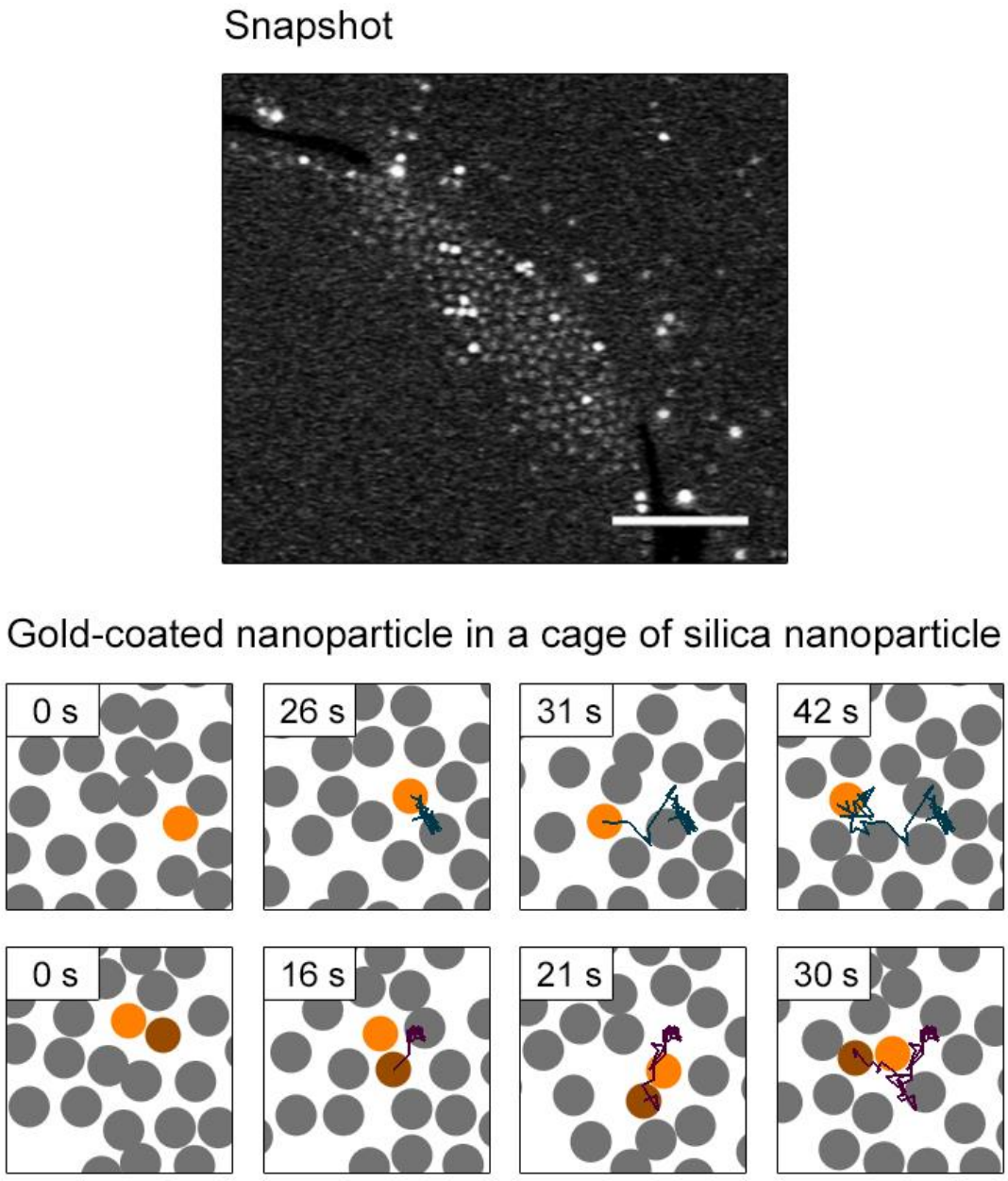

Figure 3.10 NPs and GSNPs mixed at the periphery of an IL film. (top) GSNPs appear bright and NPs appear dark in a raw movie frame. (bottom) Image sequences for diffusion of single (top row) and dimer (bottom row) GSNP at ~57% areal coverage of surrounding NPs. The scale bar in the snapshot is 2 μm. The width of each box is 1.6 μm. The curve traces the center of mass position of the GSNP over preceding frames.

NP positions were determined by an algorithm described in Chapter 3.2.6, and relative position accuracy was determined by applying this algorithm to the occasional image series for NPs stuck on lacey carbon. The measurement uncertainty in NP position is illustrated through image analysis of Movie S4. During the movie span of 82 s, the entire specimen, including carbon grid, drifted by 115 nm. To compensate for the drift, positions of NPs adhered to the lacey carbon film were tracked, identifying their positions by the algorithm described in the Experimental section. Six such NP trajectories are overlaid in Figure 3.11. Positions of mobile NPs in the IL were corrected by subtracting the average of these trajectories. Figure 3.12 displays twice the root-mean-square radial deviation of the corrected measured position vs. *t* (*i.e.*, for each successive movie frame) for the NPs adhered to the lacey carbon. The average of this deviation, termed the "2drms" measure of radial error, is 4 nm. The accuracy of NP and GSNP positions, assessed as twice 2drms, was 8 nm, indicating that 98% of measured positions lie within 8 nm of real positions. This error reflects the imaging resolution, sacrificed to some extent by lowering the magnification to expand the field of view and limiting the beam dose to increase the number of collectable frames. The insets to Movie S4 use particle position information from the movie to trace in time at highest resolution the motions of a GSNP single particle and a GSNP dimer amidst their NP neighbors.

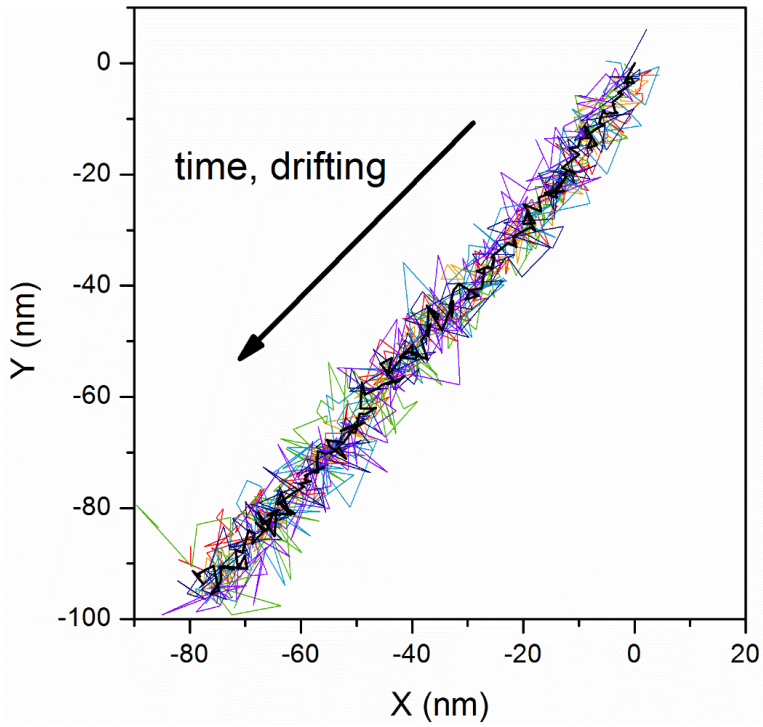

Figure 3.11 Trajectories of six adhered NPs in Movie S4. The bold line is the average of the trajectories.

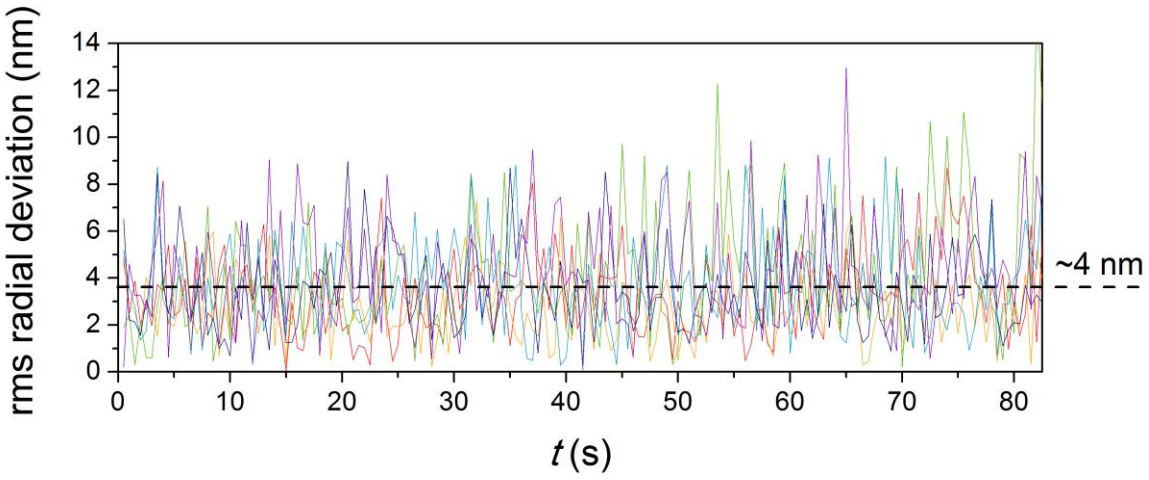

Figure 3.12 Root-mean-square radial deviation of measured NP position from average NP position as a function of time. The average deviation was 4 nm.

3.3.4 Concentrated Nanospheres

NPs were immobile at >70% areal coverage because they were trapped strongly by steric repulsions. The monodisperse size distribution allowed NPs to be packed closely into two-dimensional hexagonal lattices as shown in Figure 3.13. The quality of grain ordering was visualized by color coding the average distances and the orientations between NPs and their closest neighbors. Capillary interactions concentrated nanoparticles at the film periphery, forcing close-packing of NPs. Near the center of the film, however, NPs were separated at longer distances. The grain orientation was determined by the shape (*i.e.* lateral curvature) of the liquid film, because each grain was nucleated from the film edge. The orientation map shows that each grain matches their orientation with the slope around the film periphery. The long-range ordering was frustrated when the film had high curvatures.

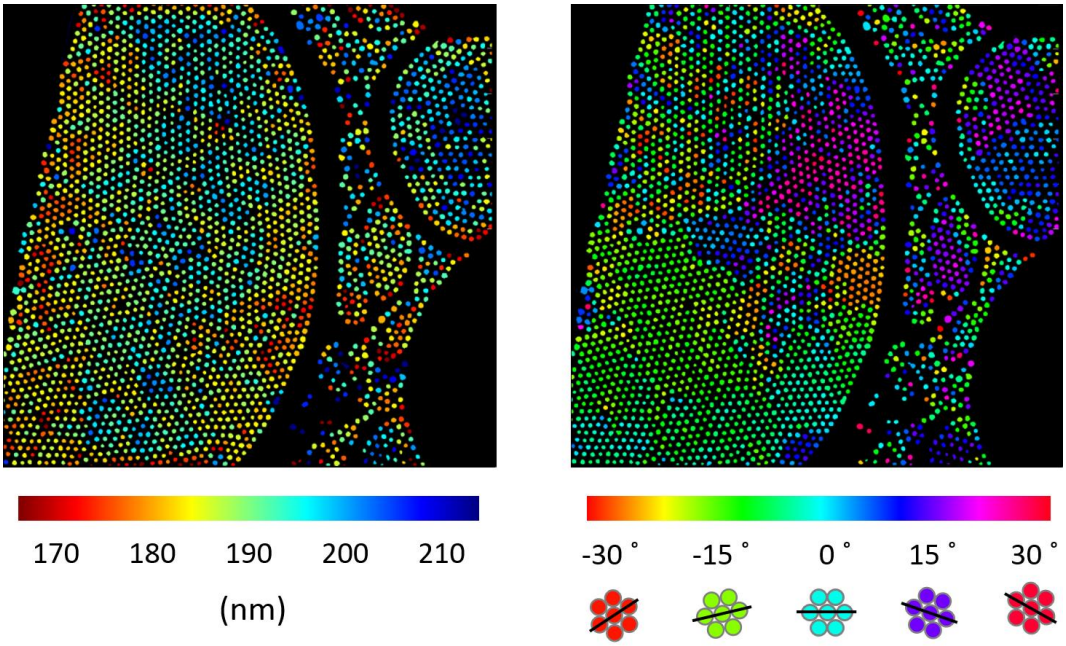

Figure 3.13 NPs in freestanding IL film at >70% areal coverage. (left) color map of average distances between nearest neighbors (right) color map of relative orientation of hexagons including a central entity and its six nearest neighbors.

3.3.5 Isolated Nanorod

NRs pose a bigger imaging challenge than NPs, as orientation is more difficult to capture than position, and displacements of the latter are anisotropic for times less than the rotational diffusion time $\tau_r = 1/(2D_r)$, where D_r is the rotational diffusion coefficient. Here, NRs were accompanied by a fraction of NP impurities, a further complication. Fortunately, all NPs and NRs are well resolved by SEM in each frame, allowing correlations in and between the two particle types to be calculated. A single, isolated NR is the simplest case, but with the ratio of film thickness to rod diameter less than unity, hydrodynamics are still not trivial. Movie S5 displays motions of a NR near the middle of a grid opening. The 30 s movie duration is more than an order-of-magnitude greater than τ_r calculated for the bulk fluid, 1.4 s. Figure 3.14 plots the mean square rotational and translational (center of mass) displacements vs. τ, and for τ<30 s, spanning 62 frames, both displacements display the linearity expected for Brownian motion. (Because rotations offset by 90° are indistinguishable, rotational displacements between frames were assumed to be less than 90°. And, to improve signal-to-noise, τ is re-defined as the time between any two frames.) Sub-diffusive trends for τ>30 s are attributed to viscosification by crosslinking. According to theory for an isolated rod in bulk fluid, $D = k_B T(\ln(L/b) + \gamma)/4\pi\eta L$ and $D_r = 3k_B T(\ln(L/b) + \delta_T)/\pi\eta L^3$, where L/b is the ratio of length to diameter, and γ and δ_T are constants (~0.45 and ~-0.44, respectively).[69-71] Fitting data for τ<30 s, D is 0.015 μm^2/sec, close to the predicted 0.016 μm^2/sec, and D_r is 0.13 radians^2/sec, reasonably close to the predicted 0.46 radians^2/sec. Given the limited statistics and dimensionality (quasi 2D vs. 3D) difference, the theory-experiment agreement is better than expected.[16, 121]

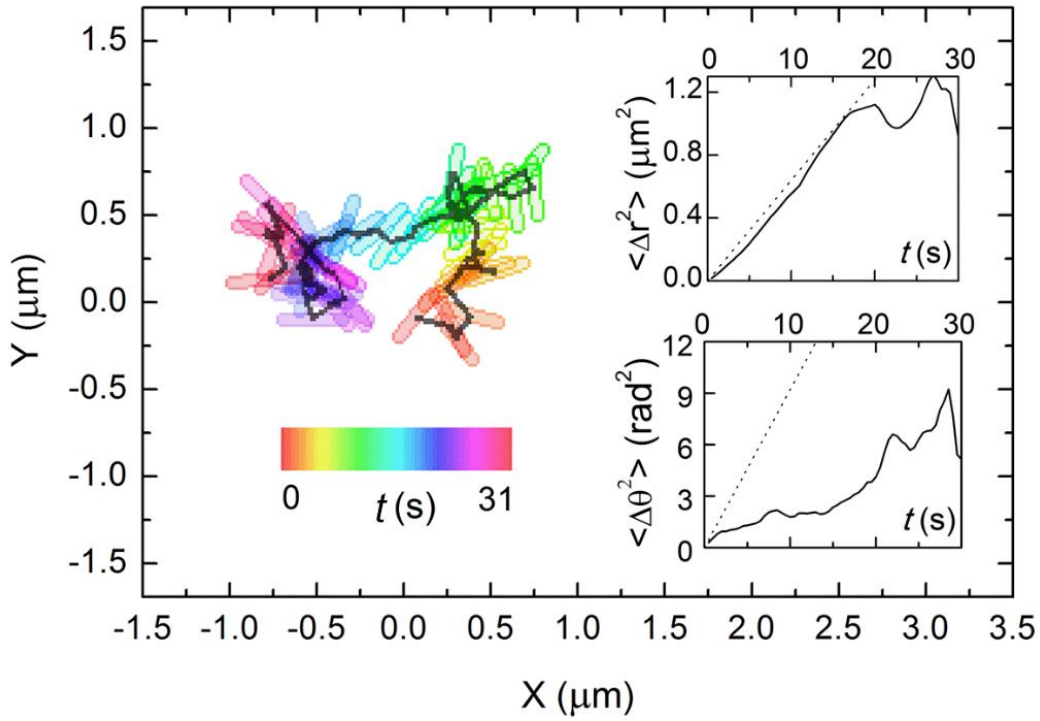

Figure 3.14 Position and orientation over a time lag t=0-31 s for a single, isolated NR in an IL film. Insets: time dependence of measured (solid) and theory (dotted) mean square displacements of position (top) and orientation (bottom).

3.3.6 Concentrated Nanorods

Movie S6 shows NR dynamics at ~60% areal coverage, and the first column of Figure 3.15 collects the 0, 10, and 20 s frames. Although the structure and dynamics for this high coverage are too complicated to discuss here fully, the basic information, individual NR orientation and position, can be extracted for every NR in each frame. At small τ, non-intersecting local NR displacements are relatively rapid, and a τ crossover between anisotropic and isotropic mean displacement is clear. A tendency for neighboring NRs to stack is even more evident. Defining a stack as a collection of NRs with center-to-center neighbor separations less than one-half of the NR length and orientational misalignments less than π/6, the second column of Figure 3.15 distinguishes stacks by color.

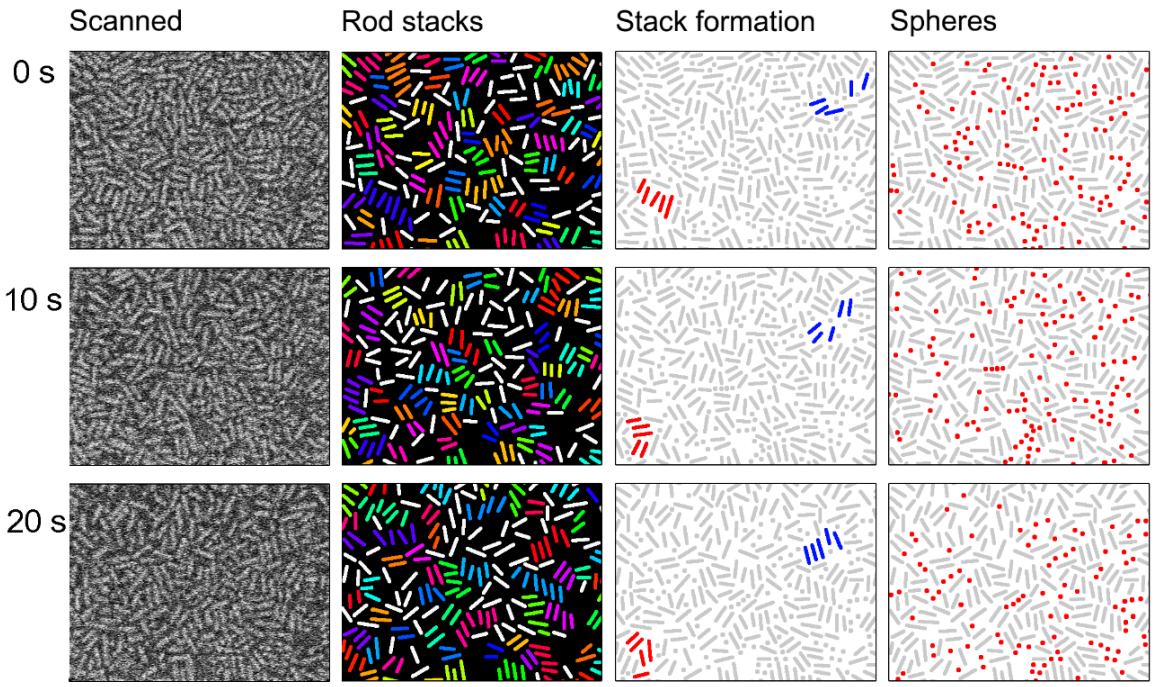

Figure 3.15 Concentrated (60% areal density) NRs in an IL film at three times. Column 1, raw images; column 2, NR stacks identified by color (unstacked NRs in white); column 3, four NR stacks highlighted to illustrate simultaneous ordering and disordering; and column 4, NPs (red) distributed among NRs (gray).

The stack size (number of NRs) ranges from 2 to 8, with the average size equal to 2.7, and at any given time, ~30% of the NRs are unstacked. Although Brownian motion makes NR arrangements transient, the average number of stacks and their mean size remain approximately constant. The third column of Figure 3.15 emphasizes the transience, highlighting two stacks that oppositely order and disorder over the movie τ span. NRs with an aspect ratio of ~4 are expected to pack in a dense monolayer with 4-fold rotational (tetratic) symmetry,[122] but the tetratic order parameter here remained small, either because of insufficient concentration or interruption of ordering by NP impurities. For the same 3 frames, Figure 3.15 (fourth column) graphically depicts both NRs and NPs, and a close examination shows that the NPs tend to adopt necklace-like structures between grains of the NRs. With an average diameter nearly equal to the average NR

diameter, the NPs often align 3 or 4 in a row to fill space locally, much as would a single NR. Such NR-NP spatial correlations clearly carry over to NR-NP dynamic correlations, although these correlations are not yet addressed.

3.3.7 Nanospheres on Liquid Surfaces

The bare IL surface, uncovered with other materials, allowed to image nanoparticles floated on the IL. A small IL droplet less than 1 mm in diameter was placed on a low-resistivity silicon wafer (Silicon Prime Wafers, boron doped, 0.001-0.005 Ω·cm) for reduced electron beam charging. After then GSNPs in methanol was applied on the top of the IL droplet. The particles were washed just prior to the sample preparation, because contaminants can remain on the surface and influence the interfacial dynamics. Methanol evaporated after spreading instantly over the IL surface. Despite good miscibility between methanol and the IL, the evaporation of methanol was much faster than mixing with the IL, leaving most particles on the surface. The particles were trapped on the surface and motions were confined in two-dimensions.

Movie S7 shows diffusions of an isolated GSNP on the IL. The movie was collected for much longer time (104 s) without noticeable artifacts due to reduced viscosification of the IL (crosslinked IL at the surface diffused into the bulk). NPs were visible at the lowest acceleration voltage of 500 V, because the particles were exposed directly to the vacuum. Trajectories of the GSNP is shown in Figure 3.16. The same figure plots the corresponding mean square displacement $\langle \Delta \vec{r}^2 \rangle$ vs. time τ, where τ is defined as time between any two frames. Linear $\langle \Delta \vec{r}^2 \rangle$ confirmed Brownian motion. The fitting data with $\langle \Delta \vec{r}^2 \rangle = 4D\tau$ returns D=0.0194 μm^2/s, smaller than D=0.0237 μm^2/s from Stoke-Einstein equation. The slower diffusion on the surface conflicts common intuition

supported by hydrodynamic theories; viscous drags on a partially wetted particles are smaller than that observed in the bulk fluid. The surface contaminants could increase the effective viscosity. Nobili and co-workers also observed slower diffusions at air-water interface, suggesting thermally activated fluctuations of the interface at the particle-air-water contact line and their coupling to the particle drag through the fluctuation–dissipation theorem.[123]

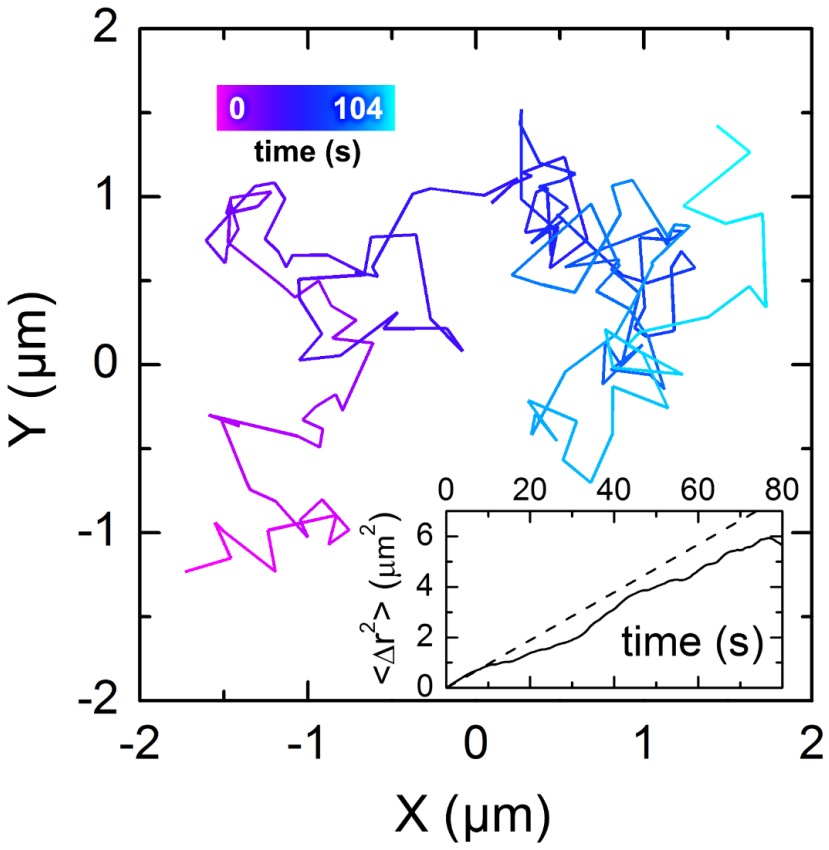

Figure 3.16 Trajectories over 104 s for an isolated GSNP on an IL droplet. Inset: time dependence of mean square displacement as measured by SEM (solid), calculated from Stokes-Einstein equation.

3.4 Conclusions

As an alternate approach to visualize the dynamics of soft matter systems, the combination of IL solvation with SEM imaging has applications beyond the model nanoparticle dispersions described here. Two applications under active exploration are nucleation and growth of polymer crystals and network formation in polymer gels. The chief limitations of the approach are (i) contrast is difficult to achieve without beam damage, and (ii) dynamics are observed near an interface. These are general concerns for *in situ* electron microscopy, and so the greater issue is how these concerns intersect with soft matter dynamics. Clearly, as demonstrated by the systems described here, dynamics near surfaces or in thin films, can be different than in bulk. But often, the differences are either small or relate to a nanoscale effect. Conversely, advantages of this approach are significant: (i) imaging is performed in a standard SEM without a liquid cell, (ii) sample preparation is simple, (iii) field of view is much larger than for TEM, and (iv) dynamics much below the optical diffraction limit are unequivocally resolved. Also, although undocumented here, a wide selection of materials (metals, semi-conductors, and organic materials) can be studied in ILs with acceptable contrast. The use of an IL for solvation may appear to be a constraint, but ILs, as a group, present a full spectrum of solvent properties, and experience shows the approach can be applied across the group, realizing just about any form of soft matter dynamics possible in thin films.

CHAPTER 4

CAPILLARY INTERACTIONS BETWEEN MICROSPHERES ADSORBED AT A CYLINDRICALLY CURVED LIQUID INTERFACE

4.1 Introduction

When particles adsorb to the interface between immiscible fluids, the interface may locally deform, producing a meniscus that causes long-range capillary interactions among the particles or between the particles and the interface edges. These lateral interactions often propagate over length scales much greater than the particle size, producing directed particle migration, the so-called Cheerios effect,[35] which has much appeal for assembly of hierarchical 2D structures by an inexpensive bottoms-up process.[36-45] For homogeneous isotropic particles, such as uniform spheres and disks, capillary interactions on a planar interface (i.e., one that is flat in the absence of the particles) have no directionality, but directionality may emerge on a curved interface due to anisotropy of the contact line around an adsorbed particle's periphery. To understand the capillary interactions on such curved interfaces, as well as their impacts on interfacial assembly, this study examined spherical microparticles adsorbed to highly stable cylindrical liquid interfaces, testing proposed theoretical expressions for particle wetting and particle-particle interactions through systematic variation of interaction parameters and optical microscopy tracking of particles.

Under capillary interactions, particles at an interface can attract or repel each other,[52, 56, 59, 124, 125] reflecting a more general principle that particles are driven up gradients of Gaussian interfacial curvature.[57, 58, 126, 127] On a planar interface, interfacial curvature near

an isotropic particle requires that the particle impose on the interface a vertical force, as might occur, for example, when particle and fluid densities are mismatched[46, 47] or when particle and interface are charged.[48, 49] Even so, capillary interactions are negligible in the first situation if the particle is small, or in the second if the electrostatic interactions are weak. Without interface deformation, a spherical particle simply inserts into the fluid so as to satisfy the equilibrium contact angle condition about its periphery. Beyond direct actions, vertical forces can also arise from nonuniform particle wetting. If the particle shape isn't isotropic, for example, the fluid-solid-vapor contact line must distort to satisfy the equilibrium contact angle conditions; the resulting shape-driven wetting behaviors have been demonstrated both theoretically and experimentally. An ellipsoidal (or rod-like) particle, for example, induces an interface curvature field of elongated, quadrupolar structure, thereby driving a collection of the particles to assemble variously into chains, loops, arrows, and orthogonal lattices.[50-52, 54, 56-59, 128-130] Likewise, interactions on curved interfaces cause these particles to orient and steer along predicted trajectories.[57, 58] Even slightly non-spherical (1% deviation for unity aspect ratio) particles display undulated contact lines and can undergo dendritic aggregation.[59]

For a spherical particle on an interface with anisotropic curvature, analogous orienting and directing phenomena occur because, to keep the contact angle constant about the particle periphery, the liquid meniscus must adopt a non-uniform curvature field. Interface curvature anisotropy is captured in the deviatoric curvature D, defined as $1/2|\kappa_1-\kappa_2|$, where κ_1 and κ_2 are the principal radii of curvature. In an early contribution, Wüger predicted that a sphere on a catenoid surface creates a quadrupolar interface deformation,[60, 61] and as a consequence, spheres on such a surface migrate toward the

catenoid waist, where they order into a square lattice. Russell and co-workers experimentally observed that spherical particles on a capillary bridge are driven toward the bridge edge.[62] More generally, Nobili and co-workers predicted and measured the capillary force experienced by a sphere placed on an interface of arbitrary shape.[63] Sphere ordering into a square lattice was also observed by van der Gucht and co-workers, who measured a larger capillary interaction energy[64] on interfaces of higher *D*.

Dinsmore and co-workers estimated the adsorption energy of a sphere on a cylindrical interface (a surface of uniform *D*) by numerical calculation.[65] Because of the zero gradient in curvature for such a surface, capillary forces are not experienced unless a second sphere is encountered. Near an isolated sphere of radius *a* and equilibrium contact angle θ_e, deviation ζ of the interface from its unperturbed cylindrical shape was predicted to display a quadrupolar form

$$\zeta = \frac{a^4 D}{6s^2}\sin^4\theta_e \cos 2\phi + O\left(D^3 a^4\right) \qquad \text{Equation (1)}$$

where *s* and φ are distance and direction from the sphere center (the latter defined as angle with respect to cylinder axis). The derivation of Equation (1) assumed that $Da \ll 1$, i.e., that the sphere radius is much less than the cylinder radius, making interface curvature on the particle size scale a perturbation. Under this condition, the magnitude of the first term can be written $\zeta / a \sim aD\left(a/s\right)^2$, and with s_c, the nominal s at the contact line, following the proportionality $s_c \sim a$, the maximum interface deviation, obtained at the contact line, is approximated $\zeta_{\max} \sim a^2 D$. Establishing an analogy to the 2D electrostatic interaction of charge quadrupoles, Dinsmore and co-workers further

calculated the capillary force F between identical spheres on a cylindrical liquid interface,

$$F(d,\omega) = \frac{4\mathrm{D}^2\pi\gamma a^8 \sin^8\theta_c}{3d^5}(\hat{z}\cos 5\omega + \hat{y}\sin 5\omega) + O\left(\frac{\mathrm{D}^4\gamma a^{10}}{d^5}\right) \qquad \text{Equation (2)}$$

where d is the sphere separation distance, ω is the angle defined by the line of sphere centers and the direction of the cylindrical axis, and γ is the interfacial tension. Choosing a cylindrical coordinate system aligned with the cylinder, $\hat{z}$ and $\hat{y}$ are orthogonal unit vectors tangent to the interface and locally pointed in axial and angular directions. In the electrostatic quadrupole analogy, the charge assigned to a sphere here is $\sim a^2 D\left(a^3\right)$. Figure 4.1 illustrates the geometric variables as well as the anticipated perturbations to interface shape for isolated and paired sphere(s).

The key objective of this work was to test Equation 1 and 2, which were derived under the assumption that the adopted, possibly non-equilibrium contact angle θ_c matches θ_e uniformly around the wetted sphere periphery. The interface perturbations near an isolated sphere were measured using a three-dimensional (3D) optical profilometer, and the capillary interaction between a pair of particles was estimated from the particle trajectories determined using an optical microscope. In both cases, to preclude evaporation, ionic liquids and low molecular weight polymer were employed; these liquids are essentially nonvolatile, thereby stabilizing interface shape and eliminating evaporative temperature gradients that might cause unwanted convection.

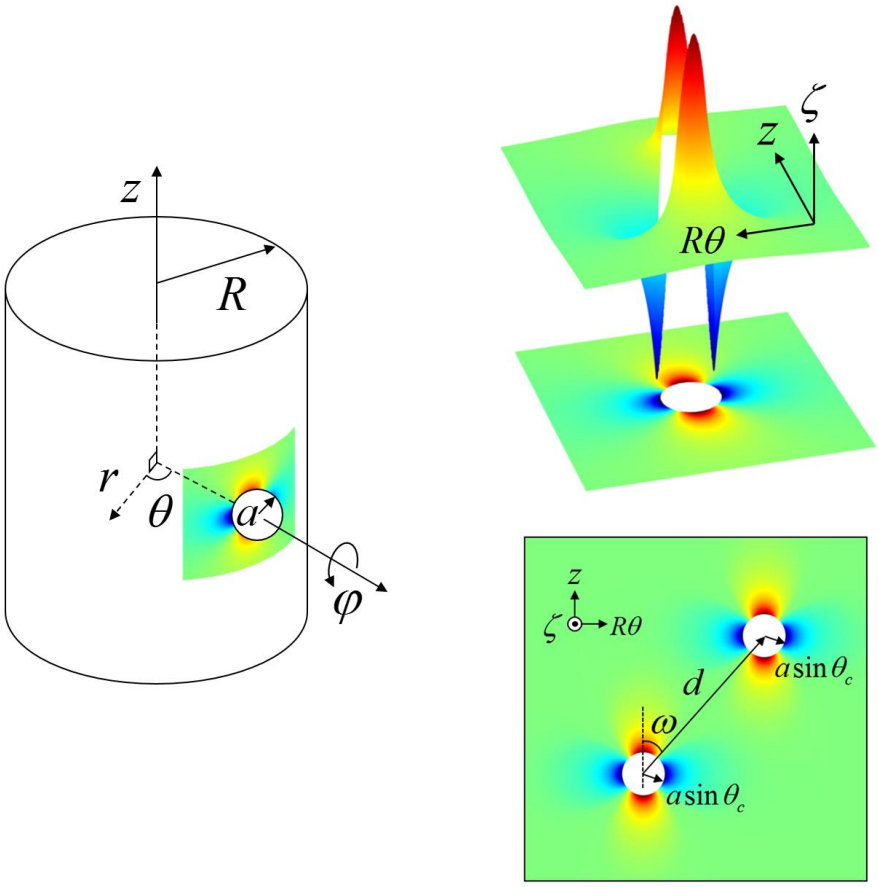

Figure 4.1 Geometry of the experiments. (Left) Sphere bound to a cylindrically curved liquid interface. (Top right) Meniscus near the particle from the theoretical prediction. The deformation of the interface was enhanced for clarity (Bottom right) Capillary interaction between two spheres bound to the interface.

4.2 Experimental

4.2.1 Materials and Sample Preparation

A freestanding cylinder is a problematic liquid geometry because surface tension quickly breaks such a cylinder into spherical drops. Here instead, liquid shapes were prepared on a flat silicon substrate by spreading a liquid over chemically patterned lines made by photolithography and chemical vapor deposition. A perfluorinated background of vastly different surface energy surrounded the silicon oxide lines (160-μm width, 14-

mm length). Thus, a polar spread liquid wetted the high-surface-energy lines but not the low-surface-energy background, creating surface-pinned horizontal cylindrical segments. A horizontal cylindrical segment is a shape produced by cutting a cylinder parallel to its axis. The chord length created by this hypothetical cutting corresponds to the patterned line width, which departs from the liquid shape's perpendicular radius of curvature except when the liquid volume corresponds to a half cylinder. To simplify analysis, liquid volumes were kept smaller, making the perpendicular radius of curvature larger than the line width, and likewise, spheres for analysis were selected from near the centerline, where the liquid thickness was greatest and the liquid surface was nearly parallel to the substrate surface.

To preclude evaporation, the cylindrical segments were made either of the ionic liquid bis(hydroxyethyl)dimethyl ammonium methanesulfonate $[C_6H_{16}O_2N][CH_3SO_3]$ (abbreviated BH-DAMS) or low molecular weight polymer polyethylene glycol (400 g/mol; abbreviated PEG400), with both displaying negligible volatility. BH-DAMS was selected when measuring the meniscus shape near a single sphere by optical profilometry, studies conducted in open air (i.e. at a gas-liquid interface), and PEG400 was chosen when assessing capillary interactions by particle tracking optical microscopy, studies conducted with the cylindrical segment covered by an immiscible and nonvolatile silicone oil (i.e., at a liquid-liquid interface). The different liquid choices reflect the different needs of the two experiments. A gas-liquid interface produces the best interference fringe contrast (light reflectivity at normal incidence here was 3.8%), and the chosen liquid-liquid pairing offers slow sedimentation to the interface of spheres suspended in the covering liquid. Figure 4.2 provides a sketch of the nominal liquid

interface geometry, a table of tested material combinations, and an optical micrograph of BH-DAMS cylindrical segments in air.

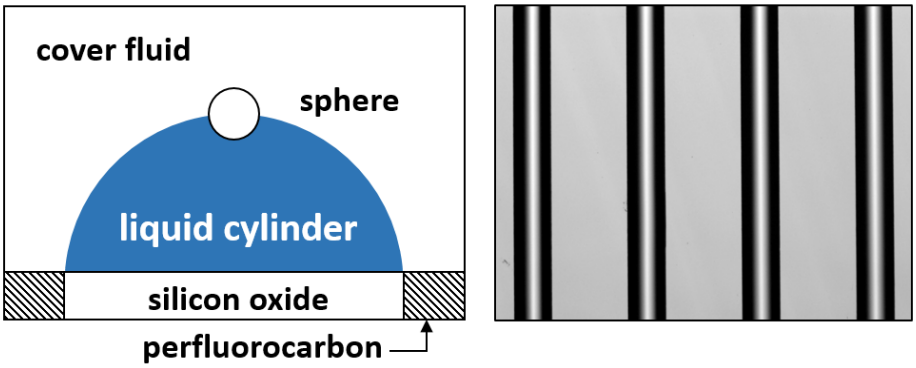

Study	Cover fluid	Cylinder	Sphere
Meniscus Shape	air	bis(hydroxyethyl) dimethyl ammonium methanesulfonate	polystyrene
Capillary Interaction	silicon oil 20 cP	polyethylene glycol MW400	polystyrene

Figure 4.2 Schematics of the experiments. (Top left) Configuration of the system. (Top right) Liquid pinned on a chemically patterned substrate to create cylindrically curved sinterfaces. Image width is 1.7 mm. (Bottom) Materials for each component.

4.2.1.1 IL purification and storage

Bis(hydroxyethyl)dimethylammonium methanesulfonate ($[C_6H_{16}O_2N]$ $[CH_3SO_3]$, BH-DAMS) was received as a gift (TEGO IL 2 MS; Evonik Goldschmidt GmbH, Essen, Germany). The clear but amber-colored liquid was stirred 48 h with activated charcoal (Norit CA1, Sigma-Aldrich) and methanol before the filtration through a column packed with diatomaceous earth (Celite 545, Sigma-Aldrich) and a PTFE 0.2-μm membrane (Whatman). After removing methanol in reduced pressure, the IL was dried in vacuum

oven at 60 °C for a week before storage in a nitrogen glove bag.

4.2.1.2 Preparation of Chemically Patterned Substrates

Chemical line patterns for liquid semi-cylinders were prepared by photolithography as described by Cheng et al. A photomask was custom-made from PhotoplotStore. The mask has lines in 10,160 DPI resolution on a polyester film. Each line had 160-μm width and 14-mm length with 320-μm spacing. Silicon wafers (100-mm diameter, 550-μm thickness, 2500-Å wet thermal oxide layer) were obtained from International Wafer Service. The wafers were cleaned by oxygen plasma using a RF plasma chamber (Harrick Plasma Cleaner, PDC-001). The chamber was depressurized to 50 mTorr and then bled with oxygen until the pressure becomes steady at 120 mTorr. The plasma was generated at 30 W and etched the wafers for 20 min. In a cleanroom environment, line patterns were fabricated on the cleaned wafers. Microposit S1813 positive photoresist was spun-coated on the wafer at 3000 rpm and soft-baked at 115 ˚C for 60 s. The wafer and the mask were tightly contacted by vacuum using Karl SUSS MA6 mask aligner and then exposed to UV (400-nm wavelength, 150 mJ/cm^2). The exposed wafer was stirred gently in a developer solution (Microposit MF-321 in deionized water, 1:4 in volume) for 45 s and then rinsed in water for 60 s. The fabricated substrates had S1813 lines surrounded by a silicon oxide layer. The substrates are again cleaned with oxygen plasma in the same procedure; oxide was cleaned preferentially, since S1813 was stable from plasma etching. The oxide layer was perfluorinated afterward by chemical vapor deposition methods. The substrates were placed in a polypropylene container (12-cm diameter × 8-cm height) together with a vial containing 0.1 ml of (tridecafluoro-1,1,2,2-tetrahydrooctyl) dimethylchlorosilane (Gelest, $CF_3(CF_2)_5CH_2CH_2Si(CH_3)_2Cl$,), which was used without

purification. The container was sealed and heated in an oven at 70 ˚C for a week. The chemically patterned substrates were cut into pieces and stored in a sealed container. Just prior to preparing liquid cylinders, the substrate was rinsed with solvents in the order of hexane, acetone, and isopropyl alcohol and blown dry with a nitrogen stream; hexane washed out non-anchored perfluorocarbon and acetone removed S1813 to uncover silicon oxide layer.

4.2.1.3 Preparation of Cylindrically Curved Interfaces

A drop of liquid (BH-DAMS or PEG400) was rolled on the chemically patterned substrate and any excess liquid was removed by blotting with task wipers. To prepare interfaces with higher curvatures, the same liquid was sprayed on the substrate using an airbrush (Iwata Eclipse HP-CS) pressurized by dry nitrogen gas (30 PSI). The high viscosity of BH-DAMS was lowered by diluting with methanol (50 v/v%) for spraying. The methanol was then removed in a vacuum oven for three days at 60˚C. In case of PEG400 was covered by silicon oil after attaching the substrate on a polystyrene dish (1.5-inch diameter, 6-mm height) using a UV curable adhesive (Norland Optical Adhesive 71).

4.2.1.4 Preparation of Particles

Polystyrene microparticles of 5±0.09, 10±0.11, and 20±0.31 μm diameter were purchased from Sigma-Aldrich, and fitting scanning electron microscopy particle images to ellipses, their average elliptical eccentricity ε ($=\sqrt{1 - b^2 / a^2}$), where a and b are the respective semi-major and semi-minor axes lengths), was found to be less than 0.1 (Figure 4.3). Prepared using a persulfate polymerization initiator, the particles

incorporated sulfate groups on their surfaces, and due to these ionizable groups, even without added surfactant, repulsive electrostatic interactions stabilized aqueous dispersions against aggregation. The 10- and 20-μm particles were 2% cross-linked to fix shape, and as supplied, all three samples had nominally clean particle surfaces, although surface roughness was not assessed experimentally. To remove stray contaminant(s), particles were centrifuged and washed multiple times with copious deionized water before dispersal in methanol or silicon oil for meniscus shape and capillary interaction studies, respectively.

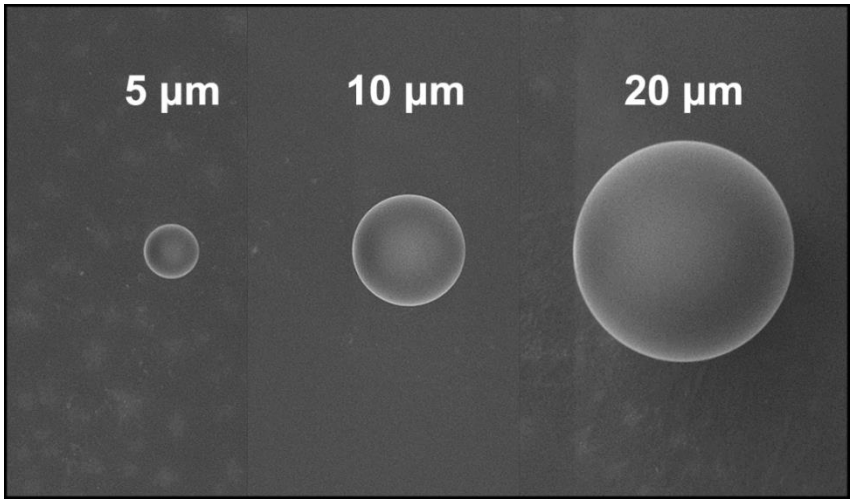

Figure 4.3 Scanning electron micrographs of 5-μm, 10-μm, and 20-μm polystyrene spheres on a flat carbon film. The average eccentricity of the particles is less than 0.1.

4.2.2 Contact Angle Measurement

Advancing and receding contact angles, θ_A and θ_R, respectively, between microparticles and liquids were estimated by the sessile drop method, which was implemented over a smooth, flat surface prepared by spin coating the uncrosslinked 5-μm microparticles onto a silicon wafer. The particles were dissolved in toluene and filtered through 0.2-μm PTFE

membrane before spun-coated on an 8-mm square wafer. Then the polymer films were fully dried in a vacuum oven at 90 ˚C overnight. Figure 4.4 shows the lateral views of two interfaces. For air-BH-DAMS, θ_A/θ_R=83°/42°, and PEG400-silicone oil interface, θ_A/θ_R= 97°/54°. Hysteresis was substantial in both cases, implying a large difference in activation energies for advancing and receding contact lines; θ_e lies between θ_A and θ_R. As particles were brought to the curved interface from above (see below), θ_A would appear the more pertinent characterization, and values for this angle establish that a majority of the microparticle surface was wetted by BH-DAMS, or alternately, PEG400. Considering the smoothness of the test surface, the pronounced contact angle hysteresis presumably originated in surface chemical inhomogeneity, either produced during particle preparation or adsorbed from advancing liquid during deposition.

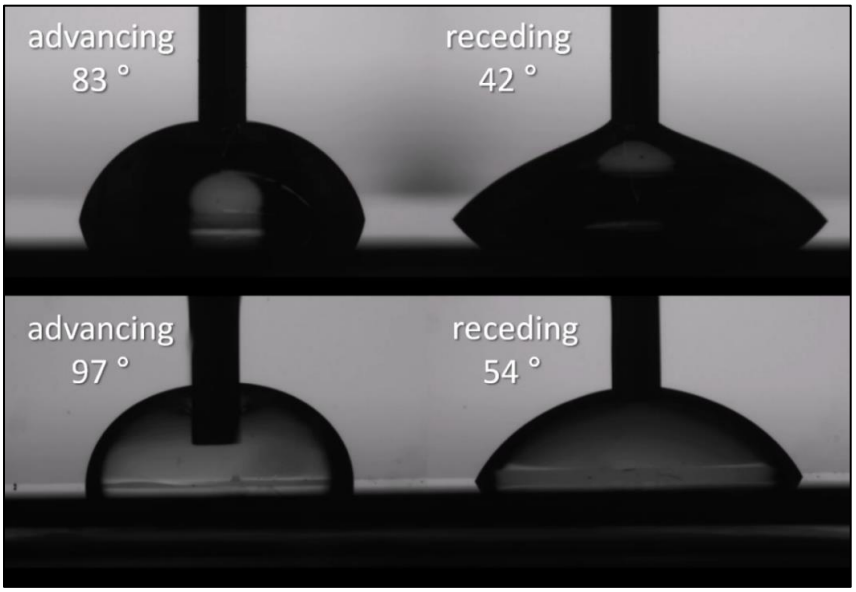

Figure 4.4 Advancing and receding contact angles between polystyrene surface and liquid interfaces. (Top) air/polystyrene/BH-DAMS, θ_A / θ_R =83°/42°. (Bottom) silicon oil /polystyrene/PEG, θ_A/θ_R=97°/54°.

4.2.3 Meniscus Shape Profiling

To measure meniscus shape near an isolated particle, particles dispersed in methanol at very low concentration were sprayed onto curved air-BH-DAMS interfaces using an airbrush pressurized by dry nitrogen gas (30 psi). The resulting depositions were approximately random across the array of curved interfaces decorating a Si substrate, with the adjacent particles on a single interface typically separated by ~500 μm, making overlap of menisci from different particles rare events. Spraying was performed at large displacement between nozzle and substrate (>60 cm), and consequently, most of the methanol evaporated in transit to the interface. To remove the remaining portion, samples were dried at 30˚C under vacuum for a week prior to optical profilometry. For the latter, liquid interfaces were aligned on the motorized microscope stage and scanned using a 50× objective lens combined with a 2.0× field zoom lens. Images were then collected at 640x480 pixel horizontal pixel resolution and sub 1-nm height resolution.

4.2.4 Particle Motion Tracking

To monitor capillary interactions, dilutely dispersed particles in silicon oil were carefully layered over a pre-deposited set of curved PEG400 liquid interfaces. The microparticles (1.05 g/cm^3) sedimented slowly in the covering oil (0.93 g/cm^3, 150-μm thickness) before their capture at the liquid-liquid interface. The interface captured microparticles were imaged with an optical microscope (Olympus BX60) installed on a vibration isolation table. That the particles resided in the same focal plane as the liquid interface proved the attachment of particles to interface. The bulk of the bound particles displayed lateral mobility, with the remaining few immobilized near the liquid-liquid-

substrate contact line, where interface particle penetration was sufficient to stick the particles to the underlying substrate. After 30 min equilibration in the microscope, pairwise motions of neighboring particles (d<6a) were recorded for pairs well away from the liquid-liquid-substrate contact line.

4.3 Results and Discussion

4.3.1 Cylindrical Interface without Spheres

Cylindrical segment shape was verified by 3D optical profilometry (Zygo Newview 7300). Excluding the two tip regions, the liquid interface height was uniform in the line direction, and the cross-section was well fit by a circular arc (normalized by R, the root-mean-squared deviation from a fitted circular arc was ~0.1%), as shown in Figure 4.5. The good fitting affirmed the dominance of capillarity relative to gravity at 160-μm line width, a dimension at least an order of magnitude smaller than the mm-scale capillary length $\lambda_c = \sqrt{\gamma/\rho g}$, where ρ is the liquid density and g is the gravitational constant. With gravity's influence negligible to liquid shape, the mean interface curvature was invariant, with zero curvature in the axial direction and constant positive curvature in the perpendicular direction.

To vary the perpendicular curvature, variable liquid volumes were sprayed onto the lines using an airbrush, obtaining D~0.006 μm^{-1} at maximum loading. Depending on the interface penetration by spheres, which sets a lower bound to this loading, the minimum D ranged from ~0.0001 μm^{-1} to ~0.002 μm^{-1}. The horizontal cylindrical liquid segments preserved their initial shapes for at least several months.

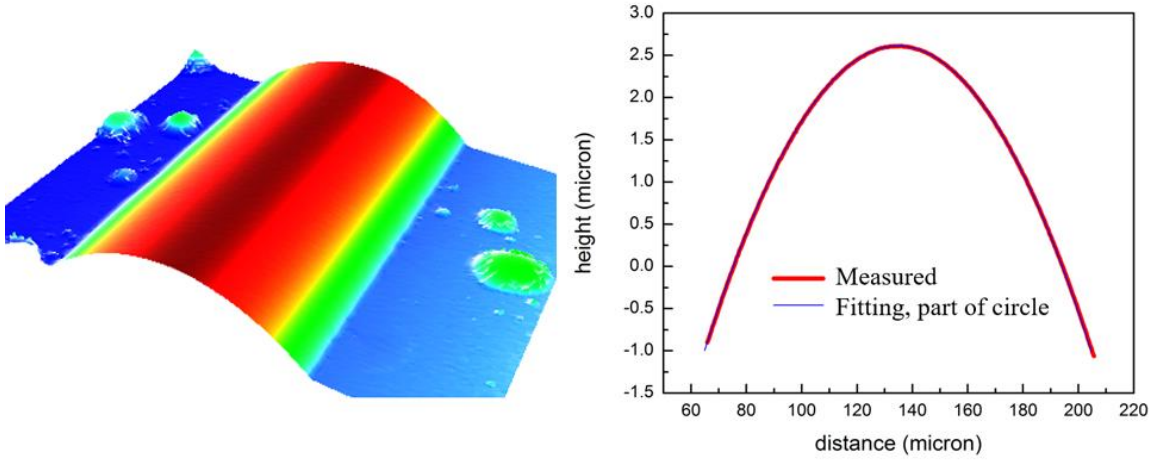

Figure 4.5 Cylindrical shape of air-DAMS interface measured by an optical profilometer. (Left) 3D plot of a liquid pinned on the line patterned substrate. (Right) Fitting of cross-section of the interface along the direction of the minimum curvature to a circular arc.

4.3.2 Spheres on Planar Interface

The selected microparticles were too small to impose a gravity force sufficient to create a meniscus around the particles on a flat liquid interface, with the governing Bond number, $Bo=\Delta\rho g a^2/\gamma$, of order 10^{-6}, where $\Delta\rho$ is the density difference between particle and liquid. Confirming this expectation, Figure 4.6 shows the surface topography in the vicinity of an isolated 20-μm microsphere adsorbed to an intrinsically planar air-BH-DAMS interface. Despite finite (and positive) $\Delta\rho$, upward interface deformation due to particle buoyancy was not apparent; instead, on a gross scale, the interface remained nearly flat. Cross-sections better highlight nuances of surface topography, and Figure 4.6 demonstrates that the contact line about the particle periphery undulated with a small vertical amplitude of ~10 nm. This undulation, barely above superimposed noise/fluctuation/drift, crudely followed a quadrapolar ϕ dependence, and as seen in the same figure, a weak meniscus of the same approximate form propagated over the nearby

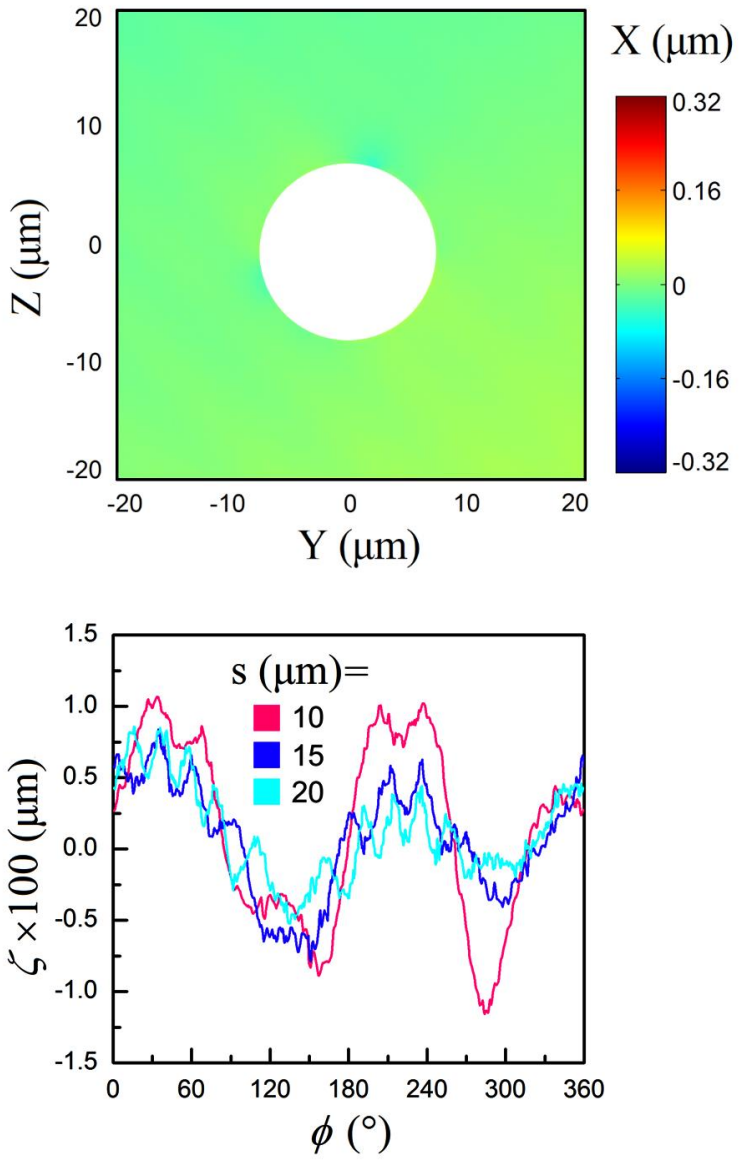

Figure 4.6 Meniscus of a flat air/BH-DMAS interface near an adsorbed 20-μm polystyrene sphere (Top) Height map of the interface. (Bottom) Height profile of the interface along *s*=10, 15, and 20 μm.

liquid interface. Numerical calculations for a particle with 0.1 eccentricity predict a maximum ζ variation of ~10^{-3} nm,[59] four orders of magnitude less than observed. Hence, as an alternative explanation, the anisotropic meniscus over a flat interface is argued to arise from contact line pinning on particle surface defects, a proposal consistent with the

substantial measured contact angle hysteresis for the test surface. In subsequent discussion of behaviors observed on curved liquid interfaces, the potential contribution of this particle-imposed interface deformation will be ignored; for the 20-μm spheres, the undulations measured for a planar interface were ~30 times smaller than those observed for a curved interface.

Further, the anisotropic meniscus on a planar interface rotated freely and was observed at all orientations in the plane, distinct from the behaviors seen on an intrinsically curved interface, where an anisotropic meniscus stayed fixed in orientation and directed as expected with respect to interface curvature. On an intrinsically flat interface, two particles in apparent contact never bonded irreversibly, an absence indicating that any residual capillary interaction was weak compared to thermal fluctuations and/or electrostatic repulsions. This behavior again departed from that observed for the same particles on a cylindrical liquid segment, where particle-particle bonding was irreversible.

4.3.3 Spheres on Cylindrical Interface

4.3.3.1 Shape of Interface near a Sphere

Figure 4.7 shows a quadrupolar meniscus generated by the wetting of a 20-μm sphere on a cylindrically curved liquid interface with D=0.004 μm^{-1}; relative to the particle-free surface, the surrounding interface rose in axial (or z) directions and fell in perpendicular (or y) directions. The occluded central region, bounded by the sphere's wetted perimeter, was significantly smaller than the sphere cross section due to the deep penetration of the sphere into the liquid. (The sphere center-unperturbed interface displacement was less than a.) Notably, the occluded domain, defined by $s=s_c$, where s_c varies with ϕ was

distorted from circular. By $s \sim 5a$ (beyond the range displayed), the meniscus had smoothly faded into the cylindrical background, characterized by straight, vertical contour lines. Indeed, the meniscus topological cross-sections in Figure 4.7 reveal that most of the meniscus amplitude faded over $s<2.5a$, with the decays in the axial and perpendicular directions similar; meniscus shapes on opposite sides of the particle were nearly mirror reflections. All these features are qualitatively consistent with the theoretical expressions given in the Introduction. To confirm that the sphere caused the deviations in interface shape, Figure 4.7 also provides orthogonal topographic sections at $s=10a$; at this large distance from the sphere, the interface curvature was cylindrical.

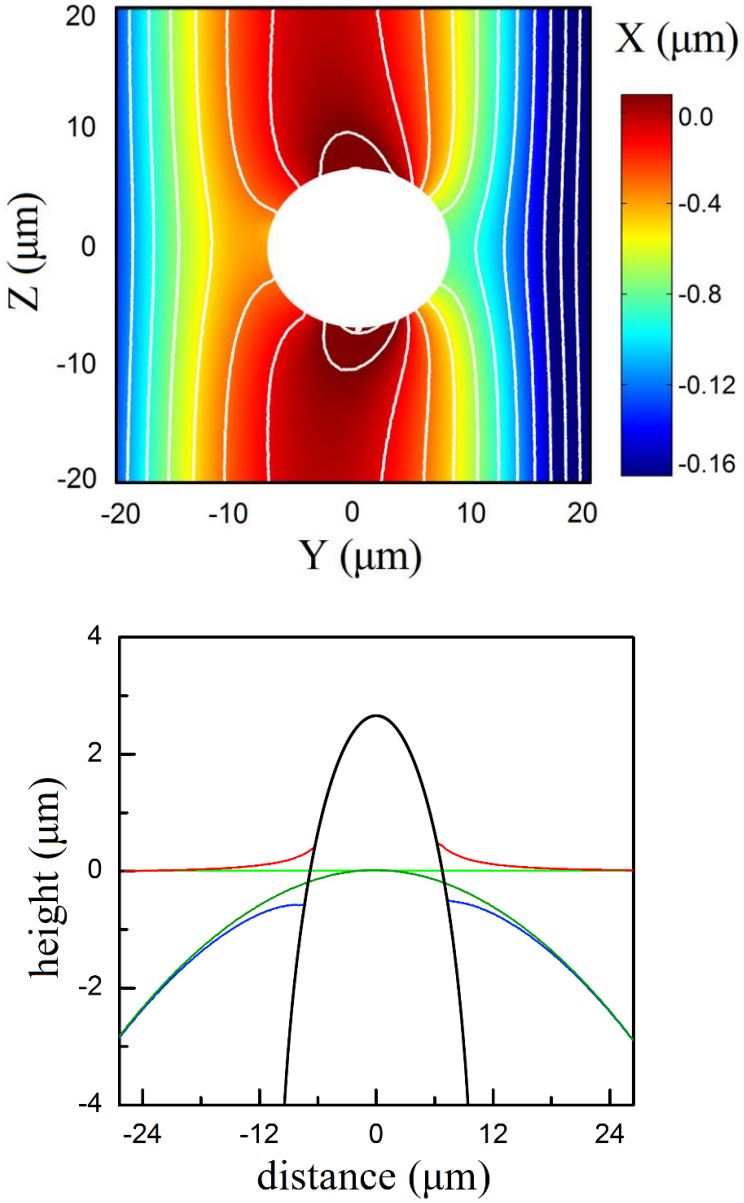

Figure 4.7 A cylindrically curved air/BH-DMAS interface (D=0.004 μm^{-1}) near an adsorbed 20-μm polystyrene sphere. (Top) Height map. (Bottom) Height profiles across the particle center (red, blue) and across a remote location (lime, green).

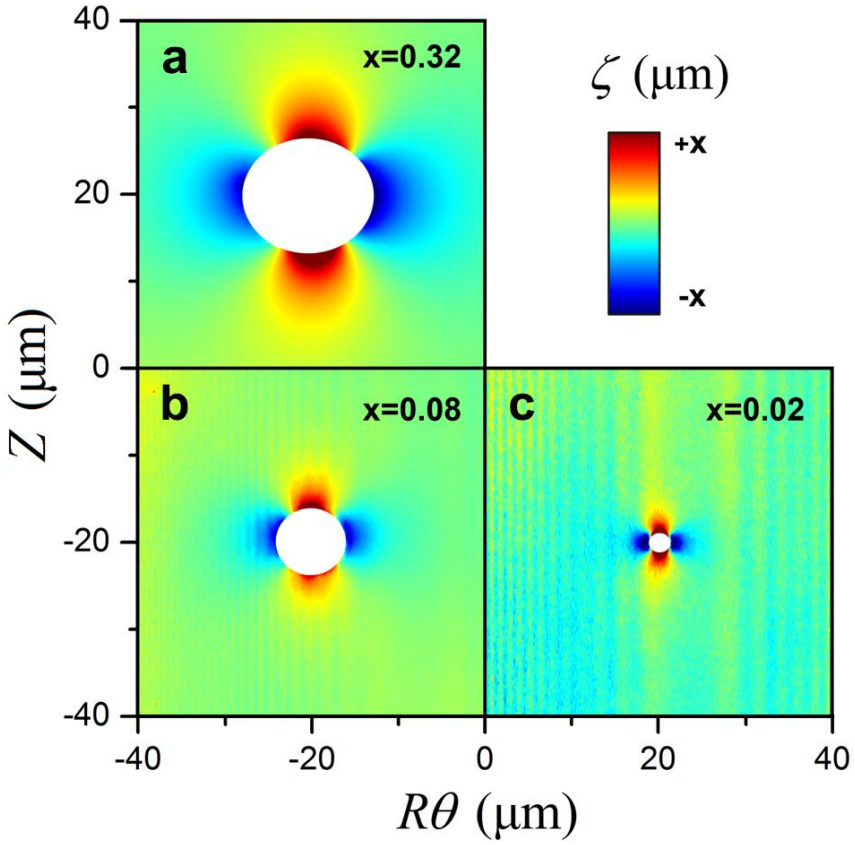

Figure 4.8 Deformation map of a cylindrically curved air/BH-DMAS interface perturbed by 20-μm (a), 10-μm (b), and 5-μm (c) polystyrene spheres.

To obtain meniscus structure by profilometry, the Cartesian coordinate x of the liquid interface was measured across a grid of y,z locations. Then, to line up the measured topography with the theoretical predictions, the interface from profilometry was mathematically "unwrapped", thereby presenting the interface deviation ζ from cylindrical shape in terms of surface coordinates. Defined as r-R, ζ can alternately be plotted in terms of the global surface coordinates $R\theta$,z, where $R\theta$ is the perpendicular arc length assessed relative to the cylindrical centerline, or the local surface coordinates s, ϕ, defined relative to the particle center. Figure 4.8a presents the unwrapped form of the quadrupolar meniscus displayed in Figure 4.7, and Figures 4.8b-c show analogous unwrapped quadrupolar menisci for 5- and 10-μm particles, all at D=0.004 cm^{-1}. The

nominal s_c for the 20-μm particle was ~4 and ~2 times greater, respectively, than for the 5- and 10-μm particles, and further, ζ_{max} was~16 and ~4 times larger. These values agree quantitatively with the expressions presented in the Introduction, and the measured menisci structures do not change in time. The magnitude of ζ_{max} was tens to hundreds of nanometers, orders of magnitude less than a (and more than an order of magnitude larger than the contact line ζ fluctuations observed on a planar interface at the same a). Figure 4.8 also reveals that the lateral meniscus span increased with a.

Figures 4.9a-c present several detailed aspects of meniscus topography for 20-μm spheres on a D=0.004 μm cylinder. Superimposing local coordinates for clarity, Figure 4.9 highlights topographic symmetries, including ϕ=0º and 90º lines of almost perfect symmetry. The s dependence of ζ for 0º≤ϕ≤90º is plotted in Figure 4.9a, with curves of constant ϕ starting at different s_c due to the previously discussed distortion of the wetted perimeter. The figure indicates that for all ϕ, $|\zeta|$ fell below the profilometer's resolution limit, ~0.01 μm, by s≈2.5a (≈25 μm) and displayed just a weak or nil dependence of decay length on ϕ, both as predicted by Equation 1. Supporting the quadrupole depiction of meniscus structure, the same figure shows that, for fixed s, the magnitudes of $|\zeta|$ at ϕ=0º and 90º are approximately equal. For example, at the lowest shared s value, ~6.5 μm, $|\zeta|$ was respectively 0.275 and 0.29 μm at the two angles. Equation 1 also predicts that ζ falls as s^{-2}, matching another quadrupole characteristic, and Figure 4.9b replots the curves of Figure 4.9a as log$|\zeta|$ versus log$s$ to confirm this -2 exponent. Within experimental error, which changes with ϕ due to the shifting magnitudes of $|\zeta|$, the predicted exponent is fully consistent with experiment. Figure 4.9c tests still another quadrupole characteristic, angular dependence of the field in the form ζ~cos2ϕ, and

theoretical expectation is met; this form holds to positions well away from the particle. To emphasize the result, at s=10 μm, the measured deviation is plotted alongside its predicted angular form (fitted in amplitude), and the discrepancy between experiment and theory is insignificant.

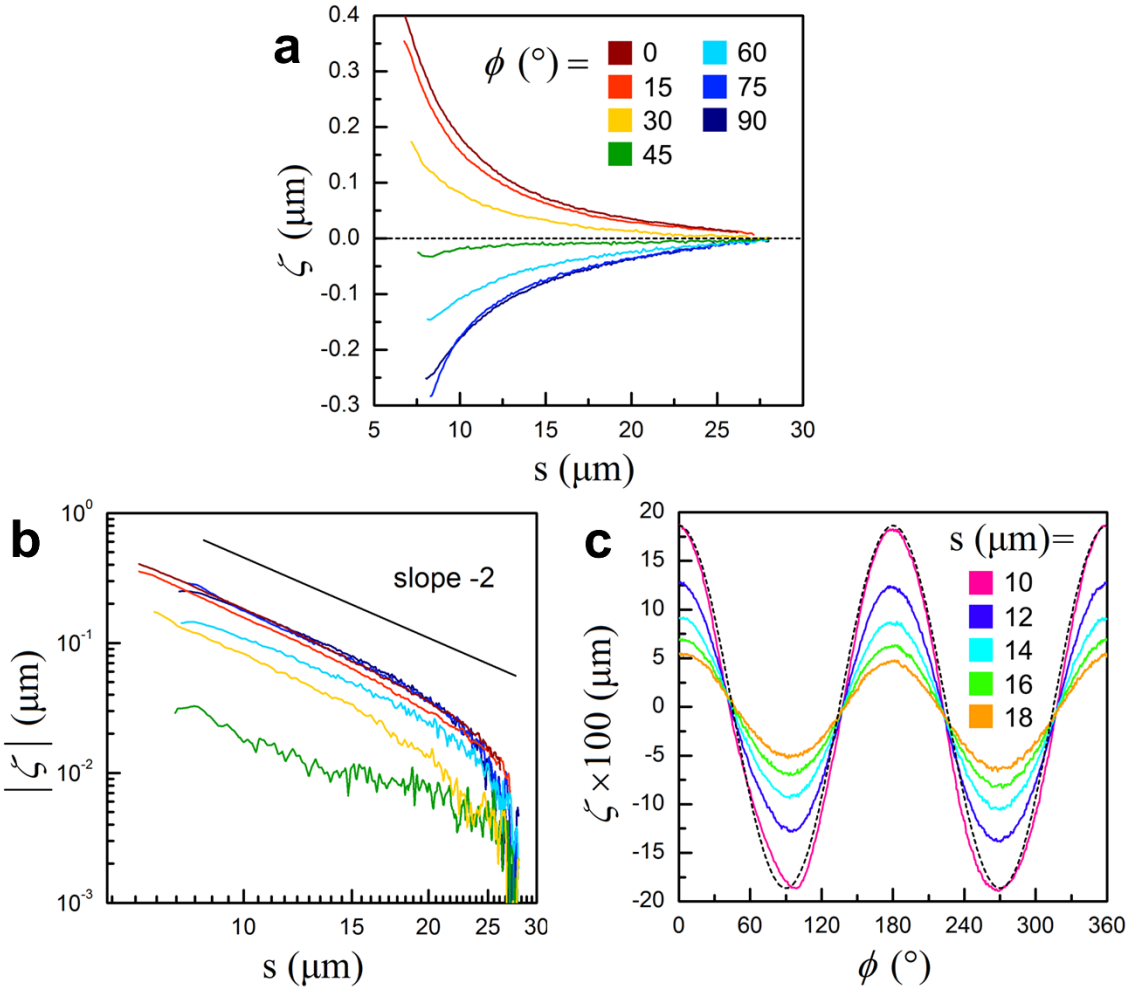

Figure 4.9 Deformation, contact line, and contact angle around a 20-μm polystyrene sphere on a cylindrically curved air/BH-DMAS interface (D=0.004 μm^{-1}). (a) Deformation line profiles in s direction for ϕ =0, 15, 30, 45, 60, 75, and 90˚. (b) Log-log plot of Figure 4.9a. (c) Deformation line profiles in φ direction for ρ=10, 12, 14, 16, and 18 μm with cos2ϕ (dotted) scaled to the curve s=10 μm.

4.3.3.2 Contact Line between Particle and Interface

To assess how the formation of a meniscus affects the contact line perimeter, which is defined by the ϕ dependence of s_c, an "unperturbed" or reference perimeter was theoretically constructed by intersecting a sphere and a cylinder of appropriate radii with their relative positions overlapped as found in the actual experiment. The cylinder's anisotropic curvature makes the unperturbed perimeter non-circular, and after cylinder unwrapping, the cylindrical curvature stretches the contact line outward in the perpendicular direction. In experiment, because the sphere center lay below the cylinder surface, the upward meniscus deviation along the cylinder axis pushed the contact line inward, and the downward deviation in the perpendicular direction pushed it outward.

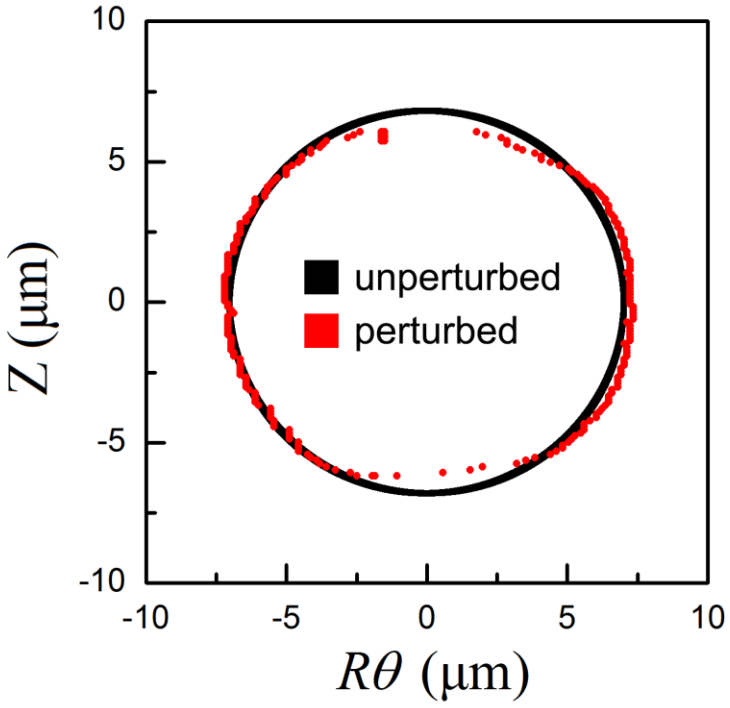

Figure 4.10 Contact line around a 20-μm polystyrene sphere on a cylindrically curved air/BH-DMAS interface (D=0.004 μm^{-1}) before (black) and after (red) the perturbation by the particle.

Unperturbed and perturbed (i.e., experimental) perimeters are compared in Figure 4.10 for a 20-μm sphere on a D=0.004 μm cylinder; the sphere center was 8 μm below the cylinder surface due to favorable wetting. The perturbed perimeter was more elongated in the perpendicular direction than the unperturbed perimeter as the ratio of major (perpendicular) to minor (parallel) axis rose from 1.03 to 1.17. The largest displacement (inward) was in the axial direction. A theoretical formula for s_c did not emerge from the analysis leading to Equations. 1 and 2, so Figure 4.10 doesn't present a prediction for the perturbed perimeter.

4.3.3.3 Contact Angle between Particle and Interface

When a surface is topologically and chemically homogeneous, θ_c is expected to satisfy Young's equation and approach its equilibrium value θ_e. For a homogeneous sphere on a liquid interface, irrespective of the interface's intrinsic curvature, this expectation points to adoption of θ_e everywhere on the sphere's wetted periphery. Indeed, the theoretical expressions of the Introduction were derived on this condition. Nevertheless, the θ_A/θ_R hysteresis found for the flat model surface of the pendant drop measurements introduced concern about distortions of the wetted perimeter generated by irregularities in θ_c. Further, because of its mode of manufacture, this flat surface might have presented different wetting characteristics than the curved sphere surfaces. Given sphere deposition by solvent evaporation, θ_c was anticipated to approach θ_A measured by the pendant drop method; instead, as revealed in Figure 4.11, θ_c fluctuated about a value more comparable to θ_R. Non-equilibrium contact angle poses a central consideration for these experiments, but before attacking the topic further, it is emphasized that the preceding results for single

particle wetting were readily reproduced: the adoption (or not) of non-equilibrium θ_c did not seem to impact meaningfully the gross quadrupolar meniscus structure.

For the 20-μm spheres on BH-DMAS, Figure 4.11 plots the ϕ dependence of ζ_{max} alongside the ϕ dependences of θ_c measured and θ_c predicted absent a meniscus perturbation to cylindrical interface shape. Shown as a solid black curve, ζ_{max} follows the same cos2ϕ dependence seen in Figure 4.11 for ζ away from the sphere. Noise in ζ_{max} appears relatively small, contrary to expectation for a surface presumed to be heterogeneous. The value of θ_c without interface perturbation, shown as the dashed red curve, follows the same cos2ϕ dependence, this angle oscillating between 41.2˚ to 42.9˚, a narrow range close to θ_R. Measured θ_c, derived from the topography given in Figure 4.7 (i.e., before the distortion incurred by unwrapping) and drawn as the solid red curve, shows a different trend: while still undergoing a sinusoidal 2ϕ oscillation, albeit with appreciable noise/drift, oscillation is phase-shifted by ≈90º. The mean of θ_c is again ≈42º, but the oscillation amplitude is large, ~7º, well beyond the experimental uncertainty in this parameter. An inverse correlation between θ_c and ζ is thereby established, with θ_c reduced at large ζ and increased at small ζ. The directions of these trends naively indicate that outward (or positive) interface deviation make wetting resemble that of a receding contact line while inward (or negative) interface deviation make wetting resemble that of an advancing contact line. While these trends are obscure in origin, at least for the current system θ_c was certainly not constant around the wetted perimeter, violating an assumption made in the existing theory. Nevertheless, whether the violation can be considered significant remains unclear, given that many other experimental trends track

well with predictions of the same theory. It is probable that heterogeneities on the sphere surface systematically pin the contact line. Manoharan and co-workers demonstrated that surface defects logarithmically slow microparticle wetting, with equilibration possibly achieved only on the timescale of several months, much longer than allowed here.[131]

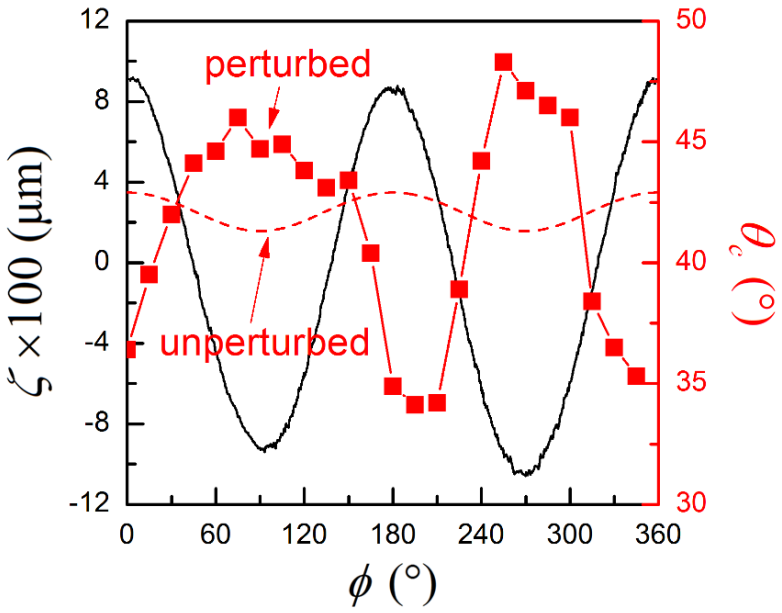

Figure 4.11 Contact angles around a 20-μm polystyrene sphere on a cylindrically curved air/BH-DMAS interface (D=0.004 μm^{-1}) before (dotted) and after (solid) the perturbation.

4.3.3.4 Effect of Particle Size and Interfacial Curvature

The preceding discussion conveyed results for a single combination of sphere and cylinder size (a=20 μm; R=500 μm, equivalent to D=0.004 μm^{-1}). Wetting and menisci structure were evaluated for further combinations, and Figure 4.12 summarizes the findings in terms of trends at a common interface location, the position at which z on the contact line reaches its largest value (ϕ=0°, s=s_c). For 0.002 μm^{-1}<D<0.002 μm^{-1} and a=5, 10 and 20 μm, Figure 4.12a shows θ_c scattered between 25° and 52° without a discernable

trend in D; parsing individual data points, the variations in θ_c between spheres are larger than those along the wetted perimeter for any single sphere. To clarify the influence of θ_c variations on wetting and meniscus properties, Figures 4.12b and 4.12c evaluate the sphere vertical displacement relative to the interface level; this displacement is highly sensitive to θ_c. While theoretical expressions for sphere displacement on a cylindrical liquid interface aren't available, expressions for a planar liquid interface are straightforward, and with the curvature here always small (i.e., aD<<1), the latter expressions should provide excellent approximations. In particular, for a non-buoyant sphere on a planar interface (i.e., one with no meniscus), $s_c=a\sin\theta_c$ and $r_c-R=a\cos\theta_c$, where r_c-R is the distance below the unperturbed interface of the sphere center (i.e., r_c is the center's r coordinate). Since an unpertubed planar interface is free of vertical forces, the two expressions are written in terms of θ_c, the angle adopted, rather than θ_e. Using values of θ_c reported in Figure 4.12a, s_c and $(r_c-R)/a$ are plotted against $\sin\theta_c$ and $\cos\theta_c$, respectively, in Figures 4.12b and 4.12c, and agreement with expectation in both cases is excellent. By replacing θ_e with θ_c, Figures 4.12b and 4.12c suggest that Equations 1 and 2 apply in actual practice to spheres on cylindrical liquid interfaces. To verify the speculation, after making the substitution, Figures 4.12d-e plot menisci characteristics in ways suggested to isolate impacts from three parameter combinations, $a\sin\theta_c$, s, and D. The deformation was proportional to $(a \sin \theta)^4$ and $1/s^2$, conforming well to Equation 1 (Figure 4.12d-e). Contrary to the prediction $\zeta\sim D$, the particles were insensitive to D (Figure 4.12f) because of the angle hysteresis and small variable range (D=0.002-0.006 μm^{-1}).

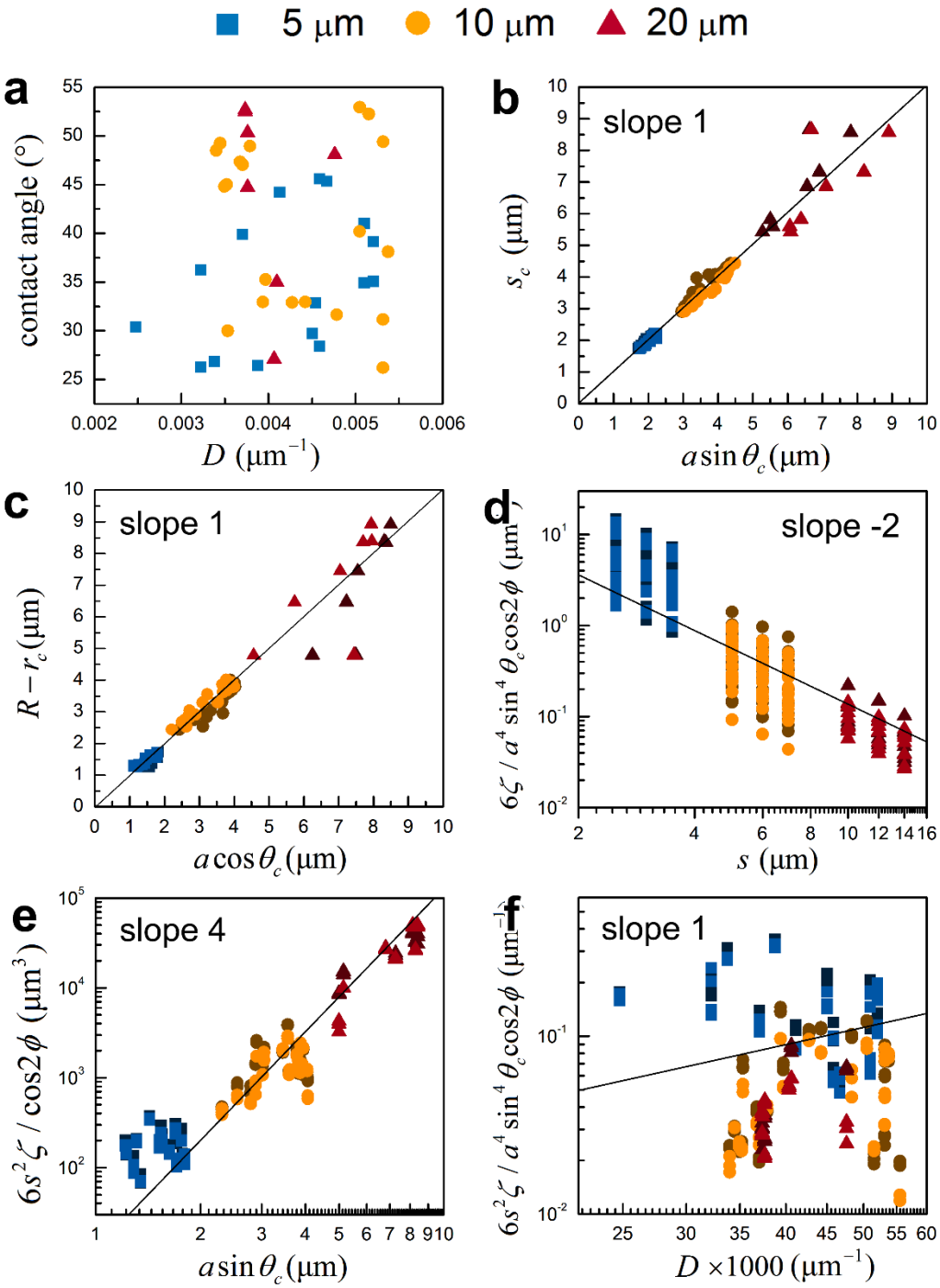

Figure 4.12 Evaluation of interfacial deformations (air/BH-DMAS interface) from the measurements at different *a*, D. Each data point was extracted from the particular position on the interface (ϕ=0, 90, 180, 270˚, *s*=*a*, 1.2*a*, 1.4*a*). (a) Inconsistent θ_c (b) $s_c \sim a \sin\theta$ (c) $r_c \sim R + a\cos\theta$ (d) $\zeta \sim 1/s^2$ (e) $\zeta \sim (a\sin\theta)^4$ (f) No $\zeta \sim D$

4.3.3.5 Self-Assembly and Alignment of Particles

Oriented relative to the cylinder axis, the meniscus quadrupoles drive the microspheres to assemble into square lattices of the same orientation. Figure 4.13a shows images of three 5-μm particle assemblies; the short experimental timeframe combined with the low areal density of particles limited assemblies at this condition to just a few particles, which bound together irreversibly. As anticipated, attractions between spheres were dominantly expressed in axial and perpendicular directions, corresponding to increased overlap of meniscus regions of the same sign in ζ. To the contrary, but as also expected, assembly did not much occur in the off-axis directions because, in these scenarios, strong repulsion would be experienced as meniscus regions of the opposite sign in ζ approached each other. Irrespective of configuration, assemblies showed a strong tendency to form along the cylindrical segment centerline, an outcome illustrated in the images of Figure 4.13b. This tendency reflected the capillary repulsions between spheres and pinned cylinder segment-substrate contact lines; the reduction of cylinder height near these lines generated capillary forces on a sphere analogous to the electrostatic forces on a charge near dielectric boundaries, forces that are often modeled through image charges. Here, one imagines a repulsion generated by a hypothetical particle of inverted meniscus and located at the same distance from, but on the opposite side of, the contact line.[132, 133] Positioning of a sphere, or sphere assembly, at the cylindrical segment centerline minimizes the repulsions.

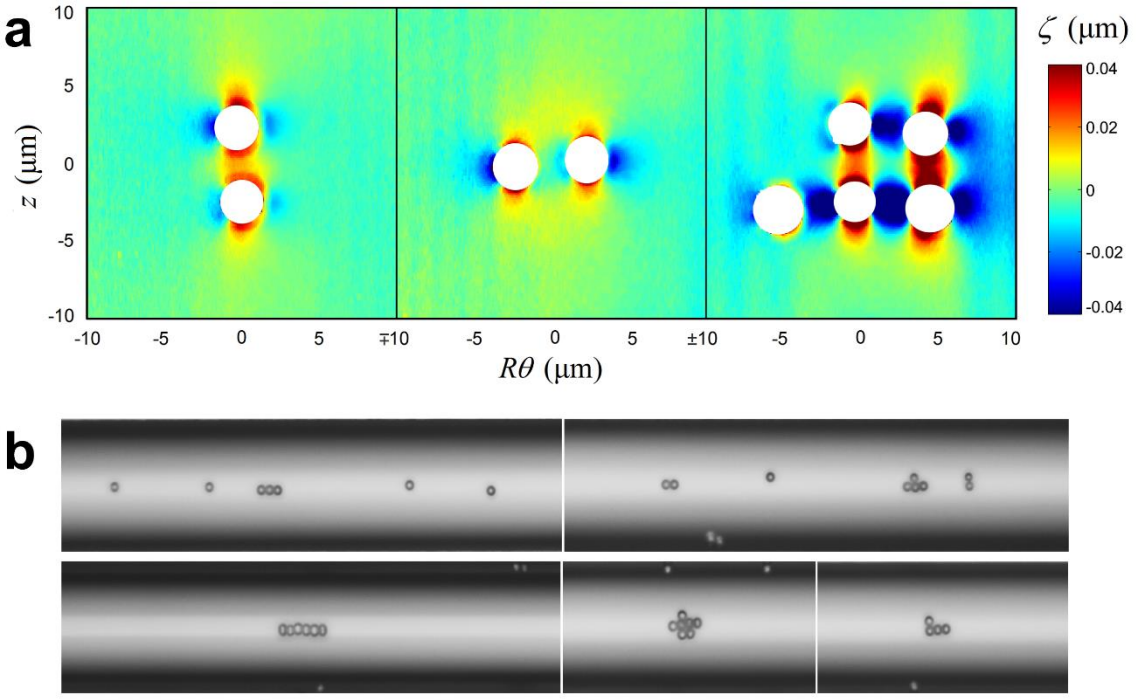

Figure 4.13 Self-assembly and alignment of 5-μm polystyrene spheres along the midline of a cylindrical air/BH-DMAS interface. (a) Deformation image of two or more particles assembled in a tetragonal lattice. (b) Optical micrographs of particles on the interface aligned along the midline.

4.3.3.6 Lateral Capillary Interaction

Equation 2 makes predictions for the d and ω dependences of $F(d,\omega)$ that are best tested by tracking the relative motion within an isolated pair of approaching microspheres. Each sphere follows an equation of motion that balances $F(d,\omega)$ against the viscous force generated by lateral sphere displacement across the interface. At small d ($<<a$), this resistance will depend on d and ω due to complicated interfacial hydrodynamic interactions, but at larger d, where the interactions weaken, these dependences will disappear, making $F(d,\omega)$ proportional to particle velocity $v(d,\omega)$, where the proportionality constant is the unknown but d- and ω-independent friction coefficient of

an isolated single sphere. Assuming validity of Equation 2, this coefficient can be deduced by establishing the $F(d,\omega)$ vs. $v(d,\omega)$ relationship; viewed differently, the coefficient simply re-scales the time of interaction t. The experimentally determined pair trajectories were assessed relative to theoretical pair trajectories predicted without hydrodynamic interactions. In the calculations, one sphere was fixed at the (z,y) position (0,0), and the approach trajectory of a second sphere was integrated numerically in t from its initial relative position $(z_o,y_o)=(d_o\cos\omega_o, d_o\sin\omega_o)$ to its current relative position (z, y).

Unlike the purely attractive or repulsive interactions of monopoles, which produce pair trajectories in which motion is either linearly inward or outward, the more complex interactions of two oriented quadrupoles lead, in general, to curved pair trajectories that vary both z and y in t. In concept, capillary quadrupoles interact exactly as do electrostatic quadrupoles confined in two dimensions. For the systems studied, interactions during approach do not rotate the quadrupoles, demonstrating that interface curvature was sufficient to maintain quadrupole orientation relative to the cylindrical axis. Thus, in calculating pair trajectories, quadrupole orientations were assumed aligned and fixed. Depending on ω, the instantaneous interaction between two oriented quadrupoles can be either attractive or repulsive. Interactions parallel and perpendicular to the cylinder axis for capillary quadrupoles are purely attractive, whereas interactions in directions shifted by 45º from these axes are purely repulsive; in either case, pair trajectories should not deviate from radial. At other ω, where interactions possess a ω component, pair trajectories will curve, but nonetheless, at large enough t, two spheres should eventually attract along an inward path parallel or perpendicular to the cylinder axis. These features are displayed in the numerical calculations summarized in Figure

4.14, which presents pair trajectories for a range of ω_o. (In terms of figure variables, by the form of the equation of motion, trajectories are distinguished by ω_o alone. To prevent sphere overlap, actual trajectories would terminate before reaching the origin. The predicted trajectories are a type of Lissajous curve.) Unless initially aligned 45º off-axis, the calculations show that two particles should assemble tetragonally irrespective of their initial configuration, and with the strength of their interaction decaying with *d*, the rate of assembly (approach) is anticipated to accelerate as spheres come together.

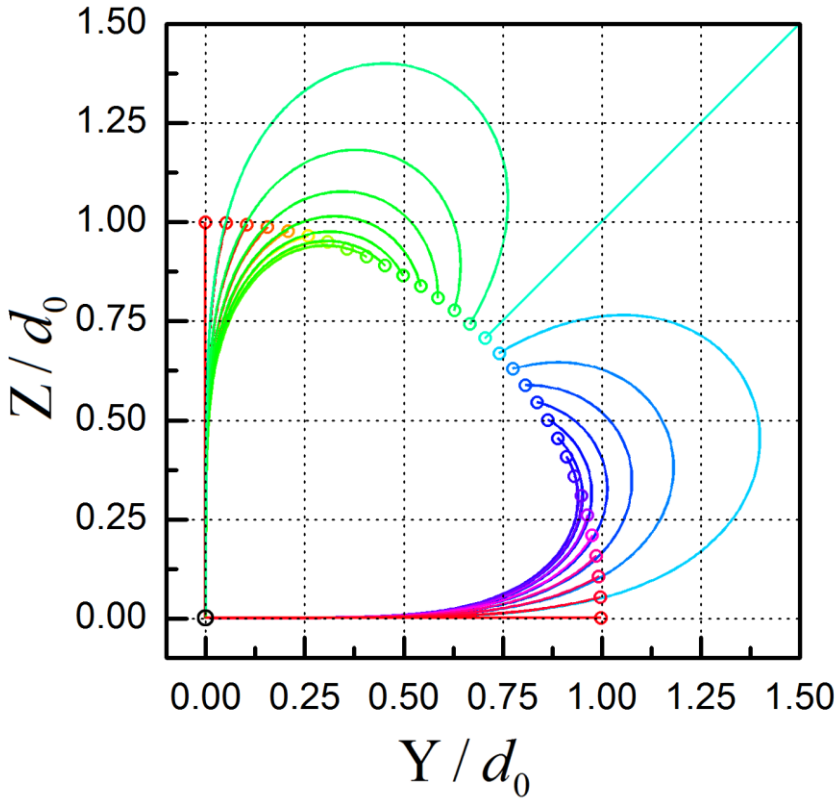

Figure 4.14 Relative trajectories of a particle from equal d, different ω (0-90° with 3° interval) calculated from Equation 2.

Figure 4.15 shows six experimental pair trajectories for 10-μm spheres bound to a liquid-liquid interface. Pairs 1-3 were chosen for ω_o clustered relatively near to the z-

axis (-20º≤ ω_o ≤12º, where ω_o is 0º at the axis), and pairs 4-6 were chosen for ω_o clustered relatively near to the y-axis (256º≤ ω_o ≤282º, where ω_o is 270º at the axis). For all pairs, d_0 was ~6a, corresponding to the weak far-field meniscus, and to minimize hydrodynamic interactions, tracking was terminated at d≈2.5-3a.[134] As predicted by theory, pair trajectories were curved, more so for larger departures of ω_o from the z- or y-axes. Also as predicted, trajectories eventually pointed inward along the z- or y-axis closest to ω_0.

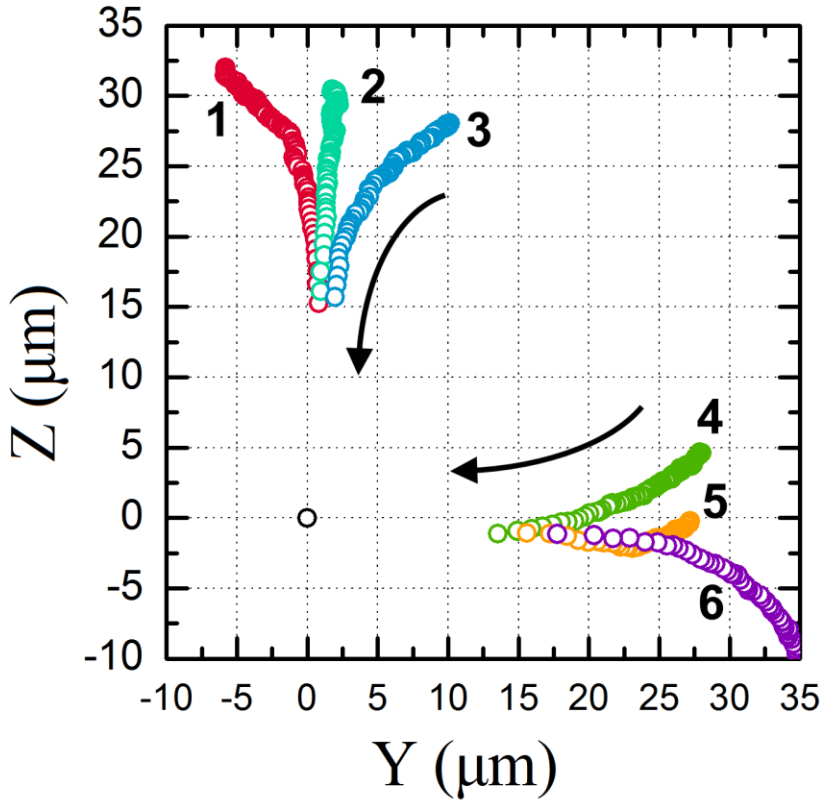

Figure 4.15 Relative trajectories of six particles from different initial ω.

Finally, the anticipated acceleration of the spheres towards each other was abundantly clear in the movie sequences. Analyzing the t-dependence of data in Figure 4.16 plots the z-component of $v(d,\omega)$ vs. d for pairs 1-3, those closest to the z-axis and thus moving at

highest speed in this direction. The plotted velocity component is normalized with the theoretically expected factor $\cos 5\omega$ to highlight its d-dependence, which Equation 2 predicts obeys a power law of exponent 5. Figure 4.16 also plots the analogous y-component velocities for pairs 4-6, those closest to the y-axis. In both cases, since the capillary force in the far field is small, with velocities correspondingly small, noise across this region is substantial. Nevertheless, the predicted exponent well fits the data, especially for smaller d, strongly supporting the theory for quadrupolar interactions. The spheres accelerate towards each such that their approach velocity rises by almost an order of magnitude in the narrow region of sphere separation between $6a > d > 2a$ reflecting the radial span of the meniscus.

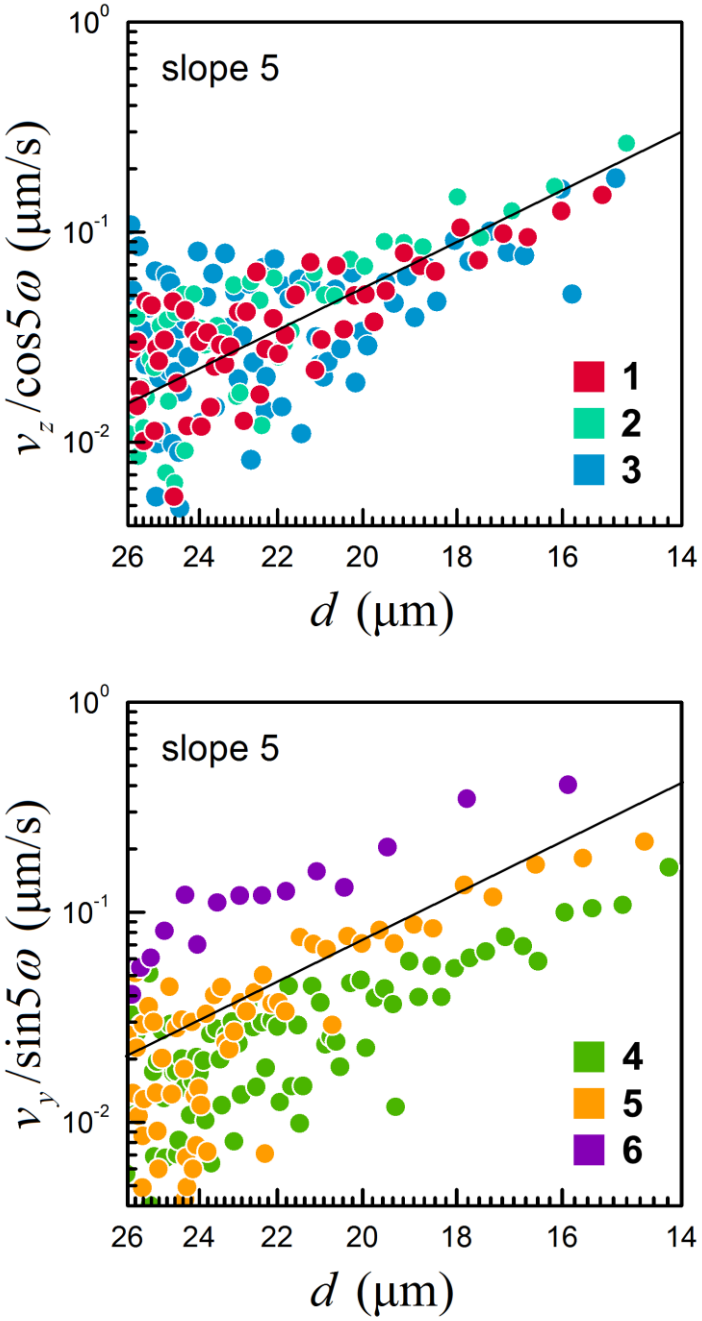

Figure 4.16 Capillary interaction between two 10-μm spheres on a cylindrical PEG400/silicon oil interface. (a) Interparticle speed in z direction vs. d, measured from trajectories 1, 2, 3. (b) Interparticle speed in y direction vs. d, measured from trajectories 4, 5, 6.

4.4 Conclusions

Affected by anisotropic curvatures, spherical microparticles created quadrupole deformations when they were bound to cylindrically curved liquid interfaces. Although the constant-contact-angle condition was disregarded by surface inhomogeneity, the deformations corresponded well to the theoretical predictions. However, to understand on how the deformations were created, the displacement of the contact line should be measured over the time span.

The arrangement of particles in tetragonal lattice and its alignment by capillary interactions present the opportunity of a new approach for the manipulation of micro-sized objects. Designing the interfacial curvature in elaborate structures will allow directed self-assembly of particles at specific locations, which should be useful with the potential applications in fabrication of functional devices or materials with enhanced properties, in encapsulation, and in emulsion production.

CHAPTER 5

IONIC LIQUIDS AS FLOTATION MEDIA FOR CRYO-ULTRAMICROTOMY OF SOFT POLYMERIC MATERIALS

5.1 Introduction

The preparation of samples for TEM can be both time-consuming and prone to the creation of imaging artifacts. To minimize multiple scattering effects, the sample thickness must be comparable to, or less than, the electron mean free path, about 20-30 nm.[135] For many 'soft' polymers, such thicknesses are best achieved with diamond knife ultramicrotomy. After microtomy, the cut sections typically are floated onto a liquid to facilitate their transfer onto a TEM grid. With a high surface tension γ ($72.8 mN \cdot m^{-1}$), water is an excellent room temperature flotation medium. However, when the sample's glass transition temperature lies below the freezing point of water, cryomicrotomy is necessary, and the choice of a flotation medium becomes more difficult. In addition to large γ, desired properties include low viscosity η, low volatility, low toxicity, and negligible mutual solubility.

Values of γ and melting temperature T_m for some common flotation media are listed in Table 5.1. Each has one or more drawbacks. The popular molecular solvent isopentane, for example, not only has high vapor pressure and low γ, η rises sharply when T_m is approached by cooling. Water-based antifreeze solutions incorporating either glycerol and dimethylsulfoxide (DMSO) are good alternatives, [136] but the high T_m of the former and the pungent odor of the latter present difficulties. If mutual solubility precludes sample-to-liquid contact, an eye brush or steel needle may be chosen to position dry sections on a

TEM grid. Alternatively, a drop of a sticky liquid, perhaps an aqueous solution of sucrose or methyl cellulose, can be used in conjunction with the brush or needle for positioning. [137, 138] Although such 'drop-and-pick-up' methods perform adequately at low temperature, considerable experience, luck, and/or manual dexterity are required. With sticky sucrose drop, for example, soft contact and subsequent maneuvering must be completed before ice crystals form. Moreover, if the solution adheres to the section, evaporation produces contaminating sucrose crystals.

Flotation media	γ /mN·m^{-1}	T_m /°C
2 M sucrose solution (aq)	75.8	-3.7
50% glycerol solution (aq)	68	-15
50% DMSO solution (aq)	71.9	-80
Isopentane	16.1	-160

Table 5.1. Surface tension γ and melting temperature T_m of several ultracryomicrotomy flotation media

Flotation media	γ /mN·m^{-1}	η /mPa·s	T_m /°C	T_g /°C
1-ethyl-3-methylimidazolium ethylsulfate	49.2	122	-	-87
1-butyl-3-methylimidazolium tetrafluoroborate	45.6	219	-81	-81
1-butyl-3-methylimidazolium hexafluorophosphate	43.4	312	10	-80
tri(butyl)ethylphosphonium diethylphosphate	33.3	541	-	-75

Table 5.2. Surface tension γ (at 20°C), viscosity η (at 25°C), melting temperature T_m, and glass transition temperature T_g of tested ILs [139-141]

Here, ionic liquids (ILs) and their mixtures with several conventional solvents are presented as a new category of cryo-ultramicrotomy flotation media. ILs are salts that pair a bulky, asymmetric organic cation with a small inorganic anion to form a liquid that melts near or below room temperature. Many ILs exhibit a broad liquidus range, the temperature span over which their liquid state is preserved, and importantly, the liquidus range can extend far below room temperature, typically (but not always) terminated on the low end by a glass transition. ILs often display relatively high γ, in many instances, in the range 30-80 $mN \cdot m^{-1}$ at 20 °C.[141] Finally, ILs are essentially nonvolatile, especially at the low temperatures of contemplated use. These properties suggest that ILs might serve as excellent flotation media for cryo-ultramicrotomy or ultramicrotomy. Adding to these advantages, hundreds of ILs are commercially available. Even more, if needed, IL properties are easily tailored by swapping their cation and/or anion.

5.2 Experimental

5.2.1 Materials and Sample Preparation

Table 5.2 lists the four ILs examined, each possessing large enough γ (>30 $mN \cdot m^{-1}$at 20°C) to float polymer sections easily. With the lowest tabulated T_g, -87 °C, 1-ethyl-3-methylimidazolium ethylsulfate ([emim][$EtSO_4$]), a gift of Evonik Goldschmidt GmbH (TEGO IL IMES), appears best suited for the lowest temperature applications; this and the other ILs discussed are commercially available from Sigma-Aldrich, Strem chemicals and other vendors. This as-received IL, with a slight amber color, was purified by adding activated charcoal (Acros Organics) and dichloromethane,[142] the mixture stirred for 48 h before sequential filtration through a Celite 545 column and a PTFE 0.2-μm membrane.

After solvent removal at reduced pressure, the IL was dried in a vacuum oven at 60 °C overnight. Because of hygroscopicity, dried [emim][$EtSO_4$] was stored in a nitrogen glove bag before use. The other ILs were similarly dried and stored under nitrogen before use. The same imidiazolium cation is maintained in three of the ILs, varying just the identity of the anion, while the fourth IL is from the chemically distinct family of phosphonium salts. All four ILs mix with low molecular weight alcohols (ethanol, methanol, 2-propanol; Fisher Scientific) as a minority co-solvent.

To explore the neat ILs as well as their alcohol mixtures for cryo-ultramicrotomy, isotactic polypropylene (iPP), poly(styrene-b-isoprene) (PS-b-PI), and poly(styrene-b-butadiene) (PS-b-PBD), with nominal lowest T_g values of 0 °C, -73 °C, and -104 °C, respectively, were chosen as representative soft polymer systems. iPP (Braskem PP D115A, melt flow index of 11) was spread on a glass slide at 200 °C as a 3 mm-thickness film and rapidly cooled to room temperature in water to nucleate the alpha crystal phase. After detachment, the film was cut directly into a trapezoid shape for microtoming (*i.e.*, not embedded in an epoxy resin). The block copolymers PS-b-PI and PS-b-PBD, both purchased from Polymer Source (PS-b-PI: PS block=31000 g/mol, PI block=12000 g/mol, M_w/M_n=1.05; PS-b-PBD: PS block=28400 g/mol, PB block=13600 g/mol, M_w/M_n=1.05), were first spun-coat onto silicon oxide substrates as10 wt. % toluene solutions. After 6-h vacuum removal of solvent at room temperature, the cast films were thermally annealed at 120 °C for 24 h. Floated from their substrates over 5% aqueous HF solution, the films were recovered on a small polystyrene plate and sputter-coated with 2 nm of gold to assist in sample location during TEM. Finally, the films were embedded in an epoxy resin.

5.2.2 Cryo-Ultramicrotomy

After mounting in the microtome (Leica Ultracut UCT equipped with Leica EM FCS), polymers were cooled below T_g (or, for the block copolymers, below T_g of both components) and trimmed with a razor blade and then a glass knife to create a smooth, 0.5 mm square tip. After pouring the IL into the microtome trough, 50-nm sections were cut at 1.0 mm/s with a diamond knife (Diatome), these sections deposited directly on the IL to minimize handling stresses. The sections were then picked up on a 400-mesh copper grid, and if any residual IL remained, the liquid was blotted away by placing the grid on filter paper (Whatman). Finally, iPP sections were vapor-stained with ruthenium tetroxide (30 min, Electron Microscopy Sciences), and PS-b-PI and PS-b-PBD sections were vapor-stained with osmium tetroxide (150 min, Sigma-Aldrich). To establish that the ILs or their minority alcohol mixtures do not create imaging artifacts, control samples of each polymer type were prepared by dry cutting, with each cut sample directly placed on a 600-mesh copper grid.

5.3 Results and Discussion

With sample and microtome knife temperatures set to-115°C, and the trough set to-120 ºC, PS-b-PBD sections were floated onto [emim][$EtSO_4$] and then successfully lifted onto TEM grids. As the latter temperature is below the IL's T_g, the trough was filled just before cutting, which allowed several minutes before IL vitrification. Even so, the IL was highly viscous ($\eta > 10^4$ $mN \cdot m^{-1}$),[143] making reproducible manipulations difficult. To lower and better control η at these temperatures, three low molecular weight alcohols, ethanol, methanol, and 2-propanol, were explored as [emim][$EtSO_4$] co-solvents. At minority

compositions, all three mix miscibly with the IL, not only lowering η but also depressing T_g. Adjusting co-solvent identity and concentration alongside temperature, optimal parameters for sectioning PS-b-PBD were 40 vol. % ethanol and -120 °C. (Throughout the optimization, the sample and knife temperatures were kept 5 ºC higher than the trough temperature.) At -90 °C, η for the IL:ethanol mixture is similar to that of the neat IL at room temperature.

At the optimal composition, γ=25.1 $mN \cdot m^{-1}$was determined at room temperature by a pendent drop tensiometer (Dataphysics OCA 20). Measuring γ at the trough temperature would be much more difficult, but approximately the same fractional reduction as at room temperature (25.1/49.2) would be expected for the ethanol addition, a trend supported by the ease at which cryomicrotomed polymer sections were floated on the cooled liquid mixture. Miscibility of [emim][$EtSO_4$] and ethanol at low temperature was confirmed by differential scanning calorimetry (TA Instruments Q200 DSC) heating runs performed from -150°C to 60 °C at 10 °C/minute. The mixed liquid displays a single T_g(-129 °C) that is significantly lower than the T_g of neat [emim][$EtSO_4$] or the freezing point of ethanol (-114 °C). The other ILs of Table 5.2, as well as their mixtures with ethanol, methanol, and 2-propanol, performed similarly as floatation liquids, although its lower T_g endows [emim][$EtSO_4$] and its mixtures a lower range of operating temperatures. Because of potential exposure to its toxic vapor during cryo-ultramicrotomy, methanol as co-solvent is not recommended.

For the optimal 60:40 (v/v) mixture of [emim][$EtSO_4$] and ethanol, Figure 5.1a shows the floating of polymer sections in the cryo-ultramicrotomy trough. Each section was cut and floated at a temperature appropriate to the specimen's thermal properties: -30 °C for

iPP, -90 °C for PS-b-PI, and -120 °C for PS-b-PBD. Figure 5.1b shows the corresponding TEM images. Sections were well flattened, and there is no indication of residual adhered liquid. As expected, the floated PS-b-PI and PS-b-PBD sections adopt well-ordered lamellar block copolymer morphologies whereas the iPP section exhibits a semi-crystalline spherulite morphology; the latter is shown at lower magnification to illustrate the characteristic features of a single spherulite. For temperatures above -100 °C, the liquid mixture functions effectively as a flotation medium for at least several hours, its properties unchanged with time. Nearer the mixture's T_g of -120 °C, however, η becomes too high to float specimens after several minutes in the trough. For comparison, Figure 5.1c offers images of the same three samples made with dry cutting; temperatures of microtome knife are as cited for the IL mixture. For all three systems, the images obtained after flotation on the IL mixture are comparable to those achieved by dry-cutting, a comparison that proves that neither IL nor co-solvent disrupt polymer morphology.

The key benefits of the IL mixture method lie in much reduced sample preparation effort and time; the time advantage for the systems examined here was more than an order-of-magnitude. Somewhat better sample flattening is an additional benefit of a flotation approach. ILs are inherently hydrophilic (more properly, polar), a property that leads to dewetting of hydrophobic polymer surfaces; such dewetting aids blotting as a means to remove any residual adhering liquid. For more hydrophilic polymers than those studied, the nonvolatile IL probably can be removed by rinsing with water or alcohol. A careful examination of the images for PS-b-PI in Figures 5.1a and 5.1b uncovers a difference in the lamellar domain spacing, larger for the dry cut method than for the IL-mixture method. We believe the difference is attributable to a greater deformation of the

dry cut sample during cryo-ultramicrotomy, although alternative explanations are possible.

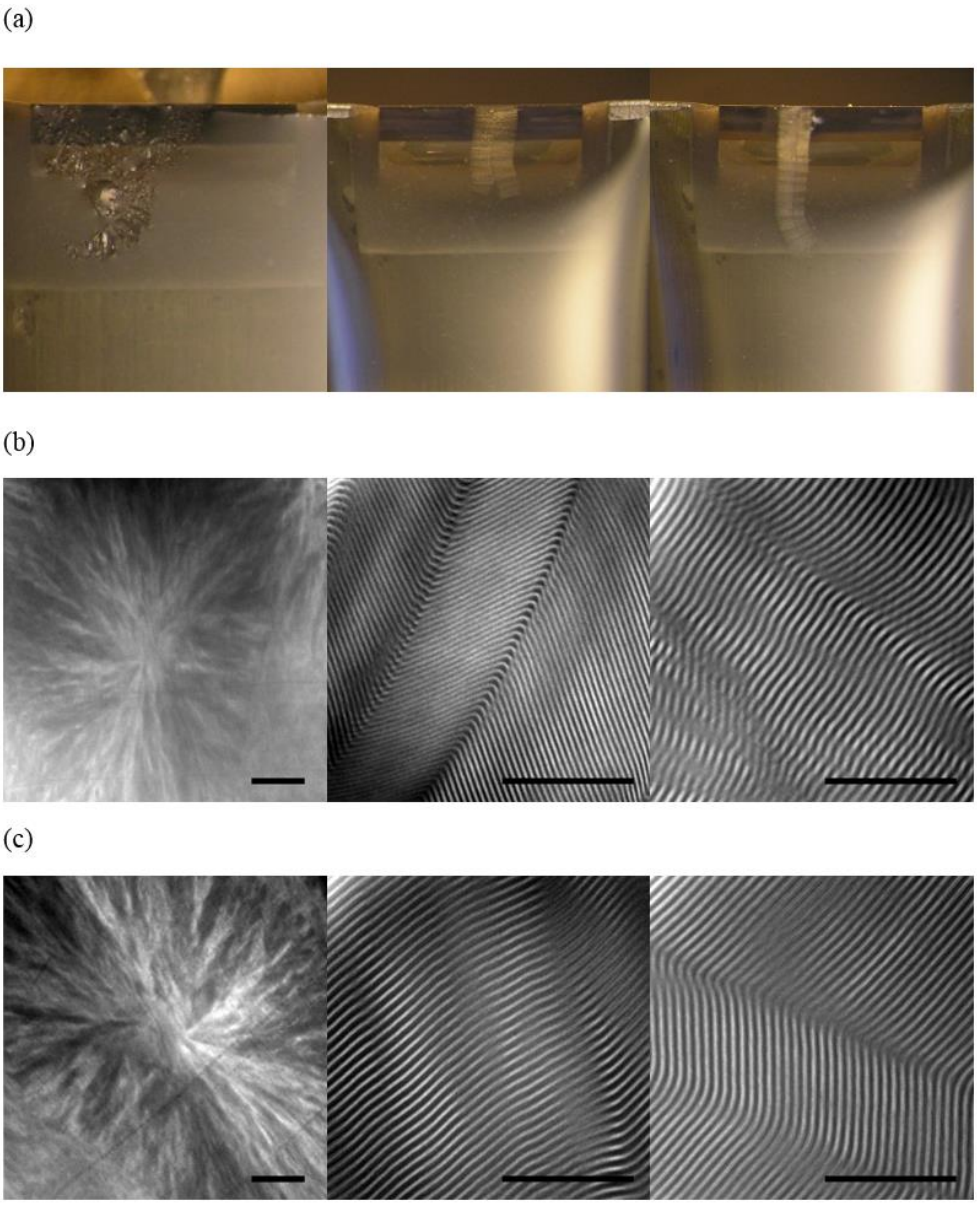

Figure 5.1. Comparison of floated sections on ionic liquid (a) Sections floating on [emim][$EtSO_4$] mixed at 40% v/v with ethanol: (left) iPP cut at -30 °C; (center) PS-b-PI cut at -90 °C; and (right) PS-b-PBD cut at -120 °C. (b) TEM images from the sections of (a): (left) iPP; (center) PS-b-PI; and (right) PS-b-PBD. Scale bar sizes, from left to right: 2 μm, 500 nm, and 500 nm. (c) TEM images of ultracryomicrotomed sections retrieved without use of floatation liquid: (left) iPP; (center) PS-b-PI; and (right) PS-b-PBD. Scale bar from left to right: 2 μm, 500 nm, and 500 nm

5.4 Conclusions

We presented a versatile new approach to use Ionic liquids as flotation media for cryo-ultramicrotomy. The use of ILs opens new windows of opportunities for this long standing TEM sample preparation technique through tailor-made floatation media. While we could demonstrate the usability and advantages for synthetic polymer materials we believe that the method will have application in the life sciences and medical field as well.

APPENDIX A

STRUCTURES ANALYSIS OF NANOPARTICLE DISPERSIONS IN IONIC LIQUID BY X-RAY SCATTERING

Ionic liquid (IL) has been a prospective candidate for colloidal dispersing media of nanoparticles (NPs) due to its unique physiochemical properties. A number of colloidal systems with ILs have recently been reported with regard to the dispersion of metal and semiconductor nanoparticles, including *in-situ* nanomaterial synthesis in ILs, enhancement of colloidal stability in ILs, phase transfer to ILs from other dispersed media, and catalytic reaction using metal nanoparticles in ILs. In contrast to these advances, few studies have been carried out on the fundamental colloidal properties in ILs. To understand spatial arrangements of the system, NPs/IL dispersions were measured by small-angle X-ray scattering (SAXS) and wide-angle X-ray scattering (WAXS). Micro- and nanoscale structures of the NP-IL system were characterized in terms of average particle size, distribution, and crystal structure.

Three sizes of gold NPs were purchased from Nanocomposix. The average diameters were 5 nm, 10 nm, and 20 nm. For good dispersibility in IL, NPs was surface-decorated by polyethylene glycol (PEG-SH, 5000 g/mol). NPs were rinsed repeatedly with deionized water before re-dispersion in IL; NPs were pelleted by centrifugation and then vortexed with IL. Hydrophilic IL, 1-ethyl-3-methylimidazolium ethyl sulfate [emim][$EtSO_4$], was used as a dispersant. Residual water in the mixtures was removed in

a vacuum oven for 48 h at 70°C. The dried samples were sealed in 20 ml vials after purging with nitrogen gas.

SAXS and WAXS measurements were performed at the room temperature on five samples, as summarized in Table A.1. Tests were run on a Nano-inXider system at Xenocs HQ in Sassenage, France. The instrument was equipped with Cu Kα 8.04 keV source and Pilatus 100K detector. The samples were spread across 1×1 mm^2 holes on a 50-μm thick polyimide film (*i.e.* Kapton). The liquid formed freestanding films without touching the solid surface.

#	Sample
1	IL
2	Empty
3	5-nm gold NPs + IL (0.5 v/v %)
4	10-nm gold NPs + IL (0.5 v/v %)
5	20-nm gold NPs + IL (0.5 v/v %)

Table A.1 Lists of samples measured by X-ray scattering

Two dimensional (2D) scattering patterns were acquired under continuous vacuum from source to detector, ensuring the highest signal-to-noise ratio. The 2D patterns were azimuthally integrated and plotted in 1D profiles as a function of q-vector or 2θ. SAXS and WAXS were collected at the same time. High resolution (HR) mode was selected as a resolution setting; q-range covered [0.0054, 4.3] $Å^{-1}$ with a nominal resolution of 7.5×10^{-4} $Å^{-1}$. For all samples, 60-600 s was sufficient for quantitative analysis.

Azimuthal Averaging of 2D Scattering Patterns:

SAXS/WAXS patterns collected for 1 min from the samples are presented in Figure A.1. The overall scattered intensity was related to the sample thickness. The crystal structures of gold and PEG were detected in ring patterns in the WAXS region. Integrated 1D profiles are shown in Figure A.2. The Foxtrot (*i.e.* Xenocs software) was used to perform data reduction. 1D curves were normalized with solid angle, exposure time, and transmitted intensity. A wide q-range [0.054, 4.3] $Å^{-1}$ acquisition was obtained by a single shot measurement.

Data collection for 1 min was already sufficient for most data analysis. However, the exposure time was further increased to enhance signal-to-noise ratio, especially for SAXS at high q values (>0.1 $Å^{-1}$). The longer exposure time allowed high signal-to-noise ratios throughout the entire q-range. The scattering range from the samples was broad, covering eight decades of intensity as shown in Figure A.2. SAXS data collected for 10 × 10 min are displayed in Figure A.3. The significant improvement of the signal-to-noise ratio was noted. 1D profiles were processed by the successive operations: background subtraction, scaling to sample thickness, and final subtraction from pure IL contribution.

Background Subtraction:

The scattering from background was eliminated by subtracting the empty camera curve from all measurements (Figure A.4). Owing to normalized scattered intensity, the subtraction was straightforward even for samples with different absorptions. To compare scattering profiles of different samples, subtracted intensities should be scaled to a specific sample thickness. The estimation of thickness required sample specifications (*i.e.* shape, chemistry, and transmission) or complementary experimental data. However, both

information was unavailable for NP dispersions. As an alternative approach, all curves were scaled to the IL curve; the curves were shifted using a common q-regions, where NPs do not interfere (nor in the form factor and the particle-to-particle structure factor neither in the intra-particle structure factor) with the IL. All curves were than divided by the IL thickness, which was calculated from scattered intensity. Precise approach would require the knowledge of the exact effective chemical composition of the sample mixture.

Matching to Pristine Ionic Liquid:

A position in WAXS region at q = 1.0 $Å^{-1}$ was selected as a scaling reference. The re-scaled curves are shown in Figure A.5. XRD peaks from gold crystals were appeared in WAXS at 38.1˚ and 43.3˚ (Figure A.6), which were broader for smaller particles. PEG crystals were also detected on the top of the broad IL double bump at 19.2˚ and 23.2˚; these peaks vanished mostly for 20-nm NPs.

Scaling to Sample Thickness:

The samples thickness was determined from transmitted intensity through the IL sample. Based on the NIST absorption table for Cu $Ka_{1,2}$ wavelengths, the absorption of X-ray by IL (*i.e.* $C_8H_{16}N_2O_4S$, 1.24 g/ml) was calculated as listed in the Table A.2. All data were then expressed in mm^{-1} by multiplying with a normalization factor (*i.e.* the inverse of the IL thickness). The scaling was a rough estimation, because the absorption by NPs was ignored.

List	Value
Transmission through IL	0.626
Linear absorption from NIST table	$\mu \sim 1.81\ cm^{-1}$
Calculated IL thickness	$-\ln(T)/\mu = 279.4\ \mu m$
Normalization factor *converts absolute intensity into* mm^{-1}	1/279.4 = 3.579

Table A.2 Parameters for the estimation of IL thickness

Subtraction from Pristine Ionic Liquid:

To estimate scattering exclusively from NPs, IL curve was subtracted from all data. I(q) was expressed in mm^{-1} using the normalization factor (Figure A.7). The curve slopes q^{-4} reflected the sharp interfaces of the Au NP surface. The observation proves that data resulting from subtraction was reasonable. However, the intensities were slightly over-subtracted as appeared at $q \sim 1\ A^{-1}$ with zero or negative values.

SAXS - Form Factor:

SASfit software was used to calculate form factors, particle-size distributions, and preliminary structure factors. The form factor was fitted by a simple model of hard spheres with log-normal size distribution in Figure A.8. The structure factor was modeled by square-well potential with decoupling approach in Figure A.9. The convolution of two models did not fit the measurements perfectly, especially for 5-nm and 10-nm NPs. The interaction between NPs was not clearly described by a simple square-well model; smaller NPs may incorporate faceted surface and cause complicated interactions. For 20-nm NPs, the oscillations at large q were not well described by the model in spite of a nice fit at smaller q-values. Thus, the models (*i.e.* size distribution and hard sphere) did not

offer the most adequate solution. More precise form factor models may be adapted for this system.

SAXS - Structure Factor:

The structure factor was considered after fitting the form factor. As mentioned above, the square-well potential was used as the structure factor. The model provided reasonable results for 10-nm and 20-nm NPs (Table A.3); 5-nm NP curve was not compatible with this model. Repulsion diameter estimated from square-well potential was much larger than the NP diameter; 24 nm and 29 nm for the 10-nm and 20-nm particles respectively. A rough estimate of the structure factor was also derived from the minimum of the curve in the I(q)*q vs. q representation. The characteristic distance is in the range of 30-40 nm for 5 nm particle (Table A.3), which is larger than the NP size.

Sample	Repulsion Diameter (from fit of square well potential)	Characteristic distance (from local minimum I(q)·q vs. q)
IL + 5-nm NPs	-	32 nm
IL + 10-nm NPs	24 nm	35 nm
IL + 20-nm NPs	29 nm	45 nm

Table A.3 Characteristic distances between gold NPs in IL

WAXS - Au Peaks Width:

The crystalline peaks from Au particles were easily quantified after subtracting the IL curve. SASit performed the double peak shape analysis with Pearson VII model to extract full-width at half-maximum (FWHM) of peaks. The aforementioned increasing peak width with decreasing particle size was clearly illustrated with FWHM of the [111] peak ranging from 0.192$Å^{-1}$ down to 0.067 $Å^{-1}$ for 5-nm and 20-nm particle respectively.

In conclusion, SAXS/WAXS measurements were performed on NPs-IL dispersions. Both SAXS and WAXS resolved nanostructures of the system by a single measurement. Investigated samples showed a high scattering dynamic range. Form factor of NPs and their size distribution were obtained from SAXS. A strong interaction between NPs was revealed with distances much larger than the particles diameter themselves. The gold NPs and PEG coating were found to be crystalline.

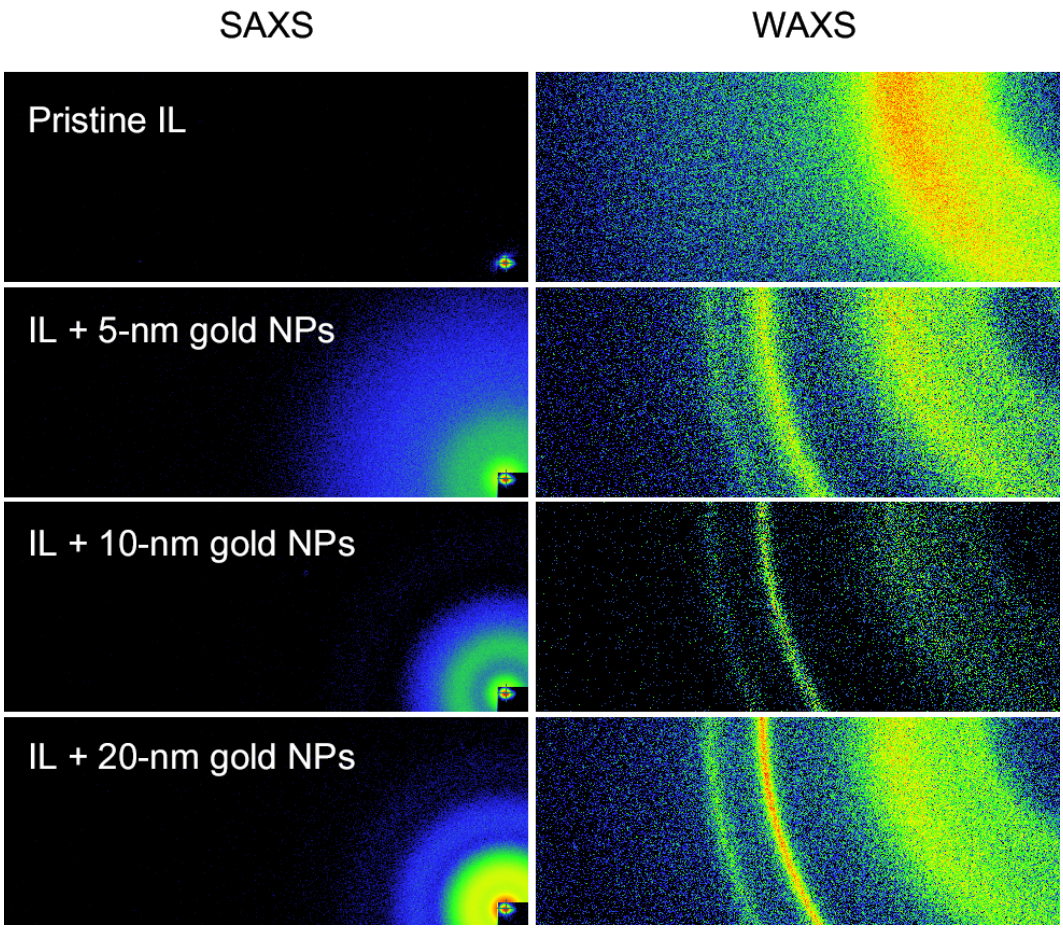

Figure A.1 2D SAXS and WAXS scattering patterns. Pristine IL, 5-nm NPs in IL, 10-nm NPs in IL and 20-nm NPs in IL.

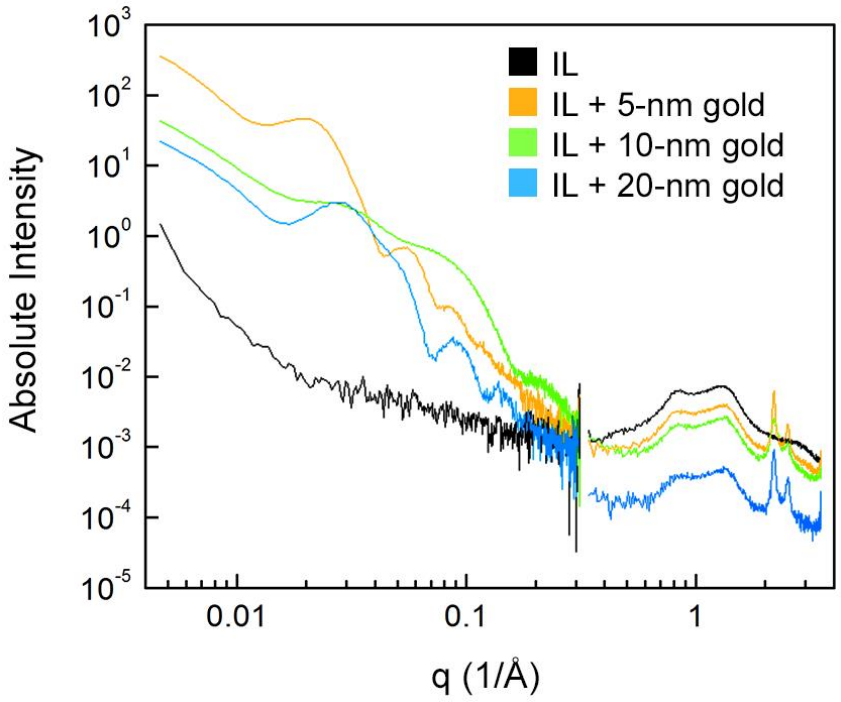

Figure A.2 SAXS/WAXS of IL (black), 5-nm NPs in IL (yellow), 10-nm NPs in IL (green) and 20-nm NPs in IL (blue). Exposure time was 60 s.

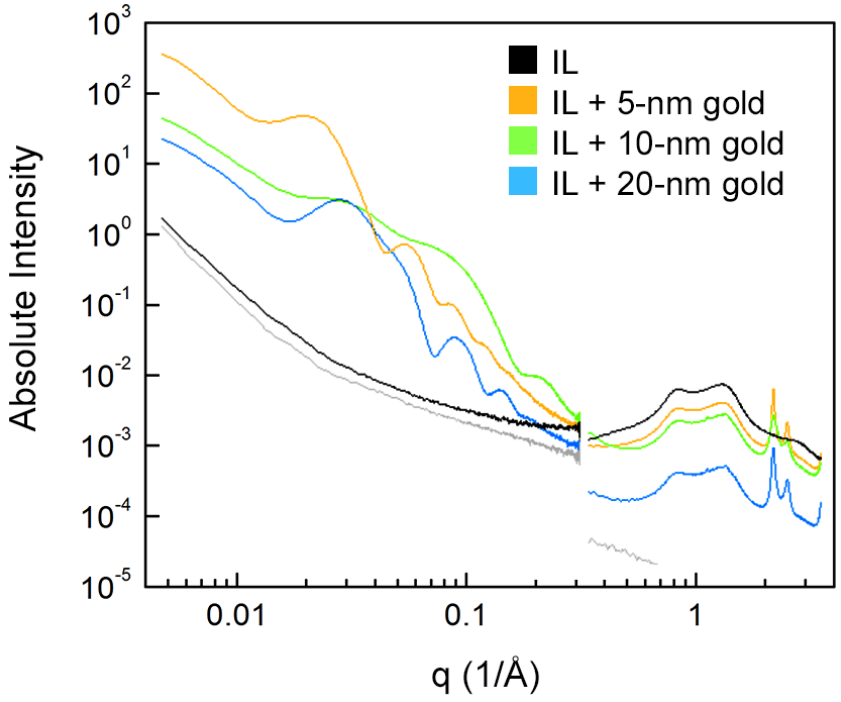

Figure A.3 SAXS/WAXS of empty camera (grey), IL (black), 5-nm NPs in IL (yellow), 10-nm NPs in IL (green) and 20-nm NPs in IL (blue). Exposure time was 10 × 600 s.

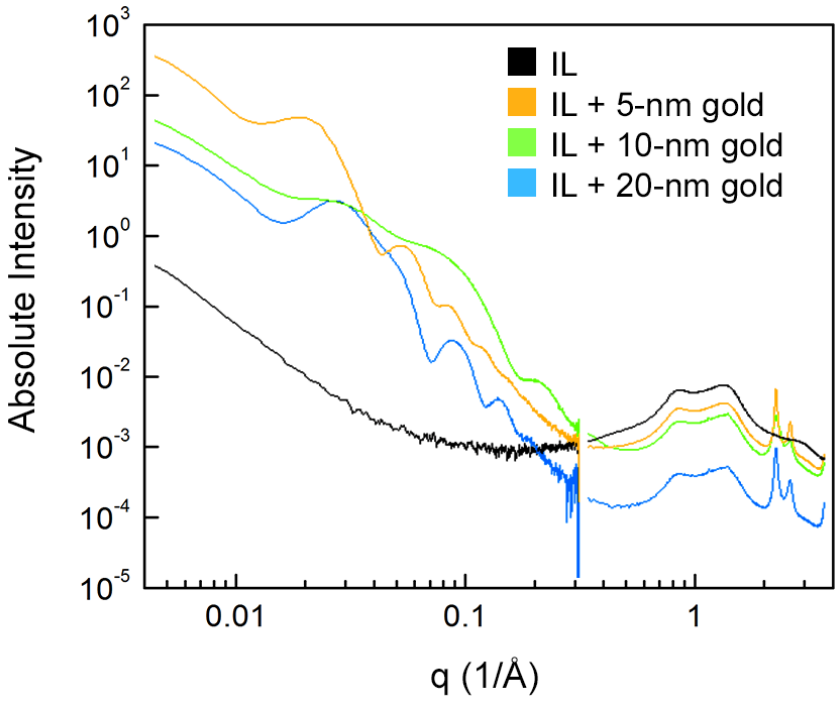

Figure A.4 SAXS/WAXS subtracted by empty camera. IL (black), 5-nm NPs in IL (yellow), 10-nm NPs in IL (green) and 20-nm NPs in IL (blue). Exposure time was 10 × 600 s.

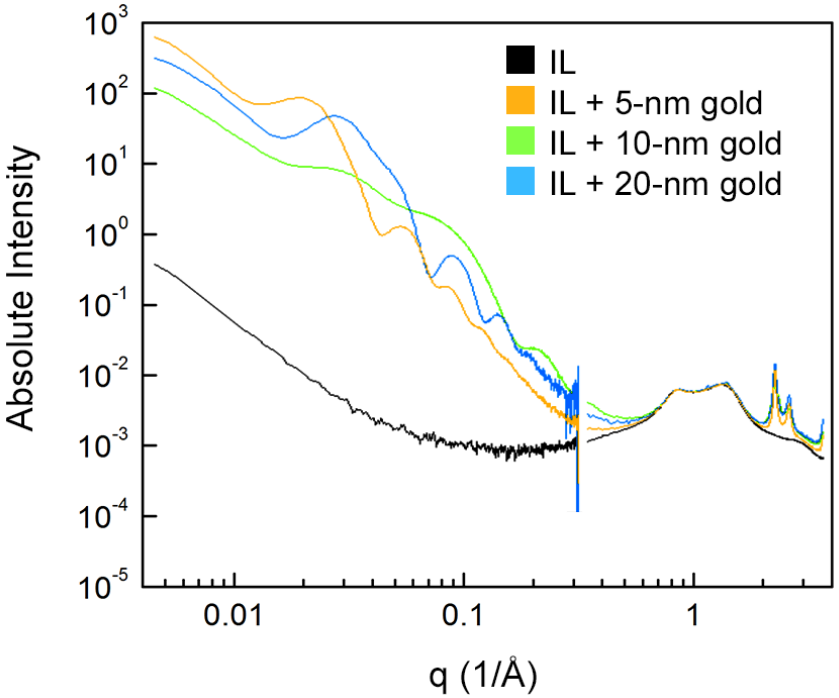

Figure A.5 SAXS/WAXS scaled to IL curve. IL (black), 5-nm NPs in IL (yellow), 10-nm NPs in IL (green) and 20-nm NPs in IL (blue). Exposure time was 10 × 600 s.

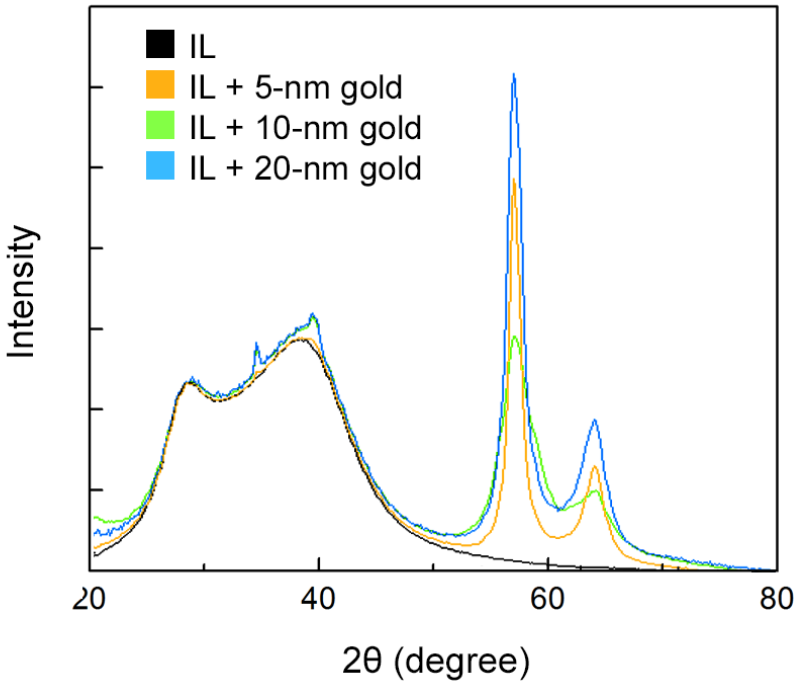

Figure A.6 WAXS region enlarged from Figure 8. XRD peaks at 38.14° and 44.30° correspond to Au crystallites; peaks were broader when NPs get smaller. Peaks at 19.2° and 23.2° were from PEG crystallites.

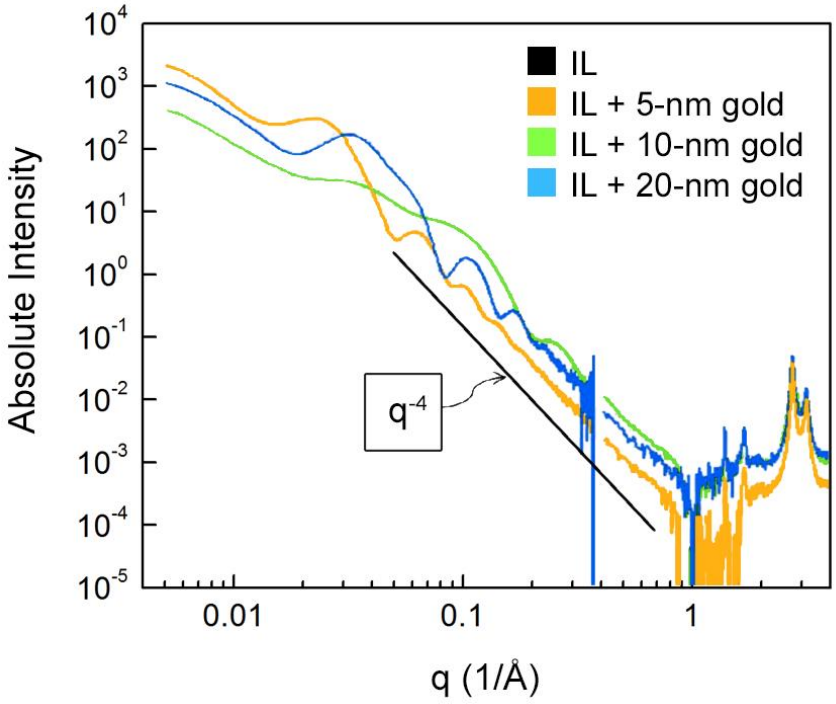

Figure A.7 SAXS/WAXS subtracted from IL curve. 5-nm NPs in IL (yellow), 10-nm NPs in IL (green) and 20-nm NPs in IL (blue). Exposure time was 10 × 600 s.

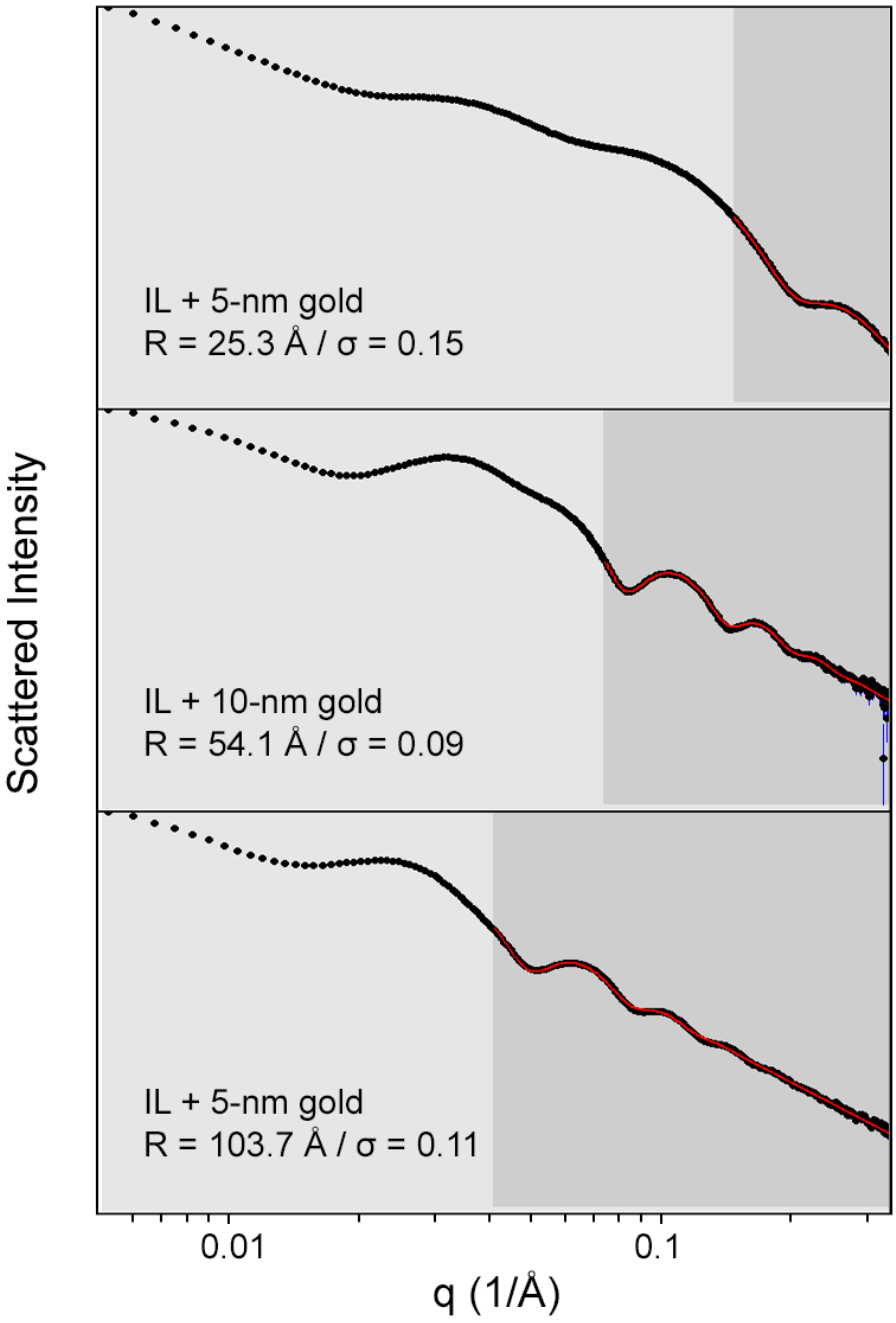

Figure A.8 Form factor fitting on SAXS data. 5-nm NPs in IL (top), 10-nm NPs in IL (center), and 2-nm NPs in IL (bottom). Measurement (black) and fitting (red) are overlaid.

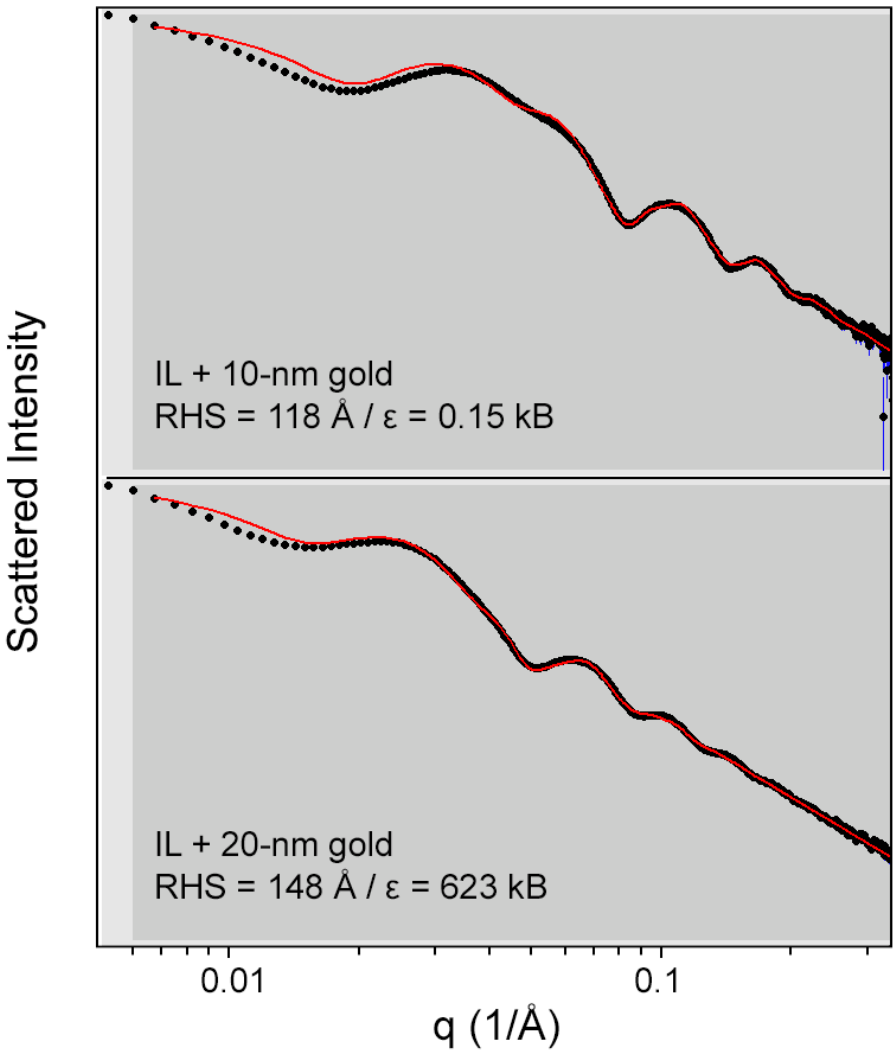

Figure A.9 Structure factor fitting on SAXS data. 5-nm NPs in IL (top), 10-nm NPs in IL (center), and 2-nm NPs in IL (bottom). Measurement (black) and fitting (red) are overlaid.

APPENDIX B

SOLUTION CRYSTALLIZATION OF POLYMERS FROM IONIC LIQUIDS

The polymer crystallization plays an important role in technological applications. Many of thermoplastic polymers crystallize to some extent when they are cooled below their melting temperatures. The procedure occurs repeatedly during polymer processing and the resulting properties are heavily influenced by the presence of crystals. Therefore, it is important to understand why and how polymer molecules crystallize. Solution crystallization is an alternative way to crystallize polymers. Isolated polymer coils in dilute solutions start to crystallize when molecular interaction is increased *via* solvent evaporation, temperature decrease, or solvent change. Solution-grown polymer crystals have higher degree of perfection than melt-crystallized counterparts, because molecular rearrangement and cooperative movement are less hindered by chain entanglement. Depending on the molecular structure (*i.e.* tacticity, extent of branching, side group size, and complexity of repeating unit), different morphologies of polymer crystals can evolve, including hollow platelet, hollow pyramids, spirals, and multilayer dendritic structures.

This section presents crystallization of polymers from dilute solutions in ionic liquids (ILs). ILs have emerged as effective and green solvents, mainly due to their high thermal and chemical stability, non-flammability and miscibility with many other solvent systems. A number of anions in ILs such as halides, phosphate, formate and acetate were found to dissociate multiple hydrogen bonds in biopolymers (*i.e.* cellulose-based thermoplastics and proteins). Dissolution of such polymers in ILs can be used to develop benign processing technologies that do not use toxic and non-recyclable chemicals. Despite great

advantages of ILs, no work has been reported until now about the systematic investigation on polymer crystallization from ILs. Our work was focused on finding the pairings of polymer and IL for solution crystallization either by lowering the solution temperature or by adding non-solvents into solutions. The crystal morphologies were imaged using optical microscopy, scanning electron microscopy (SEM), and transmission electron microscopy (TEM).

Finding pairings for solution crystallization:

Polyethylene glycol, polyvinyl alcohol, poly-L-lactide, polycaprolactam and poly(methyl methacrylate) were separately mixed (3-5 wt.% concentration) with ILs in 3-ml vials. Imidazolium and phosphonium based ILs were employed:

1-ethyl-3-methylimidazolium tetrafluoroborate, [EMIM][BF_4],

1-ethyl-3-methylimidazolium ethylsulfate, [EMIM][$EtSO_4$],

1-ethyl-3-methylimidazolium bis(trifluoromethane)sulfonamide, [EMIM][TFSI],

1-buyl-3-methylimidazolium bis(trifluoromethane)sulfonamide, [BMIM][TFSI],

1-buyl-3-methylimidazolium hexafluorophosphate, [BMIM][PF_6],

tributyl(ethyl)phosphonium diethylphosphate, [$P_{2,4,4,4}$][DEP].

The mixtures were heated in a vacuum oven at 80 °C for a week. If polymer is dissolved in an IL, the solution was slowly cooled down to room temperature. After three days, cooled samples were observed using optical microscopy to check the formation of crystallites. If crystallization does not occur at lowered temperatures, non-solvents were added to promote crystallization. Figure B.1 lists our finding of the polymer-IL pairings that exhibited solution crystallization. In most cases, polymers were phase separated from

solutions into solid particles near IL surfaces because of their lower densities.

TEM imaging of polymer crystallites:

Heated polymer solutions were spread into ultra-thin films on amorphous carbon TEM grids. The samples were re-crystallized into ensure that crystallites have thicknesses less than 100 nm; TEM grids were heated to 80 °C overnight and then cooled down to room temperature. To prevent water absorption, the samples were stored in a nitrogen glove bag before imaging with JEOL 2000-FX.

Optical microscopy of polymer crystallites:

A drop of polymer solution was applied on a microscope slide. The sample was observed using an optical microscope (Olympus BX-60) between crossed polarizer with transmitted light illumination. For hygroscopic ILs [EMIM][$EtSO_4$] and [$P_{2,4,4,4}$][DEP], the samples were placed in chamber purged with dry nitrogen gas during optical imaging. The evolution of crystal structures was imaged *in situ* by spontaneous temperature decrease.

Morphologies of crystallized polymers produced by lowering temperature:

Figure B.2 shows spherulites of poly-L-lactide crystallized from [$P_{2,4,4,4}$][DEP]. The spherulites appeared in Maltese cross (*i.e.* dark perpendicular cones diverging from the origin) between crossed-polarizer of an optical microscope. The observation proves that molecular chains are aligned in tangential directions. Maltese cross patterns did not change with spherulite rotations, because molecular arrangement was homogeneous versus the polar angle. When polymers are crystallized from thin liquid films (>100 nm), platelets and multilayers (average size of ~150 nm) were evolved. The crystallite

morphologies of polyvinyl alcohol, polyethylene glycol, and poly-L-lactide from solutions in $[P_{2,4,4,4}]$[DEP] are shown in Figure B.3. Polyvinyl alcohol grew up into triangles platelets. Polyethylene glycol and poly-L-lactide resulted in the intermediate structure between lamellae and spherulite. Several platelets were growing from the center in radial directions

In-situ SEM observation of polymer crystallization by lowering temperature:

Polyethylene glycol formed fibril structures from [EMIM][$EtSO_4$] upon crystallization as shown in Figure B.4. Due to physical crosslinking between polymer crystals, the solution was transformed into an opaque gel. To study the progress of crystallization at high magnifications, the solution was observed with *in situ* SEM. The polymer solution (10 wt.% dissolved at 80°C) was suspended on a lacey carbon film. The sample was placed in SEM with a thermal reservoir (*i.e.* $3\times3\times1cm^3$ pebble, Figure B.4). The formation of crystals was visualized as the sample is cooled down below a crystallization temperature. Crystalline fibrils were interconnected and induced gelation of solution (Figure B.4 second row). When the sample was heated by a strong electron beam for a long time, polymer gel was melted back into the solution (Figure B.4 third row).

Morphologies of crystallized polymers produced by adding non-solvents:

Polymer crystallization was promoted by adding non-solvent ILs in to polymer solution. Figure B.4 displays two examples: (i) polycaprolactam crystallized from $[P_{2,4,4,4}]$[DEP] by adding [BMIM][PF_6], and (ii) polyethylene glycol crystallized from [BMIM][TFSI] by adding [BMIM][BF_4]. The ordering of polymer chains was visualized in cross-polarizer optical microscopy. However, the crystal morphology was not uniform,

because the mixing of two ILs was not homogeneous. Even without non-solvent ILs, polymers crystallized out if hygroscopic ILs absorbed moisture from the atmosphere. In Figure B.6, polycaprolactam in $[P_{2,4,4,4}]$[DEP] crystallized when the solution is exposed to the humid air.

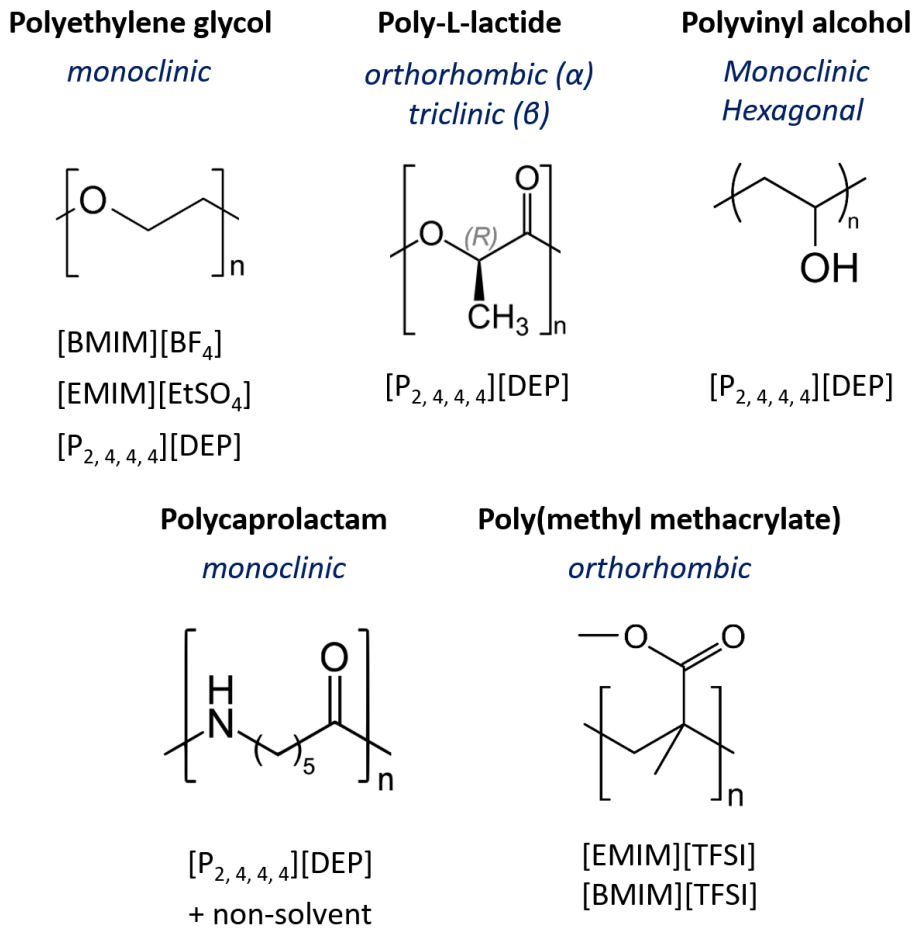

Figure B.1 Parings of polymer and ionic liquid for solution crystallization. Crystallite structures reported from literatures are listed for each polymer. [EMIM][BF_4] is 1-ethyl-3-methylimidazolium tetrafluoroborate, [EMIM][$EtSO_4$] is 1-ethyl-3-methylimidazolium ethylsulfate, [$P_{2,4,4,4}$][DEP] is tributyl(ethyl)phosphonium diethylphosphate, [EMIM] [TFSI] is 1-ethyl-3-methylimidazolium bis(trifluoromethane)sulfonamide, and [BMIM] [TFSI] is 1-buyl-3-methylimidazolium bis(trifluoromethane)sulfonamide

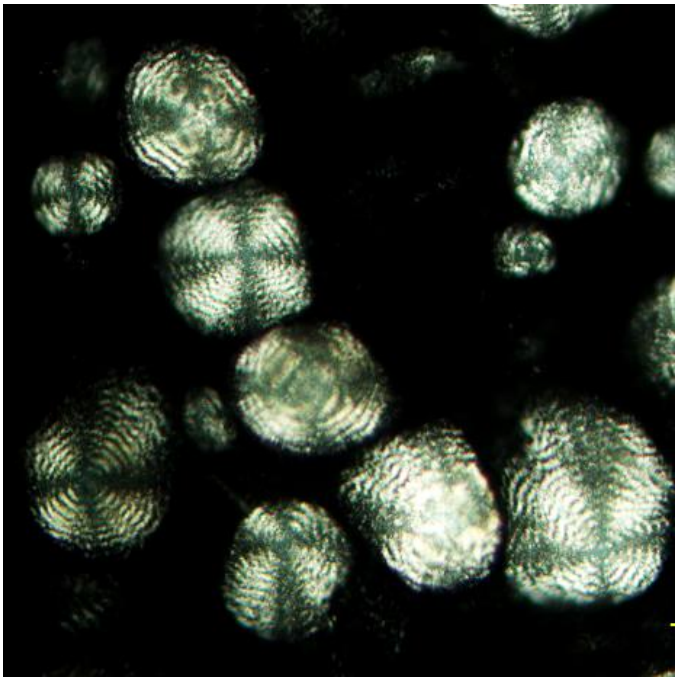

Figure B.2 Poly-L-lactide crystals from tributyl(ethyl)phosphonium diethylphosphate imaged by cross-polarized optical microscopy. Solution at 70°C was cooled down to the room temperature to promote crystallization.

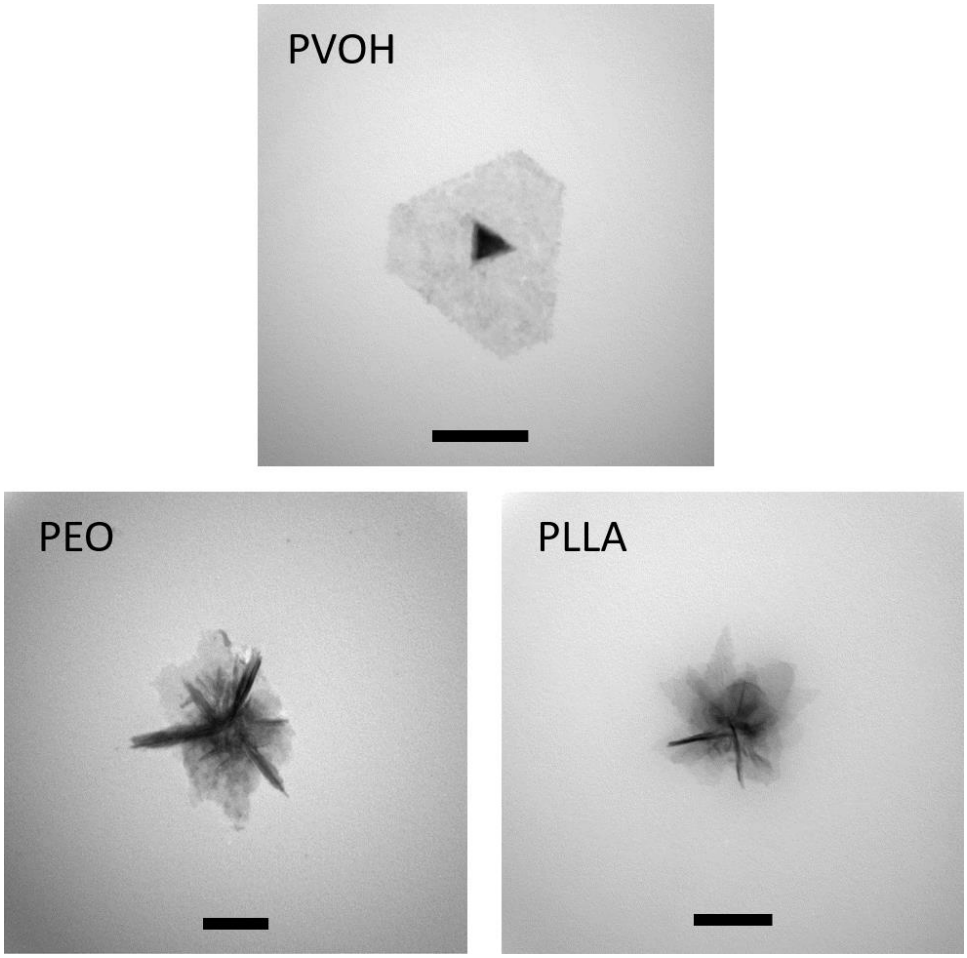

Figure B.3 Micrographs of polymer crystallized from solutions in ionic liquid captured by transmission electron microscopy. (Top) polyvinyl alcohol, (Bottom left) polyethylene glycol, and (Bottom right) poly-L-lactide. Ionic liquid was tributyl(ethyl)phosphonium diethylphosphate. Scale bar size is 100 nm.

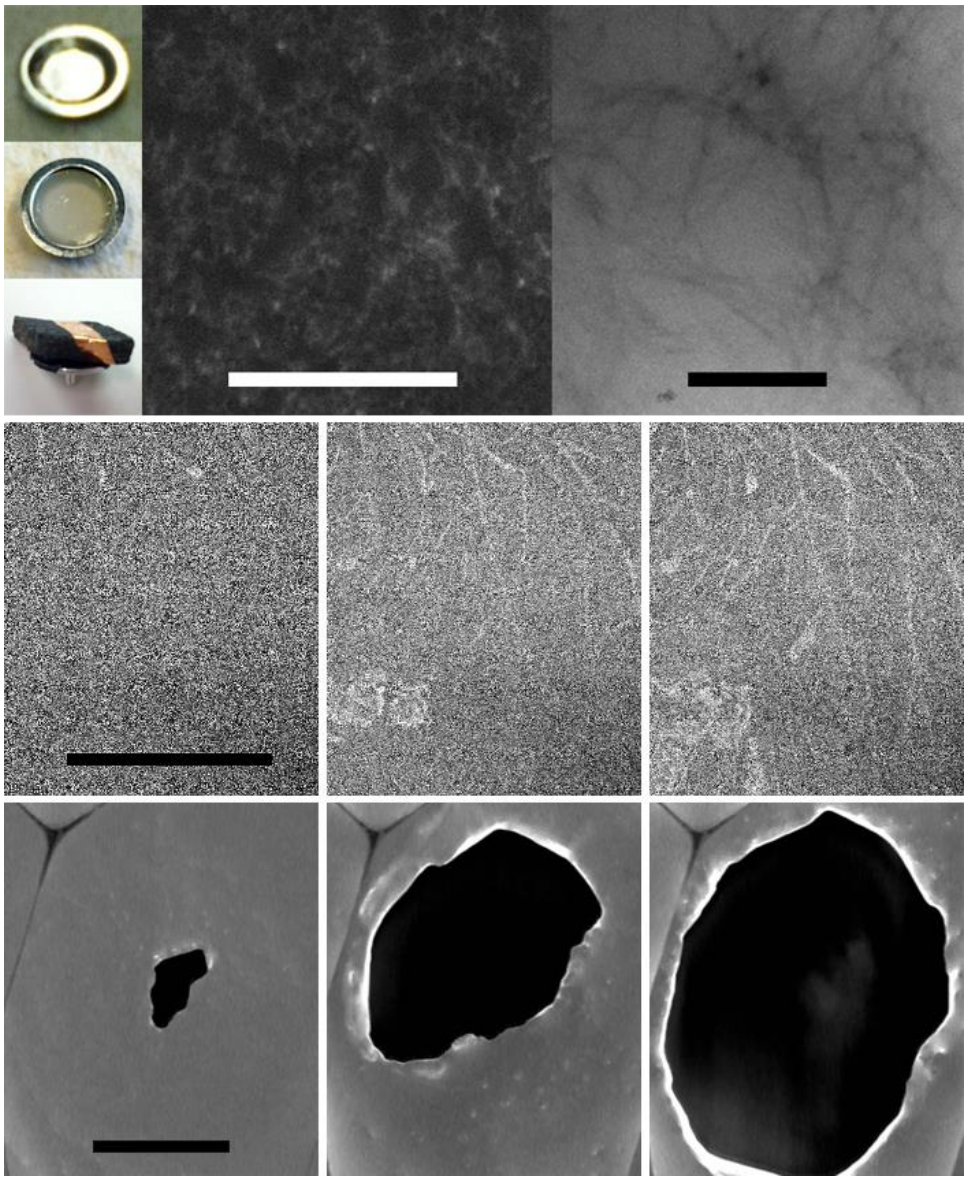

Figure B.4 Gelation of polyethylene glycol in 1-ethyl-3-methylimidazolium ethylsulfate. (First row: left) Polymer solution before crystallization, gelated solution after crystallization and thermal reservoir for *in-situ* observation. (First row: center, right) Fibril structures imaged by SEM and TEM, respectively. Scale bar is 4 μm and 300 nm. (Second row) *in-situ* SEM observation of polymer crystallization. Scale bar is 10 μm. (Third row) Melting of polyethylene glycol crystallites by electron beam heating. Scale bar is 30 μm.

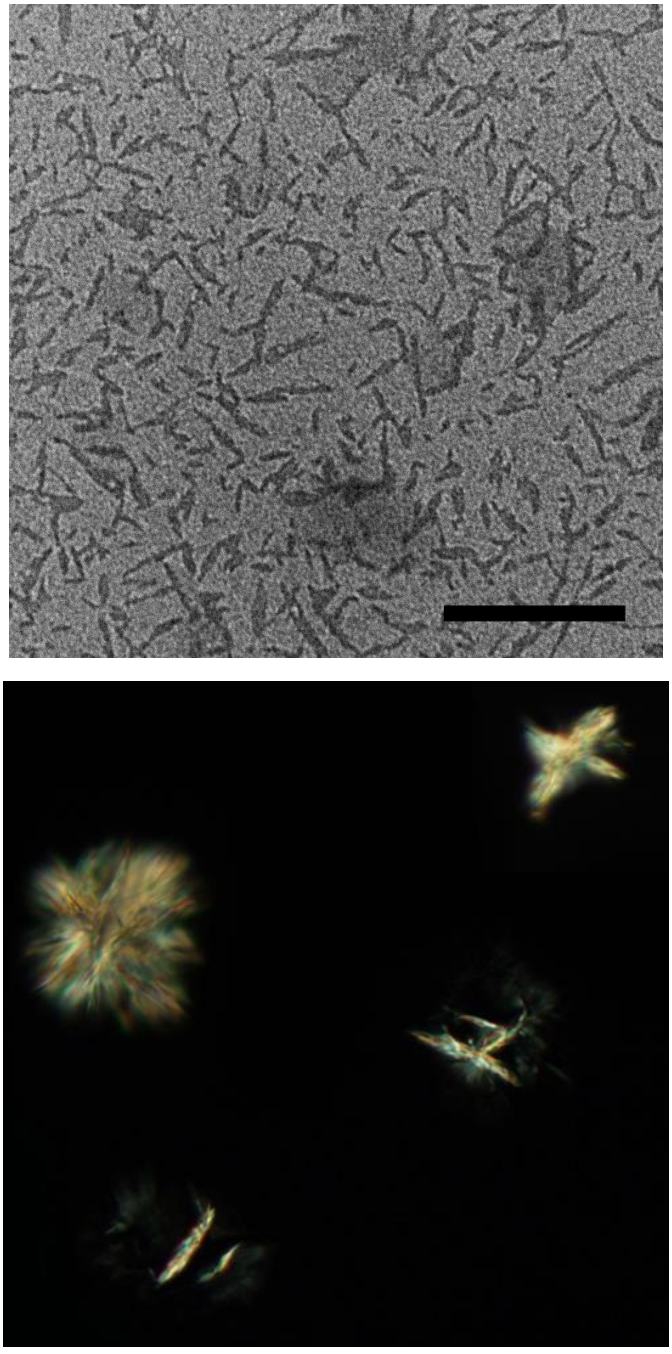

Figure B.5 Polymer crystallized by adding non-solvent ILs. (Top) Polycaprolactam crystallized from tributyl(ethyl)phosphonium diethylphosphate by adding 1-butyl-3-methylimidazolium hexafluorophosphate (Bottom) Polyethylene glycol crystallized from 1-buyl-3-methylimidazolium bis(trifluoromethane)sulfonamide by adding 1-buyl-3-methylimidazolium tetrafluoroborate

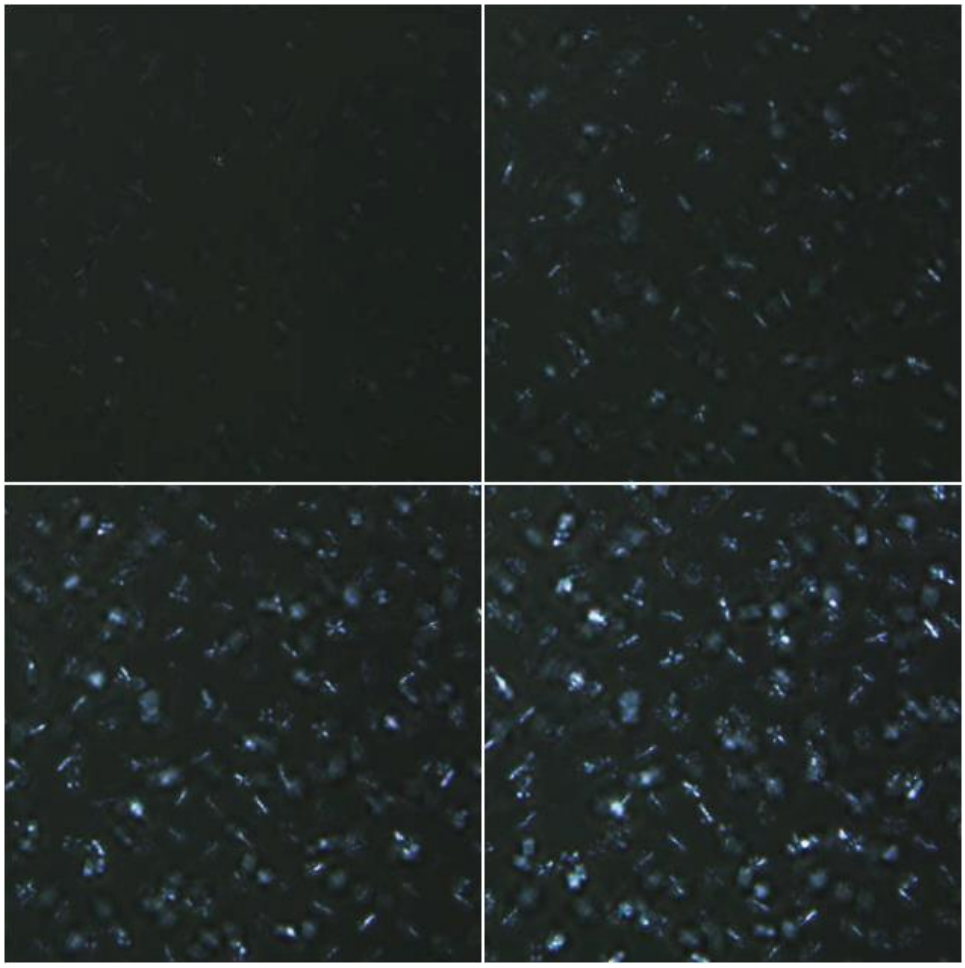

Figure B.6 Time-lapse optical microscope images of polycaprolactam crystallized from tributyl(ethyl)phosphonium diethylphosphate by adsorbing moisture from air. The image sequence is (top left)-(top right)-(bottom left)-(bottom right).

BIBLIOGRAPHY

1. Nelson DR. *Defects and geometry in condensed matter physics*. Cambridge University Press, 2002.

2. Troppenz T, Kuijk A, Imhof A, Van Blaaderen A, Dijkstra M, Van Roij R. Nematic ordering of polarizable colloidal rods in an external electric field: theory and experiment. *Physical Chemistry Chemical Physics* 2015, **17**(34)**:** 22423-22430.

3. Asakura S, Oosawa F. Interaction between particles suspended in solutions of macromolecules. *Journal of Polymer Science* 1958, **33**(126)**:** 183-192.

4. Sainis SK, Germain V, Dufresne ER. Statistics of Particle Trajectories at Short Time Intervals Reveal fN-Scale Colloidal Forces. *Physical Review Letters* 2007, **99**(1)**:** 018303.

5. Crocker JC, Matteo JA, Dinsmore AD, Yodh AG. Entropic Attraction and Repulsion in Binary Colloids Probed with a Line Optical Tweezer. *Physical Review Letters* 1999, **82**(21)**:** 4352-4355.

6. Jue T. *Fundamental concepts in biophysics*. Springer, 2009.

7. Weeks ER, Crocker JC, Levitt AC, Schofield A, Weitz DA. Three-dimensional direct imaging of structural relaxation near the colloidal glass transition. *Science* 2000, **287**(5453)**:** 627-631.

8. Weeks ER, Weitz D. Properties of cage rearrangements observed near the colloidal glass transition. *Physical Review Letters* 2002, **89**(9)**:** 095704.

9. Weeks ER, Weitz DA. Subdiffusion and the cage effect studied near the colloidal glass transition. *Chemical Physics* 2002, **284**(1–2)**:** 361-367.

10. Kasper A, Bartsch E, Sillescu H. Self-diffusion in concentrated colloid suspensions studied by digital video microscopy of core-shell tracer particles. *Langmuir* 1998, **14**(18)**:** 5004-5010.

11. Marcus AH, Schofield J, Rice SA. Experimental observations of non-Gaussian behavior and stringlike cooperative dynamics in concentrated quasi-two-dimensional colloidal liquids. *Physical Review E* 1999, **60**(5)**:** 5725-5736.

12. Courtland RE, Weeks ER. Direct visualization of ageing in colloidal glasses. *Journal of Physics: Condensed Matter* 2002, **15**(1)**:** S359.

13. Prasad V, Semwogerere D, Weeks ER. Confocal microscopy of colloids. *Journal of Physics: Condensed Matter* 2007, **19**(11)**:** 113102.

14. Di Leonardo R, Ianni F, Saglimbeni F, Ruocco G, Keen S, Leach J, *et al.* Optical trapping studies of colloidal interactions in liquid films. *Colloids and Surfaces A: Physicochemical and Engineering Aspects* 2009, **343**(1–3)**:** 133-136.

15. Di Leonardo R, Saglimbeni F, Ruocco G. Very-Long-Range Nature of Capillary Interactions in Liquid Films. *Physical Review Letters* 2008, **100**(10)**:** 106103.

16. Han Y, Alsayed AM, Nobili M, Zhang J, Lubensky TC, Yodh AG. Brownian Motion of an Ellipsoid. *Science* 2006, **314**(5799)**:** 626-630.

17. Crocker JC, Valentine MT, Weeks ER, Gisler T, Kaplan PD, Yodh AG, *et al.* Two-point microrheology of inhomogeneous soft materials. *Physical Review Letters* 2000, **85**(4)**:** 888.

18. Wong I, Gardel M, Reichman D, Weeks ER, Valentine M, Bausch A, *et al.* Anomalous diffusion probes microstructure dynamics of entangled F-actin networks. *Physical Review Letters* 2004, **92**(17)**:** 178101.

19. Xu J, Viasnoff V, Wirtz D. Compliance of actin filament networks measured by particle-tracking microrheology and diffusing wave spectroscopy. *Rheologica Acta* 1998, **37**(4)**:** 387-398.

20. Geerts H, De Brabander M, Nuydens R, Geuens S, Moeremans M, De Mey J, *et al.* Nanovid tracking: a new automatic method for the study of mobility in living cells based on colloidal gold and video microscopy. *Biophysical Journal* 1987, **52**(5)**:** 775-782.

21. Ruska E. The development of the electron microscope and of electron microscopy (Nobel lecture). *Angewandte Chemie International Edition in English* 1987, **26**(7)**:** 595-605.

22. Reimer L. *Transmission electron microscopy: physics of image formation and microanalysis*, vol. 36. Springer, 2013.

23. Bozzola JJ, Russell LD. *Electron microscopy: principles and techniques for biologists*. Jones & Bartlett Learning, 1999.

24. Danilatos GD, Robinson V. Principles of scanning electron microscopy at high specimen chamber pressures. *Scanning* 1979, **2**(2)**:** 72-82.

25. Parsons D, Matricardi V, Moretz R, Turner J. Electron microscopy and diffraction of wet unstained and unfixed biological objects. *Advances in biological and medical physics* 1974, **15:** 161-270.

26. Daulton TL, Little BJ, Lowe K, Jones-Meehan J. In situ environmental cell–transmission electron microscopy study of microbial reduction of chromium (VI) using electron energy loss spectroscopy. *Microscopy and Microanalysis* 2001, **7**(06)**:** 470-485.

27. Nishijima K, Yamasaki J, Orihara H, Tanaka N. Development of microcapsules for electron microscopy and their application to dynamical observation of liquid crystals in transmission electron microscopy. *Nanotechnology* 2004, **15**(6)**:** S329.

28. Mohanty N, Fahrenholtz M, Nagaraja A, Boyle D, Berry V. Impermeable graphenic encasement of bacteria. *Nano Letters* 2011, **11**(3)**:** 1270-1275.

29. Yuk JM, Park J, Ercius P, Kim K, Hellebusch DJ, Crommie MF, *et al.* High-Resolution EM of Colloidal Nanocrystal Growth Using Graphene Liquid Cells. *Science* 2012, **336**(6077)**:** 61-64.

30. Williamson M, Tromp R, Vereecken P, Hull R, Ross F. Dynamic microscopy of nanoscale cluster growth at the solid–liquid interface. *Nature Materials* 2003, **2**(8)**:** 532-536.

31. Kuwabata S, Tsuda T, Torimoto T. Room-Temperature Ionic Liquid. A New Medium for Material Production and Analyses under Vacuum Conditions. *The Journal of Physical Chemistry Letters* 2010, **1**(21)**:** 3177-3188.

32. Wasserscheid P, Welton T. *Ionic liquids in synthesis*, vol. 1. Wiley Online Library, 2008.

33. Mansfeld U, Hoeppener S, Schubert US. Investigating the Motion of Diblock Copolymer Assemblies in Ionic Liquids by In Situ Electron Microscopy. *Advanced Materials (Weinheim, Germany)* 2013, **25**(5)**:** 761-765.

34. Uematsu T, Baba M, Oshima Y, Tsuda T, Torimoto T, Kuwabata S. Atomic Resolution Imaging of Gold Nanoparticle Generation and Growth in Ionic Liquids. *Journal of the American Chemical Society* 2014, **136**(39)**:** 13789-13797.

35. Vella D, Mahadevan L. The "Cheerios effect". *American Journal of Physics* 2005, **73**(9)**:** 817-825.

36. Jaehoon C, Wei Z, Hatch TJ, Jacobs HO. Programmable reconfigurable self-assembly: parallel heterogeneous integration of chip-scale components on planar and nonplanar surfaces. *Journal of Microelectromechanical Systems* 2006, **15**(3)**:** 457-464.

37. Yeh HJJ, Smith JS. Fluidic self-assembly for the integration of GaAs light-emitting diodes on Si substrates. *IEEE Photonics Technology Letters* 1994, **6**(6)**:** 706-708.

38. Srinivasan U, Liepmann D, Howe RT. Microstructure to substrate self-assembly using capillary forces. *Journal of Microelectromechanical Systems* 2001, **10**(1)**:** 17-24.

39. Jacobs HO, Tao AR, Schwartz A, Gracias DH, Whitesides GM. Fabrication of a Cylindrical Display by Patterned Assembly. *Science* 2002, **296**(5566)**:** 323-325.

40. Onoe H, Matsumoto K, Shimoyama I. Three-dimensional micro-self-assembly using hydrophobic interaction controlled by self-assembled monolayers. *Journal of Microelectromechanical Systems* 2004, **13**(4)**:** 603-611.

41. Scott KL, Hirano T, Yang H, Singh H, Howe RT, Niknejad AM. High-performance inductors using capillary based fluidic self-assembly. *Journal of Microelectromechanical Systems* 2004, **13**(2)**:** 300-309.

42. Stauth SA, Parviz BA. Self-assembled single-crystal silicon circuits on plastic. *Proceedings of the National Academy of Sciences* 2006, **103**(38)**:** 13922-13927.

43. Knuesel RJ, Jacobs HO. Self-assembly of microscopic chiplets at a liquid–liquid–solid interface forming a flexible segmented monocrystalline solar cell. *Proceedings of the National Academy of Sciences* 2010, **107**(3)**:** 993-998.

44. Boncheva M, Gracias DH, Jacobs HO, Whitesides GM. Biomimetic self-assembly of a functional asymmetrical electronic device. *Proceedings of the*

National Academy of Sciences 2002, **99**(8)**:** 4937-4940.

45. Zheng W, Buhlmann P, Jacobs HO. Sequential shape-and-solder-directed self-assembly of functional microsystems. *Proceedings of the National Academy of Sciences of the United States of America* 2004, **101**(35)**:** 12814-12817.

46. Nicolson MM. The interaction between floating particles. *Mathematical Proceedings of the Cambridge Philosophical Society* 1949, **45**(02)**:** 288-295.

47. Wickman HH, Korley JN. Colloid crystal self-organization and dynamics at the air/water interface. *Nature* 1998, **393**(6684)**:** 445-447.

48. Nikolaides MG, Bausch AR, Hsu MF, Dinsmore AD, Brenner MP, Gay C, *et al.* Electric-field-induced capillary attraction between like-charged particles at liquid interfaces. *Nature* 2002, **420**(6913)**:** 299-301.

49. Nikolaides MG, Bausch AR, Hsu MF, Dinsmore AD, Brenner MP, Gay C, *et al.* Capillary attraction (communication arising): Like-charged particles at liquid interfaces. *Nature* 2003, **424**(6952)**:** 1014-1014.

50. Lewandowski EP, Cavallaro M, Botto L, Bernate JC, Garbin V, Stebe KJ. Orientation and Self-Assembly of Cylindrical Particles by Anisotropic Capillary Interactions. *Langmuir* 2010, **26**(19)**:** 15142-15154.

51. Botto L, Lewandowski EP, Cavallaro M, Stebe KJ. Capillary interactions between anisotropic particles. *Soft Matter* 2012, **8**(39)**:** 9957-9971.

52. Loudet JC, Alsayed AM, Zhang J, Yodh AG. Capillary Interactions Between Anisotropic Colloidal Particles. *Physical Review Letters* 2005, **94**(1)**:** 018301.

53. Madivala B, Fransaer J, Vermant J. Self-Assembly and Rheology of Ellipsoidal Particles at Interfaces. *Langmuir* 2009, **25**(5)**:** 2718-2728.

54. Lewandowski EP, Bernate JA, Tseng A, Searson PC, Stebe KJ. Oriented assembly of anisotropic particles by capillary interactions. *Soft Matter* 2009, **5**(4)**:** 886-890.

55. Wang J-Y, Wang Y, Sheiko SS, Betts DE, DeSimone JM. Tuning Multiphase Amphiphilic Rods to Direct Self-Assembly. *Journal of the American Chemical Society* 2012, **134**(13)**:** 5801-5806.

56. Loudet JC, Pouligny B. Self-assembled capillary arrows. *EPL (Europhysics Letters)* 2009, **85**(2)**:** 28003.

57. Lewandowski EP, Bernate JA, Searson PC, Stebe KJ. Rotation and Alignment of Anisotropic Particles on Nonplanar Interfaces. *Langmuir* 2008, **24**(17)**:** 9302-9307.

58. Cavallaro M, Botto L, Lewandowski EP, Wang M, Stebe KJ. Curvature-driven capillary migration and assembly of rod-like particles. *Proceedings of the National Academy of Sciences* 2011, **108**(52)**:** 20923-20928.

59. Nierop EAv, Stijnman MA, Hilgenfeldt S. Shape-induced capillary interactions of colloidal particles. *EPL (Europhysics Letters)* 2005, **72**(4)**:** 671.

60. Würger A. Curvature-induced capillary interaction of spherical particles at a liquid interface. *Physical Review E* 2006, **74**(4)**:** 041402.

61. Léandri J, Würger A. Trapping energy of a spherical particle on a curved liquid interface. *Journal of Colloid and Interface Science* 2013, **405:** 249-255.

62. McEnnis K, Dinsmore AD, Russell TP. Solid Particles Adsorbed on Capillary-Bridge-Shaped Fluid Polystyrene Surfaces. *Langmuir* 2015, **31**(19)**:** 5299-5305.

63. Blanc C, Fedorenko D, Gross M, In M, Abkarian M, Gharbi MA, *et al.* Capillary Force on a Micrometric Sphere Trapped at a Fluid Interface Exhibiting Arbitrary Curvature Gradients. *Physical Review Letters* 2013, **111**(5)**:** 058302.

64. Ershov D, Sprakel J, Appel J, Cohen Stuart MA, van der Gucht J. Capillarity-induced ordering of spherical colloids on an interface with anisotropic curvature. *Proceedings of the National Academy of Sciences* 2013, **110**(23)**:** 9220-9224.

65. Zeng C, Brau F, Davidovitch B, Dinsmore AD. Capillary interactions among spherical particles at curved liquid interfaces. *Soft Matter* 2012, **8**(33)**:** 8582-8594.

66. Einstein A. Über die von der molekularkinetischen Theorie der Wärme geforderte Bewegung von in ruhenden Flüssigkeiten suspendierten Teilchen. *Annalen der Physik* 1905, **322**(8)**:** 549-560.

67. Doi M, Edwards SF. *The theory of polymer dynamics*, vol. 73. oxford university press, 1988.

68. Kleinstreuer C. *Engineering fluid dynamics: an interdisciplinary systems approach*. Cambridge University Press, 1997.

69. Tirado MM, Martínez CL, de la Torre JG. Comparison of theories for the translational and rotational diffusion coefficients of rod-like macromolecules. Application to short DNA fragments. *The Journal of Chemical Physics* 1984, **81**(4)**:** 2047-2052.

70. Tirado MM, de la Torre JG. Rotational dynamics of rigid, symmetric top macromolecules. Application to circular cylinders. *The Journal of Chemical Physics* 1980, **73**(4)**:** 1986-1993.

71. Tirado MM, de la Torre JG. Translational friction coefficients of rigid, symmetric top macromolecules. Application to circular cylinders. *The Journal of Chemical Physics* 1979, **71**(6)**:** 2581-2587.

72. International Congress of Surface A. *Proceedings of the Second International Congress of Surface Activity*. London : Butterworths, 1957., 1957.

73. Saffman PG, Delbrück M. Brownian motion in biological membranes. *Proceedings of the National Academy of Sciences* 1975, **72**(8)**:** 3111-3113.

74. Graf K, Kappl M. *Physics and chemistry of interfaces*. John Wiley & Sons, 2006.

75. Defay R PI. *Surface Tension and Adsorption*. Green& Co Ltd, London, 1966.

76. Pieranski P. Two-Dimensional Interfacial Colloidal Crystals. *Physical Review Letters* 1980, **45**(7)**:** 569-572.

77. Davidovitch B, Ertaş D, Halsey TC. Ripening of porous media. *Physical Review E* 2004, **70**(3)**:** 031609.

78. Danov KD, Kralchevsky PA. Capillary forces between particles at a liquid interface: General theoretical approach and interactions between capillary multipoles. *Advances in Colloid and Interface Science* 2010, **154**(1–2)**:** 91-103.

79. Kralchevsky PA, Denkov ND. Capillary forces and structuring in layers of colloid particles. *Current Opinion in Colloid & Interface Science* 2001, **6**(4)**:** 383-401.

80. Dubochet J, Adrian M, Chang J-J, Homo J-C, Lepault J, McDowall AW, *et al.* Cryo-electron microscopy of vitrified specimens. *Quarterly Reviews of Biophysics* 1988, **21**(02)**:** 129-228.

81. Donald AM. The use of environmental scanning electron microscopy for imaging wet and insulating materials. *Nature Materials* 2003, **2**(8)**:** 511-516.

82. de Jonge N, Ross FM. Electron microscopy of specimens in liquid. *Nat Nano* 2011, **6**(11)**:** 695-704.

83. Williamson MJ, Tromp RM, Vereecken PM, Hull R, Ross FM. Dynamic microscopy of nanoscale cluster growth at the solid-liquid interface. *Nature Materials* 2003, **2**(8)**:** 532-536.

84. Zheng H, Claridge SA, Minor AM, Alivisatos AP, Dahmen U. Nanocrystal Diffusion in a Liquid Thin Film Observed by in Situ Transmission Electron Microscopy. *Nano Letters* 2009, **9**(6)**:** 2460-2465.

85. Park J, Elmlund H, Ercius P, Yuk JM, Limmer DT, Chen Q, *et al.* 3D structure of individual nanocrystals in solution by electron microscopy. *Science* 2015, **349**(6245)**:** 290-295.

86. Chen Q, Smith JM, Park J, Kim K, Ho D, Rasool HI, *et al.* 3D Motion of DNA-Au Nanoconjugates in Graphene Liquid Cell Electron Microscopy. *Nano Letters* 2013, **13**(9)**:** 4556-4561.

87. Susan MABH, Kaneko T, Noda A, Watanabe M. Ion Gels Prepared by in Situ Radical Polymerization of Vinyl Monomers in an Ionic Liquid and Their Characterization as Polymer Electrolytes. *Journal of the American Chemical Society* 2005, **127**(13)**:** 4976-4983.

88. Fukushima T, Kosaka A, Ishimura Y, Yamamoto T, Takigawa T, Ishii N, *et al.* Molecular Ordering of Organic Molten Salts Triggered by Single-Walled Carbon Nanotubes. *Science* 2003, **300**(5628)**:** 2072-2074.

89. Wang P, Zakeeruddin SM, Comte P, Exnar I, Grätzel M. Gelation of Ionic Liquid-Based Electrolytes with Silica Nanoparticles for Quasi-Solid-State Dye-Sensitized Solar Cells. *Journal of the American Chemical Society* 2003, **125**(5)**:** 1166-1167.

90. Maleki N, Safavi A, Tajabadi F. High-Performance Carbon Composite Electrode

Based on an Ionic Liquid as a Binder. *Analytical Chemistry* 2006, **78**(11)**:** 3820-3826.

91. Swatloski RP, Spear SK, Holbrey JD, Rogers RD. Dissolution of Cellose with Ionic Liquids. *Journal of the American Chemical Society* 2002, **124**(18)**:** 4974-4975.

92. Welton T. Room-Temperature Ionic Liquids. Solvents for Synthesis and Catalysis. *Chemical Reviews (Washington, DC, United States)* 1999, **99**(8)**:** 2071-2084.

93. Kaintz A, Baker G, Benesi A, Maroncelli M. Solute Diffusion in Ionic Liquids, NMR Measurements and Comparisons to Conventional Solvents. *The Journal of Physical Chemistry B* 2013, **117**(39)**:** 11697-11708.

94. Smith EF, Villar Garcia IJ, Briggs D, Licence P. Ionic liquids in vacuo; solution-phase X-ray photoelectron spectroscopy. *Chemical Communications (Cambridge, United Kingdom)* 2005(45)**:** 5633-5635.

95. Chen S, Kobayashi K, Kitaura R, Miyata Y, Shinohara H. Direct HRTEM Observation of Ultrathin Freestanding Ionic Liquid Film on Carbon Nanotube Grid. *ACS Nano* 2011, **5**(6)**:** 4902-4908.

96. Maddikeri RR, Colak S, Gido SP, Tew GN. Zwitterionic Polymersomes in an Ionic Liquid: Room Temperature TEM Characterization. *Biomacromolecules* 2011, **12**(10)**:** 3412-3417.

97. Kuwabata S, Kongkanand A, Oyamatsu D, Torimoto T. Observation of Ionic Liquid by Scanning Electron Microscope. *Chemistry Letters* 2006, **35**(6)**:** 600-601.

98. Huang JY, Zhong L, Wang CM, Sullivan JP, Xu W, Zhang LQ, *et al*. In Situ Observation of the Electrochemical Lithiation of a Single SnO2 Nanowire Electrode. *Science* 2010, **330**(6010)**:** 1515-1520.

99. Zhang Z, Berns AE, Willbold S, Buitenhuis J. Synthesis of poly(ethylene glycol) (PEG)-grafted colloidal silica particles with improved stability in aqueous solvents. *Journal of Colloid and Interface Science* 2007, **310**(2)**:** 446-455.

100. Ueno K, Inaba A, Kondoh M, Watanabe M. Colloidal Stability of Bare and Polymer-Grafted Silica Nanoparticles in Ionic Liquids. *Langmuir* 2008, **24**(10)**:** 5253-5259.

101. Ren S, Hou Y, Wu W, Liu W. Purification of Ionic Liquids: Sweeping Solvents by Nitrogen. *Journal of Chemical and Engineering Data* 2010, **55**(11)**:** 5074-5077.

102. Bogush GH, Tracy MA, Zukoski Iv CF. Preparation of monodisperse silica particles: Control of size and mass fraction. *Journal of Non-Crystalline Solids* 1988, **104**(1)**:** 95-106.

103. Gao C, Lu Z, Yin Y. Gram-Scale Synthesis of Silica Nanotubes with Controlled Aspect Ratios by Templating of Nickel-Hydrazine Complex Nanorods. *Langmuir* 2011, **27**(19)**:** 12201-12208.

104. Egerton R. *Electron energy-loss spectroscopy in the electron microscope*. Springer Science & Business Media, 2011.

105. Czyżewski Z, MacCallum DON, Romig A, Joy DC. Calculations of Mott scattering cross section. *Journal of Applied Physics* 1990, **68**(7)**:** 3066-3072.

106. Casnati E, Tartari A, Baraldi C. An empirical approach to K-shell ionisation cross section by electrons. *Journal of Physics B: Atomic and Molecular Physics* 1983, **16**(3)**:** 505.

107. Joy DC, Luo S. An empirical stopping power relationship for low-energy electrons. *Scanning* 1989, **11**(4)**:** 176-180.

108. Gauvin R, Hovington P, Drouin D. Quantification of spherical inclusions in the scanning electron microscope using Monte Carlo simulations. *Scanning* 1995, **17**(4)**:** 202-219.

109. Crocker JC, Weeks ER. Particle tracking using IDL. 2011 [cited 2016 10 Sep]Available from: http://www.physics.emory.edu/faculty/weeks//idl/

110. Narayan V, Menon N, Ramaswamy S. Nonequilibrium steady states in a vibrated-rod monolayer: tetratic, nematic, and smectic correlations. *Journal of Statistical Mechanics: Theory and Experiment* 2006, **2006**(01)**:** P01005.

111. Fröba AP, Kremer H, Leipertz A. Density, Refractive Index, Interfacial Tension, and Viscosity of Ionic Liquids [EMIM][EtSO4], [EMIM][NTf2], [EMIM][N(CN)2], and [OMA][NTf2] in Dependence on Temperature at Atmospheric Pressure. *The Journal of Physical Chemistry B* 2008, **112**(39)**:** 12420-12430.

112. Sur J, Kyu Pak H. Capillary Force on Colloidal Particles in a Freely Suspended Liquid Thin Film. *Physical Review Letters* 2001, **86**(19)**:** 4326-4329.

113. Egerton RF, Li P, Malac M. Radiation damage in the TEM and SEM. *Micron* 2004, **35**(6)**:** 399-409.

114. Noda A, Hayamizu K, Watanabe M. Pulsed-Gradient Spin−Echo 1H and 19F NMR Ionic Diffusion Coefficient, Viscosity, and Ionic Conductivity of Non-Chloroaluminate Room-Temperature Ionic Liquids. *The Journal of Physical Chemistry B* 2001, **105**(20)**:** 4603-4610.

115. Leys J, Wübbenhorst M, Preethy Menon C, Rajesh R, Thoen J, Glorieux C, *et al.* Temperature dependence of the electrical conductivity of imidazolium ionic liquids. *The Journal of Chemical Physics* 2008, **128**(6)**:** 064509.

116. Margulis CJ, Annapureddy HVR, De Biase PM, Coker D, Kohanoff J, Del Pópolo MG. Dry Excess Electrons in Room-Temperature Ionic Liquids. *Journal of the American Chemical Society* 2011, **133**(50)**:** 20186-20193.

117. Skrzypczak A, Neta P. Diffusion-Controlled Electron-Transfer Reactions in Ionic Liquids. *The Journal of Physical Chemistry A* 2003, **107**(39)**:** 7800-7803.

118. Prasad V, Weeks ER. Two-Dimensional to Three-Dimensional Transition in Soap Films Demonstrated by Microrheology. *Physical Review Letters* 2009, **102**(17)**:** 178302.

119. Vivek S, Weeks ER. Measuring and Overcoming Limits of the Saffman-Delbrück Model for Soap Film Viscosities. *PLoS One* 2015, **10**(3)**:** e0121981.

120. Cheung C, Hwang YH, Wu Xl, Choi HJ. Diffusion of Particles in Free-Standing Liquid Films. *Physical Review Letters* 1996, **76**(14)**:** 2531-2534.

121. Han Y, Alsayed A, Nobili M, Yodh AG. Quasi-two-dimensional diffusion of single ellipsoids: Aspect ratio and confinement effects. *Physical Review E* 2009, **80**(1)**:** 011403.

122. Bates MA, Frenkel D. Phase behavior of two-dimensional hard rod fluids. *The Journal of Chemical Physics* 2000, **112**(22)**:** 10034-10041.

123. Boniello G, Blanc C, Fedorenko D, Medfai M, Mbarek NB, In M, *et al.* Brownian diffusion of a partially wetted colloid. *Nature Materials* 2015, **14**(9)**:** 908-911.

124. Onoe H, Matsumoto K, Shimoyama I. Three-Dimensional Sequential Self-Assembly of Microscale Objects. *Small* 2007, **3**(8)**:** 1383-1389.

125. Bowden N, Arias F, Deng T, Whitesides GM. Self-Assembly of Microscale Objects at a Liquid/Liquid Interface through Lateral Capillary Forces. *Langmuir* 2001, **17**(5)**:** 1757-1765.

126. Sharifi-Mood N, Liu IB, Stebe KJ. Curvature capillary migration of microspheres. *Soft Matter* 2015, **11**(34)**:** 6768-6779.

127. Yao L, Sharifi-Mood N, Liu IB, Stebe KJ. Capillary migration of microdisks on curved interfaces. *Journal of Colloid and Interface Science* 2015, **449:** 436-442.

128. Brown ABD, Smith CG, Rennie AR. Fabricating colloidal particles with photolithography and their interactions at an air-water interface. *Physical Review E* 2000, **62**(1)**:** 951-960.

129. Loudet JC, Yodh AG, Pouligny B. Wetting and Contact Lines of Micrometer-Sized Ellipsoids. *Physical Review Letters* 2006, **97**(1)**:** 018304.

130. Lehle H, Noruzifar E, Oettel M. Ellipsoidal particles at fluid interfaces. *The European Physical Journal E* 2008, **26**(1)**:** 151-160.

131. Kaz DM, McGorty R, Mani M, Brenner MP, Manoharan VN. Physical ageing of the contact line on colloidal particles at liquid interfaces. *Nature Materials* 2012, **11**(2)**:** 138-142.

132. Kralchevsky PA, Paunov VN, Denkov ND, Nagayama K. Capillary Image Forces. *Journal of Colloid and Interface Science* 1994, **167**(1)**:** 47-65.

133. Velev OD, Denkov ND, Paunov VN, Kralchevsky PA, Nagayama K. Capillary Image Forces. *Journal of Colloid and Interface Science* 1994, **167**(1)**:** 66-73.

134. KIM I, ELGHOBASHI S, SIRIGNANO WA. On the equation for spherical-particle motion: effect of Reynolds and acceleration numbers. *Journal of Fluid Mechanics* 1998, **367:** 221-253.

135. Hall CE, Inoue T. Experimental Study of Electron Scattering in Electron Microscope Specimens. *Journal of Applied Physics* 1957, **28**(11)**:** 1346-1348.

136. Pegram LM, Record MT. Using Surface Tension Data to Predict Differences in Surface and Bulk Concentrations of Nonelectrolytes in Water. *Journal of Physical Chemistry C* 2009, **113**(6)**:** 2171-2174.

137. Tokuyasu KT. STUDY OF POSITIVE STAINING OF ULTRATHIN FROZEN SECTIONS. *Journal of Ultrastructure Research* 1978, **63**(3)**:** 287-307.

138. Liou W, Geuze HJ, Slot JW. Improving structural integrity of cryosections for immunogold labeling. *Histochemistry and Cell Biology* 1996, **106**(1)**:** 41-58.

139. Gao L, McCarthy TJ. Ionic Liquid Marbles. *Langmuir* 2007, **23**(21)**:** 10445-10447.

140. Huddleston JG, Visser AE, Reichert WM, Willauer HD, Broker GA, Rogers RD. Characterization and comparison of hydrophilic and hydrophobic room temperature ionic liquids incorporating the imidazolium cation. *Green Chemistry* 2001, **3**(4)**:** 156-164.

141. Zhang S, Sun N, He X, Lu X, Zhang X. Physical Properties of Ionic Liquids: Database and Evaluation. *Journal of Physical and Chemical Reference Data* 2006, **35**(4)**:** 1475-1517.

142. Nockemann P, Binnemans K, Driesen K. Purification of imidazolium ionic liquids for spectroscopic applications. *Chemical Physics Letters* 2005, **415**(1-3)**:** 131-136.

143. Schmidt H, Stephan M, Safarov J, Kul I, Nocke J, Abdulagatov IM, *et al.* Experimental study of the density and viscosity of 1-ethyl-3-methylimidazolium ethyl sulfate. *The Journal of Chemical Thermodynamics* 2012, **47**(0)**:** 68-75.